Fabrication and Modelling of MgZnO/ZnO based Heterostructures to realize 2D Confinement of Electron Gas for HEMT Application

A THESIS

Submitted in partial fulfillment of the
requirements for the award of the degree
of
DOCTOR OF PHILOSOPHY

by

ROHIT SINGH

DISCIPLINE OF ELECTRICAL ENGINEERING
INDIAN INSTITUTE OF TECHNOLOGY INDORE
AUG. 2018

INDIAN INSTITUTE OF TECHNOLOGY INDORE

CANDIDATE'S DECLARATION

I hereby certify that the work which is being presented in the thesis entitled **Fabrication and Modelling of MgZnO/ZnO based Heterostructures to realize 2D Confinement of Electron Gas for HEMT Application,** in the partial fulfillment of the requirements for the award of the degree of **Doctor of Philosophy** and submitted in the **Discipline of Electrical Engineering, Indian Institute of Technology Indore**, is an authentic record of my own work carried out during the time period from **July, 2014** to **July, 2018** under the supervisions of **Dr. Shaibal Mukherjee**, Associate Professor, Electrical Engineering, IIT Indore, **Dr. Abhinav Kranti**, Professor, Electrical Engineering, IIT Indore, and **Dr. Ajay Agarwal**, Sr. Principal Scientist, Coordinator, Smart Sensors Area, and Head of Nano Biosensors Group at CSIR-Central Electronics Engineering Research Institute, Pilani.

The matter presented in this thesis has not been submitted by me for the award of any other degree of this or any other institute.

Signature of the student with date

ROHIT SINGH

This is to certify that the above statement made by the candidate is correct to the best of our knowledge.

Signature of Thesis Supervisor #1 with date
Dr. SHAIBAL MUKHERJEE

Signature of Thesis Supervisor #2 with date
Dr. ABHINAV KRANTI

Signature of Thesis Supervisor #3 with date
Dr. AJAY AGARWAL

ROHIT SINGH has successfully given his Ph.D. Oral Examination held on ----------

Signature of Chairman OEB
Date:

Signature of External Examiner
Date:

Signature(s) of Thesis Supervisor(s)
Date:

Signature of PSPC Member #1
Date:

Signature of PSPC Member #2
Date:

Signature of Convener, DPGC
Date:

Signature of Head of Discipline
Date:

ACKNOWLEDGEMENTS

There are many people who have made important contributions to this dissertation. It would be impossible to list everyone who contributed, or to completely list the extent of the contributions for those who are mentioned.

First of all, I would like to express my deep sense of gratitude to my supervisor **Dr. Shaibal Mukherjee** and co-supervisors **Dr. Abhinav Kranti** and **Dr. Ajay Agarwal** for their outstanding mentorship and support that they provided over the past four years. They were always accessible and have been a constant source of advice to keep my project headed toward its main goal. Dr. Mukherjee played an influential role in developing my research skills and personality. I benefited immensely from his vast technical expertise and insight, he could not even realize how much I have learned from him.

I am extremely grateful to my doctoral committee members **Dr. Apurba K. Das** and **Dr. Vimal Bhatia** for giving me valuable advice on my research and kindly going through my dissertation. My sincere appreciation to **Dr. Mukul Gupta** of UGC-DAE consortium for scientific research, in providing magnetron sputtering facilities for metal deposition. Furthermore, I would like to acknowledge the support from **Mr. Tomohiko Yamakami** of the Technical Division, Faculty of Engineering, Shinshu University for TEM imaging.

I would like to thank **Dr. Pradeep Mathur**, Director, IIT Indore for providing the essential experimental facilities and financial support in attending international conferences. I want to acknowledge the support provided by sophisticated instrumentation center (SIC) at IIT Indore, for performing SEM, EDX and XRD measurements. I would like to thank my fellow group members including **Dr. Saurabh K. Pandey, Dr. Sushil K. Pandey, Dr. Vishnu Awasthi, Dr. Pankaj Sharma, Aaryashree, Vivek Garg, Brajendra Singh Sengar, Amitesh Kumar, Md Arif Khan, Ritesh Bhardwaj, Mangal Das, Biswajit Mandal, Gaurav Siddharth, Pawan Kumar, Sanjay Kumar, Daya Shankar Sharma, Ruchi Singh,** and others for their valuable support and co-operation during this research work.

Last, but far from least, I must thank my parents, sister, brother, and my wife, who have supported me in all of my academic accomplishments. I owe a lot to them.

Rohit Singh

Dedicated to my parents

LIST OF PUBLICATIONS

A: Publications from PhD thesis work

A1. In refereed journals

1. **Rohit Singh**, Md Arif Khan, Shaibal Mukherjee, and Abhinav Kranti, *Role of surface states and interface charges in 2DEG in sputtered ZnO heterostructures*, **IEEE Transactions on Electron Devices**, vol. 65, no. 7, pp. 2850-2854, July 2018. **(impact factor: 2.605)**
2. **Rohit Singh**, Md Arif Khan, Pankaj Sharma, Myo Than Htay, Abhinav Kranti, and Shaibal Mukherjee, *Two dimensional electron gases in MgZnO/ZnO and ZnO/MgZnO/ZnO heterostructures grown by dual ion beam sputtering*, **Journal of Physics D: Applied Physics**, vol. 51, no. 13, p. 13LT02, April 2018. **(impact factor: 2.588)**
3. **Rohit Singh**, Md Arif Khan, Shaibal Mukherjee, and Abhinav Kranti, *Analytical model for 2DEG density in graded MgZnO/ZnO heterostructures with cap layer*, **IEEE Transactions on Electron Devices**, vol. 64, no. 9, pp. 3661-3667, September 2017. **(impact factor: 2.605)**
4. **Rohit Singh**, Pankaj Sharma, Md Arif Khan, Vivek Garg, Vishnu Awasthi, Abhinav Kranti, and Shaibal Mukherjee, *Investigation of barrier inhomogeneities and interface state density in Au/MgZnO:Ga Schottky contact*, **Journal of Physics D: Applied Physics**, vol. 49, no. 44, p. 445303, November 2016. **(impact factor: 2.588)**

A2. In refereed conferences

1. **Rohit Singh**, Md Arif Khan, Pankaj Sharma, Abhinav Kranti, and Shaibal Mukherjee, *Variation of 2DEG density in DIBS-grown MgZnO/ZnO and ZnO/MgZnO/ZnO heterostructures*, **19th International Workshop on The Physics of Semiconductor Devices (19th IWPSD), IIT Delhi, India**, December 11-15, 2017.
2. **Rohit Singh**, Md Arif Khan, Ritesh Bhardwaj, Abhinav Kranti, and Shaibal Mukherjee, *2DEG Density in Dual Ion Beam Sputtering Grown ZnO Based Heterostructures*, **6th International Symposium on Integrated**

Functionalities, Shangri-La's Eros Hotel, Delhi, India, December 10-13, 2017.

3. **Rohit Singh**, Md Arif Khan, Abhinav Kranti, and Shaibal Mukherjee, *Two dimensional electron gas in MgZnO/ZnO heterostructures grown by dual-ion beam sputtering*, **Compound Semiconductor Week 2016, Toyama, Japan**, June 26-30, 2016.
4. **Rohit Singh**, Pankaj Sharma, Md Arif Khan, Vishnu Awasthi, Abhinav Kranti, and Shaibal Mukherjee, *Study of interface states in Au/MgZnO:Ga schottky contact grown by dual ion beam sputtering*, **18th International Workshop on The Physics of Semiconductor Devices (18th IWPSD), IISc, Bangalore, India**, December 7-10, 2015.

A3. Book chapters

Nil

A4. Patents

1. *A method of fabricating zinc oxide based heterostructure for high electron mobility transistor*

   Inventors: Shaibal Mukherjee, Abhinav Kranti, **Rohit Singh** and Md Arif Khan

   Patent No. 201721007309, March 1, 2017 (**Status: Published**)

B: Other publications during PhD

B1. In refereed journals

1. Md Arif Khan, **Rohit Singh**, Ritesh Bhardwaj, Amitesh Kumar, Amit Kumar Das, Pankaj Misra, Abhinav Kranti, and Shaibal Mukherjee, *Enhanced sheet charge density in DIBS grown CdO alloyed ZnO buffer based heterostructure*, **IEEE Electron Device Letters**, vol. 39, no. 6, pp. 827-830, June 2018. **(impact factor: 3.048)**
2. Ritesh Bhardwaj, Pankaj Sharma, **Rohit Singh**, Mukul Gupta, and Shaibal Mukherjee, *High responsivity $Mg_xZn_{1-x}O$ based ultraviolet photodetector*

fabricated by dual ion beam sputtering, **IEEE Sensors Journal**, vol. 18, no. 7, pp. 2744-2750, April 2018. **(impact factor: 2.512)**

3. Biswajit Mandal, Aaryashree, **Rohit Singh**, and Shaibal Mukherjee, *Highly selective and sensitive methanol sensor using rose-like ZnO microcube and MoO_3 micrograss based composite*, **IEEE Sensors Journal**, vol. 18, no. 7, pp. 2659-2666, April 2018. **(impact factor: 2.512)**
4. Vivek Garg, Brajendra S. Sengar, Vishnu Awasthi, Amitesh Kumar, **Rohit Singh**, Shailendra Kumar, C. Mukherjee, V. V. Atuchin, and Shaibal Mukherjee, *Investigation of dual-ion beam sputter-instigated plasmon generation in TCOs: A case study of GZO*, **ACS Applied Materials and Interfaces**, vol. 10, pp. 5464−5474, February 2018. **(impact factor: 8.097)**
5. Mangal Das, Amitesh Kumar, **Rohit Singh**, Myo Than Htay and Shaibal Mukherjee, *Realization of synaptic learning and memory functions in Y_2O_3 based memristive device fabricated by dual ion beam sputtering*, **Nanotechnology**, vol. 29, no. 5, p. 055203, February 2018. **(impact factor: 3.440)**
6. Pankaj Sharma, Ritesh Bhardwaj, **Rohit Singh**, Shailendra Kumar, and Shaibal Mukherjee, *Investigation of formation mechanism of Li-P dual-acceptor doped p-type ZnO*, **Applied Physics Letters**, vol. 111, no. 9, p. 091604, August 2017. **(impact factor: 3.411)**
7. Ritesh Bhardwaj, Pankaj Sharma, **Rohit Singh**, and Shaibal Mukherjee, *Sb-doped p-MgZnO/n-Si heterojunction UV photodetector fabricated by dual ion beam sputtering*, **IEEE Photonics Technology Letters**, vol. 19, no. 14, pp. 1215-1218, July 2017. **(impact factor: 2.375)**
8. Md. Arif Khan, **Rohit Singh**, Shaibal Mukherjee, and Abhinav Kranti, *Buffer layer engineering for high ($\geq 10^{13}$ cm^{-2}) 2-DEG density in ZnO-based heterostructure*, **IEEE Transactions on Electron Devices**, vol. 64, no. 3, pp. 1015-1019, March 2017. **(impact factor: 2.605)**
9. Pankaj Sharma, **Rohit Singh**, Vishnu Awasthi, Sushil K. Pandey, and Shaibal Mukherjee, *Detection of a high photoresponse at zero bias from a highly conducting ZnO:Ga based UV photodetector*, **RSC Advances**, vol. 5, no. 104, pp. 85523-85529, October 2015. **(impact factor: 3.108)**

B2. In refereed conferences

1. Ritesh Bhardwaj, Pankaj Sharma, Md Arif Khan, **Rohit Singh**, and Shaibal Mukherjee, *MgZnO based UV heterojunction photodetector fabricated using dual ion beam sputtering*, **19th International Workshop on The Physics of Semiconductor Devices (19th IWPSD), IIT Delhi, India**, December 11-15, 2017.
2. Md Arif Khan, **Rohit Singh**, Ritesh Bhardwaj, Abhinav Kranti, and Shaibal Mukherjee, *Enhanced sheet carrier density in ZnO based heterostructure by alloying cadmium in buffer layer ZnO*, **19th International Workshop on The Physics of Semiconductor Devices (19th IWPSD), IIT Delhi, India**, December 11-15, 2017.
3. Ritesh Bhardwaj, Pankaj Sharma, Md Arif Khan, **Rohit Singh**, and Shaibal Mukherjee, *Dual ion beam sputtering grown MgZnO based UV heterojunction photodetector*, **6th International Symposium on Integrated Functionalities, Shangri-La's Eros Hotel, Delhi, India,** December 10-13, 2017.
4. Md Arif Khan, **Rohit Singh**, Ritesh Bhardwaj, Abhinav Kranti, and Shaibal Mukherjee, *Cadmium Alloyed Buffer Layer ZnO Enhances Sheet Charge Density in ZnO Based Heterostructure Grown by Dual Ion Beam Sputtering*, **6th International Symposium on Integrated Functionalities, Shangri-La's Eros Hotel, Delhi, India**, December 10-13, 2017.
5. Amitesh Kumar, Mangal Das, **Rohit Singh**, Md Arif Khan, Biswajit Mandal, Abhinav Kranti, and Shaibal Mukherjee, *ZnO based resistive switching memory fabricated by Dual Ion Beam Sputtering with excellent endurance*, **6th International Symposium on Integrated Functionalities, Shangri-La's Eros Hotel, Delhi, India,** December 10-13, 2017.
6. Pankaj Sharma, Ritesh Bhardwaj, Amitesh Kumar, **Rohit Singh**, and Shaibal Mukherjee, *Fabrication of low resistive and stable Li-P co-doped p-type ZnO by dual ion beam sputtering*, **3rd International Conference on Smart Materials and Structures, Orlando, Florida, USA**, March 20-22, 2017.
7. Vishnu Awasthi, Vivek Garg, Brajendra S. Sengar, **Rohit Singh**, Sushil K. Pandey, Shailendra Kumar, C. Mukherjee, and Shaibal Mukherjee, *Band*

alignment study and plasmon generation at dual ion-beam sputtered Ga:ZnO/Ga:MgZnO heterojunction interface, **Compound Semiconductor Week 2016, Toyama, Japan**, June 26-30, 2016.

8. Pankaj Sharma, Ritesh Bhardwaj, **Rohit Singh**, and Shaibal Mukherjee, *Spectroscopic ellipsometric investigation of phosphorous doped p-type ZnO*, **7th International Conference on Spectroscopic Ellipsometry, Berlin, Germany**, June 6-10, 2016.
9. Pankaj Sharma, **Rohit Singh**, Ritesh Bhardwaj, and Shaibal Mukherjee, *Self-powered high photoresponse UV photodetector based on dual ion beam sputtered Ga-doped ZnO*, **Nanotech France 2016 and Joint International Conferences and Exhibition, Paris, France**, June 1-3, 2016.
10. Pankaj Sharma, **Rohit Singh**, Vishnu Awasthi, Vivek Garg, and Shaibal Mukherjee, *Self-powered high photoresponse Ga-doped ZnO ultraviolet photodetector*, **18th International Workshop on The Physics of Semiconductor Devices (18th IWPSD), IISc, Bangalore, India,** December 7-10, 2015.

B3. Book chapters

1. Md Arif Khan, **Rohit Singh**, and **Shaibal Mukherjee,** *Review of II-VI Based Compounds for Transistor Applications*, invited by Prof. Saleem Hashmi (editor-in-chief), **Reference Module in Materials Science and Materials Engineering,** Oxford: Elsevier, March 2018. DOI: 10.1016/B978-0-12-803581-8.10383-2

B4. Patent

1. *A method of fabricating high two dimensional electron gas density yielding zinc oxide heterostructures*

   Inventors: Shaibal Mukherjee, Abhinav Kranti, Md Arif Khan and **Rohit Singh**

   Patent No. 201721010866, March 27, 2017 (**Status: Published**)

TABLE OF CONTENTS

Chapter 1 Introduction

Chapter 8 Conclusion and Future Scope

LIST OF FIGURES

LIST OF TABLES

ACRONYMS

2DEG	*Two Dimensional Electron Gas*
2DHG	*Two Dimensional Hole Gas*
C-V	*Capacitance-Voltage*
DGD	*Double Gaussian Distribution*
DIBS	*Dual Ion Beam Sputtering*
DPC	*Deposition Chamber*
EDX	*Energy Dispersive X-Ray*
eV	*Electron Volt*
FESEM	*Field Emission Scanning Electron Microscopy*
FWHM	*Full Width at Half Maximum*
GaN	*Gallium Nitride*
HEMT	*High Electron Mobility Transistor*
HFET	*Heterojunction Field Effect Transistor*
HRTEM	*High Resolution Transmission Electron Microscopy*
I-V	*Current-Voltage*
LLC	*Load Lock Chamber*
MgO	*Magnesium Oxide*
SBH	*Schottky Barrier Height*
XRD	*X-Ray Diffraction*
ZnO	*Zinc Oxide*

NOMENCLATURE

a, c	Lattice constant
ε_o	Dielectric constant
e_{31}, e_{33}	Piezoelectric constant
C_{13}, C_{33}	Elastic stiffness constant
E_g	Energy gap
λ	Wavelength
μ_n	Electron mobility
μ_p	Hole mobility
ρ	Resistivity
V_H	Hall Voltage
P_{SP}	Spontaneous polarization
P_{PE}	Piezoelectric polarization
V_{OFF}	Threshold voltage
q	Elementary charge

ABSTRACT

Fabrication and Modelling of MgZnO/ZnO based Heterostructures to realize 2D Confinement of Electron Gas for HEMT Application

by

Rohit Singh

Hybrid Nanodevice Research Group, Discipline of Electrical Engineering

Indian Institute of Technology Indore

Supervisor: Dr. Shaibal Mukherjee

Co-Supervisors: Dr. Abhinav Kranti and Dr. Ajay Agarwal

ZnO has emerged as the subject of research for many electronic and optoelectronic applications in recent years because it is nontoxic, abundant, chemically stable, and biocompatible. Due to its direct wide band gap of 3.37 eV and a large exciton binding energy of 60 meV at room temperature, many researchers have explored it for devices like light emitting diode, photodetectors, lasers, and solar cells, etc. Due to the large spontaneous and piezoelectric polarization, ZnO based heterostructures are also being explored for two-dimensional electron gas (2DEG) density and applications in heterostructure field-effect transistors (HFETs). This is mainly due to the advantages it presents, such as high saturation velocity, low lattice mismatch, high conduction band offset, endurance to radiation damage, availability of native substrates, amenability to wet chemical processing, and feasibility of achieving high-quality films. In $Mg_xZn_{1-x}O$ alloy, the energy band gap and degree of polarization can be fine-tuned by varying the Mg molar composition. Moreover, as compared to other semiconductor materials such as GaN, SiC, and AlN, ZnO offers some fundamental advantages such as high breakdown strength and high-temperature operation.

In this research work, the 2DEG was realized in MgZnO/ZnO material system using Dual Ion Beam Sputtering (DIBS) system. The analytical model for the estimation of 2DEG density was also developed. My findings on MgZnO/ZnO material system finds application on the development of ZnO based heterostructure field effect transistors.

First of all, an analytical model for the estimation of 2DEG density was developed for graded MgZnO/ZnO heterostructures. Here, graded means MgZnO layers of different thickness and different Mg molar compositions deposited one over the other on the ZnO buffer layer. The developed model was based on the continuity of the electric field at the interfaces of different layers, dominant piezoelectric and spontaneous polarization components in different layers, Mg composition, and layers thickness. The developed generic model can be easily reduced for relatively simpler structures. Calculated 2DEG density (n_s) values suggest that the use of graded MgZnO layer significantly increases (2.3 times higher) the 2DEG density in MgZnO/ZnO heterostructure but at the expense of an increased threshold voltage (V_{OFF}). A graded structure with a lower thickness of layers was proposed, to achieve a compromise between high 2DEG density and V_{OFF}, based on the developed model.

After the development of an analytical model for the estimation of 2DEG density, the study of contact properties on MgZnO (barrier layer) layer was done with the aim of fabricating a good Schottky contact. For this, $Mg_{0.05}Zn_{0.95}O$ (MZO) film of 400 nm thickness was deposited using DIBS at 300 °C and 80 % Oxygen partial pressure. The *p*-Si (111) was used as the substrate. Various material characterizations including Hall, XRD, EDX, and spectroscopic ellipsometry were performed to investigate the film properties. Finally, Schottky contact was fabricated using DIBS at room temperature by depositing 100 nm thick and 12.38 μm^2 Gold contact using shadow masking techniques. The properties of Schottky contact was measured using temperature dependent *I-V* and *C-V* measurement. The Hall measurement demonstrates *n*-type conduction with resistivity, carrier concentration, and mobility of the MgZnO film as 0.12 Ω-cm, 6.05×10^{17}

cm^{-3}, and 85.12 $cm^2V^{-1}s^{-1}$, respectively at room temperature. XRD measurement demonstrates (002) crystal orientation of the film.

The apparent Schottky barrier height (SBH) and the ideality factor obtained from the *I-V* measurements were observed to increase and reduce, respectively, with increasing measurement temperature. That anomalous observation in the behavior of the SBH was in good agreement with the predictions of a double Gaussian distribution (DGD) of the inhomogeneous SBH at a metal-semiconductor (MS) interface. The values of the SBH as determined from *C-V* measurements were expectedly higher than those extracted from *I-V* measurements. The DGD model was observed to fit the experimentally obtained data for temperature dependent SBH with mean values of the SBH as 0.95 and 0.54 eV and standard deviations as 0.131 and 0.072 eV in the temperature range of 160-300 K and 80-160 K, respectively. The larger value of the SBH standard deviation confirms more SBH inhomogeneity at the MS interface, and those inhomogeneities were attributed to the presence of deep level or surface level interface states. The calculated interface states density was seen to vary from 6.46×10^{14} $eV^{-1}cm^{-2}$ at E_C-0.27 eV to 1.58×10^{14} $eV^{-1}cm^{-2}$ at E_C-0.74 eV, where E_C is the bottom of a conduction band at 300 K.

After the successful fabrication of Schottky contact on barrier layer MZO film, 2DEG density was successfully realized in MgZnO/ZnO based heterostructures fabricated by DIBS. All the layers of the heterostructures were deposited in the same ambient, i.e., at 300 °C and 60 % Oxygen partial pressure. The effect of variation of Mg composition, barrier layer thickness, and cap layer thickness on 2DEG density was studied. The value of n_s was found to be increasing with Mg composition for bilayer (MgZnO/ZnO) and capped (ZnO/MgZnO/ZnO) heterostructures, attaining values of 1.11×10^{14} cm^{-2} and 1.13×10^{14} cm^{-2} for x = 0.3 for the bilayer and capped heterostructure, respectively, from $\sim 5 \times 10^{12}$ cm^{-2} for the bare ZnO. The value of n_s initially increases and then saturates with the increase of barrier layer thickness in bilayer heterostructure keeping the Mg molar composition constant in the barrier layer. For the capped heterostructure

the n_s initially decreases and then saturates with the increase of cap layer thickness, provided, all other parameters are kept constant.

The source of electrons in 2DEG was also investigated, and the distinct roles of donor and acceptor states along with interface charges in 2DEG formation were analyzed. It was found that in case of sputter deposited samples, the dominant source of 2DEG electrons is interface charge.

The fabrication of source and drain contacts on top of MgZnO/ZnO heterostructures was also attempted by lithography and lift-off process for transistor application. The source and drain contacts on top of MgZnO/ZnO heterostructures were fabricated and characterized successfully by lift-off process which involves three lithography steps. The Au/Ti was used for source and drain ohmic contacts in which first of all 10 nm of Ti was deposited and then 200 nm of Au. To prove the ohmic nature of these contacts the current vs. voltage measurement was taken and was found to be linear. The gate contact of Pt/Ti was also attempted on top of MgZnO/ZnO heterostructure using lift-off. But the two lift-off attempts of gate metallization failed and hence remains as future course of action to realize reliable gate.

Chapter 1

Introduction

Recently, zinc oxide (ZnO) and its heterostructures have emerged as promising materials for thin-film transistors, solar cells, biocompatible devices, ultraviolet (UV) light emitting diodes, and lasers [1]–[3]. ZnO-based heterostructures are also being explored for two-dimensional electron gas (2DEG) density and its prospective applications in heterostructure field-effect transistors (HFETs) [4]–[6]. This is mainly due to the advantages offered by these heterostructures such as high saturation velocity, low lattice mismatch, high conduction band offset, endurance to radiation damage, availability of native substrates, amenability to wet chemical processing, and feasibility of achieving high-quality films [4], [5]. For example, in $Mg_xZn_{1-x}O$ alloy, the energy band gap and the degree of polarization can be fine-tuned by varying the Mg molar composition [4]. The formation of 2DEG in single-crystalline MgZnO/ZnO systems have been reported in many published literature [4], [7], [8], [9]; however, reports on such 2DEG formation in polycrystalline MgZnO/ZnO systems are limited [5]. It is reported that the polarization effect induces a high sheet carrier concentration, thereby significantly enhancing the electrical conductance of high-quality single crystalline or polycrystalline systems. However, such enhancement in conductance is mostly demonstrated by molecular beam epitaxy (MBE) [4], pulsed-laser deposition (PLD) [7], or metal organic vapor phase epitaxy (MOVPE) [8], which are not suitable for low-cost, large-area electronic applications. Hence, new techniques need to be developed for the fabrication of 2DEG in polycrystalline MgZnO/ZnO system for low-cost and large area electronic applications.

The main purpose of this research work is the realization of 2DEG in MgZnO/ZnO heterostructure using dual ion beam sputtering (DIBS) system for high electron mobility transistor (HEMT) applications. The DIBS system produces high quality thin films with reasonably superior compositional stoichiometry, uniformity, and better film adhesion on a larger substrate surface area. Other prime features of the DIBS system are

high-quality growth with a reduced surface roughness on a larger substrate area, *in situ* substrate pre-cleaning before carrying out the growth process, and *in situ* post-growth annealing. In this thesis, initially, an analytical model is developed for the estimation of 2DEG density in MgZnO/ZnO heterostructures. Thereafter, a reliable and stable gold (Au) Schottky contact is fabricated on MgZnO using DIBS which is very crucial for HEMT and thin film transistor fabrication. Afterwards, the growth conditions of the undoped ZnO buffer layer and doped *n*-type MgZnO barrier layer by DIBS were optimized. Hall measurements, X-Ray diffraction (XRD), high-resolution transmission electron microscopy (HRTEM), energy dispersive X-Ray (EDX), and *C–V* measurements were carried out to determine and correlate the elemental, electrical, and crystalline properties of these films, respectively. Subsequently, the fabrication of 2DEG in polycrystalline MgZnO/ZnO based heterostructure was carried out by DIBS system.

This chapter demonstrates a summarizing description of basic properties of ZnO, MgZnO/ZnO heterostructure, and its advantages which are very useful for realization of 2DEG and HEMT application.

1.1 Background

Since the last decade, ZnO is being considered as a potential candidate for heterostructure field effect transistor (HFET) due to several advantages over the GaN-based material system. The recent diverse heterostructures which are used for HFETs are MgZnO/ZnO and AlGaN/GaN heterostructures. The AlGaN/GaN heterostructure is one of the prime competitors of MgZnO/ZnO heterostructures. Nowadays, the interest on the development of MgZnO/ZnO heterostructure based HFET has increased due to its several advantages over its prime competitor, AlGaN/GaN. The advantages of MgZnO/ZnO material system over AlGaN/GaN material system are as follows, (i) higher saturation velocity, (ii) lower (heterojunction) lattice mismatch, (iii) larger conduction band

offset (ΔE_C) for MgZnO/ZnO heterostructure, and (iv) the possibility of the use of bulk (ZnO) substrates [10], [11].

To fabricate the MgZnO/ZnO heterostructure based HFETs, the carrier confinement in the potential well formed at MgZnO/ZnO heterointerface is of great importance. The reason for the potential well formation at MgZnO/ZnO heterointerface is discussed in the later section of this chapter. The first time demonstration of two dimensional electron gas (2DEG) in MgZnO/ZnO heterostructure was published and demonstrated in 2004 by Koike *et al.* [12]. The fabrication of this heterostructure was done by MBE. The detailed study of the effect of variation of Mg composition and thickness of MgZnO layer on 2DEG density in MgZnO/ZnO heterostructures grown by MBE was done by Tampo *et al.* [4], [13]. Thereafter, 2DEG in MgZnO/ZnO heterostructures deposited by single crystalline growth techniques is reported by many researchers [8], [14]–[17]. The realization of 2DEG in sputter deposited MgZnO/ZnO heterostructures is still very challenging. Only a few researchers have obtained 2DEG in sputter deposited heterostructures. In 2010, for the first time, 2DEG was obtained in sputter deposited MgZnO/ZnO heterostructure by Chin *et al.* [5]. Still, the detailed study of 2DEG formation in sputter deposited MgZnO/ZnO heterostructure is lagging in the literature and require a significant amount of research to be done in this regard.

1.2 ZnO: The material

1.2.1 Structural Properties

Zinc oxide crystallizes in two main forms, hexagonal wurtzite [18] and cubic zincblende [19]. Crystallographically the atomic arrangement of zincblende structure is quite similar to that of the wurtzite structure, only the angle of adjacent tetrahedral units is different, having values of 60° for zincblende and 0° for wurtzite phase [20]. For a clear layout of these structural phases, the basic crystal structures of wurtzite and zincblende ZnO are represented schematically in Fig. 1.1. The O atom is marked in the schematic with yellow circles, and another one is the Zn atom.

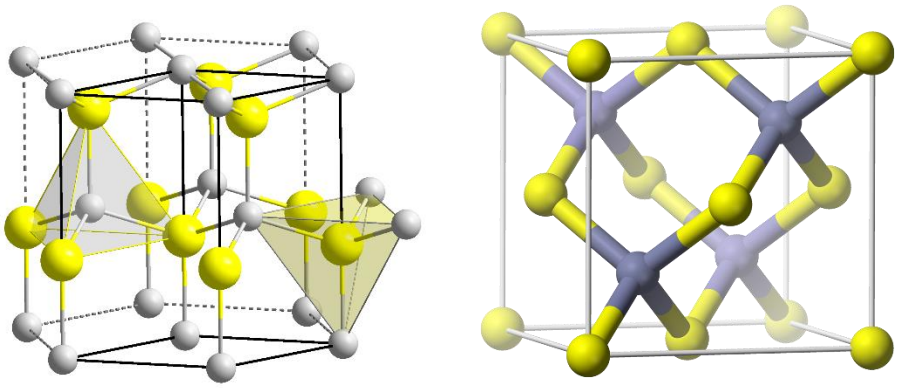

(a) (b)

Fig. 1.1: The schematic representation of ZnO crystal structures: (a) wurtzite and (b) zincblende.

Among these two structures, wurtzite structure is most stable thermodynamically at ambient conditions and thus most common. This is because its ionicity that resides exactly at the borderline between the covalent and the ionic materials. At room temperature (RT) the hexagonal wurtzite ZnO has lattice parameters a = 3.25 Å and c = 5.20 Å [21]. The polarity observed in the ZnO crystal is due to the tetrahedral structure. ZnO has four common surfaces, the polar Zn (0001) and O ($000\bar{1}$) terminated faces, and the non-polar (1120) and (1010) faces. The (1120) and (1010) surfaces contain equal numbers of Zn and O atoms [11]. At relatively modest external hydrostatic pressures wurtzite ZnO can be transformed to the rocksalt (NaCl) like other II-VI semiconductors [22]. As compared to the wurtzite structure zincblende structure has lower ionicity, this leads to the lower carrier scattering and higher doping efficiencies [20].

1.2.2 Electrical Properties

ZnO has a relatively large direct band gap of ~3.37 eV at room temperature [11]. Advantages associated with a large band gap include higher breakdown voltages, ability to sustain large electric fields, lower electronic noise, and high-temperature and high-power operation. The bandgap of

ZnO can further be tuned by alloying with magnesium oxide (MgO). These properties make it suitable for high frequency and high power applications.

The thermal conductivity and dielectric constant of ZnO are 0.6 Wcm^{-1} [23] and 8.75 [8], respectively. The thermal conductance of the material defines the ease with which power can be dissipated from the device which, otherwise, would result in higher chip temperatures and degraded performance. Having high thermal conductivity, ZnO is suitable for integrated circuits fabrication. The dielectric constant indicates the capacitive loading capability of a transistor and affects the device terminal impedances [24]. The dielectric constant of wide band-gap semiconductors is about 20% lower than the conventional semiconductors which permit them to be about 20% larger in the area for a given impedance. The increased area allows for higher radio frequency (RF) currents and therefore higher RF power. Comparing the dielectric constant of ZnO with GaN (8.9) [25] and GaAs (12.46) [26], ZnO has a lower value which makes it more suitable for RF applications.

Band-gap and other electrical properties of ternary oxides like MgZnO can be computed by interpolation using Vegard's law given by the formula [27],

$$P(Mg_xZn_{1-x}O) = xP(MgO) + (1-x)P(ZnO) + bx(1-x) \quad (1.1)$$

where $P(x)$ represents the electrical property to be interpolated and b represents the bowing parameter which has to be experimentally determined for accurate interpolation.

1.3 MgZnO/ZnO: The heterostructure

1.3.1 Hetero-structure: Band Gap Discontinuity

A heterostructure is formed when two different materials are joined together or grown one over the other keeping the same crystal structure. When such a heterojunction is formed between two materials having a large band gap difference, an energy discontinuity is created in the band diagram.

Fig. 1.2 visualizes the band diagram of MgZnO/ZnO heterostructure before and after the junction formation. As can be seen from the figure, the band gap discontinuity results in the formation of a notch in the conduction band at the interface and a valley in the valence band, both of which are present in the lower band gap material which, in the present case, is ZnO. The quality of the junction formed between such materials depends upon the difference between their lattice constants. The larger the difference in lattice constant of two materials, the larger is the possibility of the interface defects. The matching of lattice constant is the primary requirement for the formation of a good hetero-junction and hence, a good hetero-structure based device. If the materials to be joined are MgZnO and ZnO, the parameter to be considered is the fraction of magnesium, as it defines the bandgap and lattice constant of MgZnO. Bandgap discontinuity (ΔEg) is given by the difference in the band gap of two materials. Conduction band discontinuity (ΔEc) is calculated by locating the position of neutral levels in the material. In MgZnO/ZnO heterostructure cases, it is calculated as $\Delta Ec = 0.9\Delta Eg$ [11]. The value ΔEc defines the depth of the notch, sometimes termed as Quantum Well, as electrons are confined into quantum levels. The relative position of this notch with respect to the Fermi level in the lower band gap material and its corresponding depth determines the density of charge carriers, and hence, the operation of any device using the heterojunction 2DEG [11].

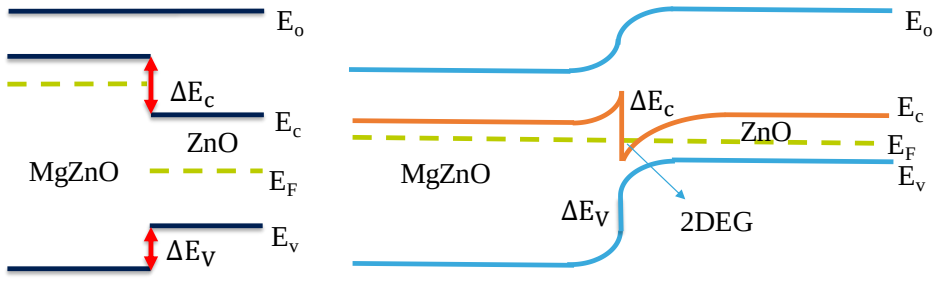

Fig. 1.2: Energy Band diagram for MgZnO/ZnO Heterostructure, (a) before junction formation and (b) after junction formation at thermo-dynamic equilibrium condition.

1.3.2 Polarization in MgZnO/ZnO: 2 Dimensional Electron Gas (2DEG)

In case of ZnO based devices, the principle behind the formation of 2DEG is the inherent net polarization, resulting in interface charge without the presence of any significant doping which further enhances their mobility. It is to be noted, ZnO material possesses an inherent spontaneous polarization whose direction depends on the growth face of the crystal (Zn or O at the surface). Since the ZnO substrate is comparatively thicker, it is formed in a relaxed state while the MgZnO is under stress. Thus, in addition to spontaneous polarization, the strain developed in the MgZnO results in a piezo-electric polarization in MgZnO. When MgZnO is grown over the ZnO substrate, due to the difference in their polarization, a net polarization charge develops at the interface depending, again, on the face of the growth of the crystal as shown in Fig. 1.3. Although it is clear that there is a positive charge at the interface of the MgZnO/ZnO heterostructure, the device has to be neutral as a whole. The positive charge must be compensated by the equal negative charge. In order to compensate for the positive charge, electrons accumulate at the interface, and due to the presence of a notch at the heterojunction, they form a 2DEG close to the interface.

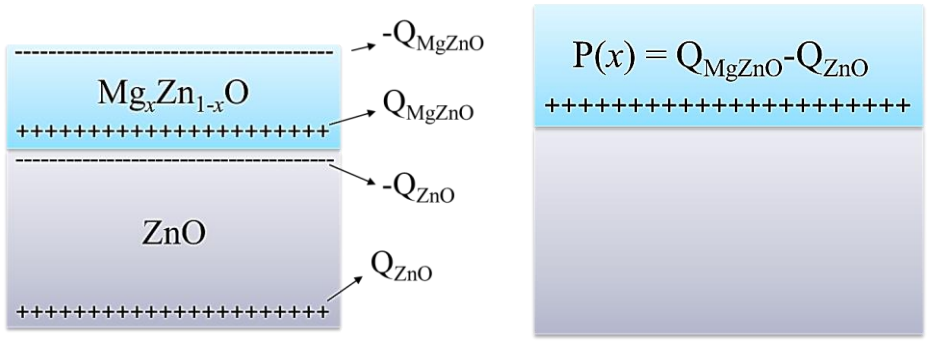

(a) (b)

Fig. 1.3: Polarization charge in MgZnO/ZnO Heterostructure, a) Charge polarization in individual materials, Q_{MgZnO} in MgZnO is the sum of both Spontaneous and piezo-electric polarization, Q_{ZnO} in ZnO is only Spontaneous polarization as ZnO has been assumed to be relaxed, b) Total sum of all the polarization results in a net positive charge at the interface.

1.4 MgZnO/ZnO: HEMT fabrication challenges

Every good thing comes at some price. This applies to ZnO technology too. The major challenges in the fabrication of MgZnO/ZnO based HEMT are as follows.

(i) The fabrication of single crystalline or polycrystalline layers of MgZnO over ZnO in which 2DEG is formed.

(ii) Fabrication of ohmic contacts for source and drain with less contact resistance on wide bandgap MgZnO top surface.

(iii) Fabrication of stable and reliable Schottky contact for the gate.

The fabrication of stable ohmic and Schottky contacts on the MgZnO top surface is challenging since certain metals like Au and Ag change their nature of contact with time [28].

Apart from this, ZnO may have certain other challenges when it comes to the full fabrication of HEMT because till now nobody has developed a full prototype of HEMT made of MgZnO/ZnO heterostructures.

1.5 Aim and Objectives

The main aim of this thesis is to realize 2DEG in MgZnO/ZnO heterostructure for HEMT using sputtering techniques as the sputtering technique is low cost and used for large area fabrication. This task includes the following objectives:

(a) As an initial step, a physics-based analytical model is developed for the estimation of 2DEG density in different configuration of MgZnO/ZnO heterostructure.

(b) The result of the simulated data of the developed model is compared with the published data in the literature.

(c) A reliable and stable Au Schottky contact is fabricated on MgZnO using DIBS which is very crucial for HEMT and thin film transistor fabrication.

(d) The optimization of the growth conditions of the undoped ZnO buffer layer and doped *n*-type MgZnO barrier layer by DIBS are done.

(e) 2DEG is realized in MgZnO/ZnO heterostructures by DIBS and the effect of variation of Mg composition, barrier layer thickness, and cap layer thickness on 2DEG density is also studied which will help in the optimization of 2DEG density.

(f) The source of electrons in 2DEG in sputtered deposited MgZnO/ZnO heterostructures is investigated.

(g) Source and drain contact of Au/Ti is fabricated on top of MgZnO/ZnO heterostructures using lithography.

1.6 Organization of the thesis

The research in this thesis is focused on the realization of 2DEG in MgZnO/ZnO heterostructures using sputtering for HEMT. The thesis is organized as follows:

Chapter 2 describes the deposition and characterization systems employed for MgZnO/ZnO heterostructures. The used systems are DIBS system, X-Ray Diffraction, Variable Angle Variable Wavelength Spectroscopic Ellipsometry, Four Probe Hall, *I-V*, and *C-V* measurements, Energy-dispersive X-Ray Spectroscopy, and High-Resolution Transmission Electron Microscopy.

Chapter 3 provides a physics-based analytical model for the estimation of 2DEG density in different configurations of MgZnO/ZnO heterostructures. Factors largely affecting the 2DEG density are Mg composition in MgZnO layer and thickness of different layers; were optimized and examined in detail. The purpose is to maximize 2DEG density through these parameters optimization.

Chapter 4 explains the fabrication of stable and reliable Au Schottky contact on MgZnO. The detailed study of temperature dependent *I-V* and *C-V* characteristics are done.

Chapter 5 describes the realization of 2DEG in MgZnO/ZnO heterostructures. The effect of variation of Mg composition, barrier layer thickness, and cap layer thickness on 2DEG density is studied.

Chapter 6 describes the roles of surface states and interface states on the formation of 2DEG in sputtered deposited MgZnO/ZnO heterostructures.

Chapter 7 describes the fabrication of source and drain contacts on top of MgZnO/ZnO heterostructures using lift-off process for transistor application.

Chapter 8 draws conclusions from the thesis and proposes the scope for future works for the continuation of the research.

1.7 References

[1] K. Ramanathan, M. A. Contreras, C. L. Perkins, S. Asher, F. S. Hasoon, J. Keane, D. Young, M. Romero, W. Metzger, R. Noufi, J. Ward, and A. Duda, "Properties of 19.2% efficiency ZnO/CdS/CuInGaSe2 thin-film solar cells," *Prog. Photovoltaics Res. Appl.*, vol. 11, no. 4, pp. 225–230, Jun. 2003.

[2] D. M. Bagnall, Y. F. Chen, Z. Zhu, T. Yao, S. Koyama, M. Y. Shen, and T. Goto, "Optically pumped lasing of ZnO at room temperature," *Appl. Phys. Lett.*, vol. 70, no. 17, pp. 2230–2232, Apr. 1997.

[3] Y.-S. Choi, J.-W. Kang, D.-K. Hwang, and S.-J. Park, "Recent Advances in ZnO-Based Light-Emitting Diodes," *IEEE Trans. Electron Devices*, vol. 57, no. 1, pp. 26–41, Jan. 2010.

[4] H. Tampo, H. Shibata, K. Maejima, A. Yamada, K. Matsubara, P. Fons, S. Kashiwaya, S. Niki, Y. Chiba, T. Wakamatsu, and H. Kanie, "Polarization-induced two-dimensional electron gases in ZnMgO/ZnO heterostructures," *Appl. Phys. Lett.*, vol. 93, no. 20, p. 202104, Nov. 2008.

[5] H.-A. Chin, I.-C. Cheng, C.-I. Huang, Y.-R. Wu, W.-S. Lu, W.-L.

Lee, J. Z. Chen, K.-C. Chiu, and T.-S. Lin, “Two dimensional electron gases in polycrystalline MgZnO/ZnO heterostructures grown by rf-sputtering process,” *J. Appl. Phys.*, vol. 108, no. 5, p. 54503, Sep. 2010.

[6] B.-S. Wang, Y.-S. Li, and I.-C. Cheng, “Mobility Enhancement in RF-Sputtered MgZnO/ZnO Heterostructure Thin-Film Transistors,” *IEEE Trans. Electron Devices*, vol. 63, no. 4, pp. 1545–1549, Apr. 2016.

[7] A. K. Das, P. Misra, R. S. Ajimsha, M. P. Joshi, and L. M. Kukreja, “Effects of electron interference on temperature dependent transport properties of two dimensional electron gas at MgZnO/ZnO interfaces,” *Appl. Phys. Lett.*, vol. 107, no. 10, p. 102104, Sep. 2015.

[8] J. D. Ye, S. Pannirselvam, S. T. Lim, J. F. Bi, X. W. Sun, G. Q. Lo, and K. L. Teo, “Two-dimensional electron gas in Zn-polar ZnMgO/ZnO heterostructure grown by metal-organic vapor phase epitaxy,” *Appl. Phys. Lett.*, vol. 97, no. 11, p. 111908, Sep. 2010.

[9] K. Ding, M. B. Ullah, V. Avrutin, Ü. Özgür, and H. Morkoç, “Investigation of high density two-dimensional electron gas in Zn-polar BeMgZnO/ZnO heterostructures,” *Appl. Phys. Lett.*, vol. 111, no. 18, p. 182101, Oct. 2017.

[10] J. D. Albrecht, P. P. Ruden, S. Limpijumnong, W. R. L. Lambrecht, and K. F. Brennan, “High field electron transport properties of bulk ZnO,” *J. Appl. Phys.*, vol. 86, no. 12, pp. 6864–6867, Dec. 1999.

[11] H. Tampo, K. Matsubara, A. Yamada, H. Shibata, P. Fons, M. Yamagata, H. Kanie, and S. Niki, “High electron mobility Zn polar ZnMgO/ZnO heterostructures grown by molecular beam epitaxy,” *J. Cryst. Growth*, vol. 301–302, no. SPEC. ISS., pp. 358–361, Apr. 2007.

[12] K. Koike, K. Hama, I. Nakashima, G. Takada, M. Ozaki, K. Ogata, S. Sasa, M. Inoue, and M. Yano, “Piezoelectric Carrier Confinement by Lattice Mismatch at ZnO/Zn $_{0.6}$ Mg $_{0.4}$ O Heterointerface,” *Jpn.*

J. Appl. Phys., vol. 43, no. No. 10B, pp. L1372–L1375, Oct. 2004.

[13] H. Tampo, H. Shibata, K. Matsubara, A. Yamada, P. Fons, S. Niki, M. Yamagata, and H. Kanie, "Two-dimensional electron gas in Zn polar ZnMgO/ZnO heterostructures grown by radical source molecular beam epitaxy," *Appl. Phys. Lett.*, vol. 89, no. 13, p. 132113, Sep. 2006.

[14] M. Yano, K. Hashimoto, K. Fujimoto, K. Koike, S. Sasa, M. Inoue, Y. Uetsuji, T. Ohnishi, and K. Inaba, "Polarization-induced two-dimensional electron gas at Zn1−xMgxO/ZnO heterointerface," *J. Cryst. Growth*, vol. 301–302, no. SPEC. ISS., pp. 353–357, Apr. 2007.

[15] S. Sasa, T. Hayafuji, M. Kawasaki, K. Koike, M. Yano, and M. Inoue, "Performance and Stability of ZnO/ZnMgO Hetero-Metal–Insulator–Semiconductor Field-Effect Transistors," *Jpn. J. Appl. Phys.*, vol. 47, no. 4, pp. 2845–2847, Apr. 2008.

[16] M. Brandt, H. von Wenckstern, G. Benndorf, H. Hochmuth, M. Lorenz, and M. Grundmann, "Formation of a two-dimensional electron gas in ZnO/MgZnO single heterostructures and quantum wells," *Thin Solid Films*, vol. 518, no. 4, pp. 1048–1052, Dec. 2009.

[17] E. Baghani and S. K. O'Leary, "An enhancement in the low-field electron mobility associated with a ZnMgO/ZnO heterostructure: The role of a two-dimensional electron gas," *J. Appl. Phys.*, vol. 114, no. 2, p. 23703, Jul. 2013.

[18] S. K. Pandey, S. Kumar Pandey, V. Awasthi, M. Gupta, U. P. Deshpande, and S. Mukherjee, "Influence of in-situ annealing ambient on p-type conduction in dual ion beam sputtered Sb-doped ZnO thin films," *Appl. Phys. Lett.*, vol. 103, no. 7, p. 72109, Aug. 2013.

[19] G. H. Lee, T. Kawazoe, and M. Ohtsu, "Room temperature near-field photoluminescence of zinc-blend and wurtzite ZnO structures," *Appl. Surf. Sci.*, vol. 239, no. 3–4, pp. 394–397, Jan. 2005.

[20] A. Ashrafi and C. Jagadish, “Review of zincblende ZnO: Stability of metastable ZnO phases,” *J. Appl. Phys.*, vol. 102, no. 7, p. 71101, Oct. 2007.

[21] H. Tampo, P. Fons, A. Yamada, K.-K. Kim, H. Shibata, K. Matsubara, S. Niki, H. Yoshikawa, and H. Kanie, “Determination of crystallographic polarity of ZnO layers,” *Appl. Phys. Lett.*, vol. 87, no. 14, p. 141904, Oct. 2005.

[22] V. L. Solozhenko, O. O. Kurakevych, P. S. Sokolov, and A. N. Baranov, “Kinetics of the Wurtzite-to-Rock-Salt Phase Transformation in ZnO at High Pressure,” *J. Phys. Chem. A*, vol. 115, no. 17, pp. 4354–4358, May 2011.

[23] X. Wu, J. Lee, V. Varshney, J. L. Wohlwend, A. K. Roy, and T. Luo, “Thermal Conductivity of Wurtzite Zinc-Oxide from First-Principles Lattice Dynamics – a Comparative Study with Gallium Nitride,” *Sci. Rep.*, vol. 6, no. 1, p. 22504, Apr. 2016.

[24] U. K. Mishra, P. Parikh, and Yi-Feng Wu, “AlGaN/GaN HEMTs-an overview of device operation and applications,” *Proc. IEEE*, vol. 90, no. 6, pp. 1022–1031, Jun. 2002.

[25] N. Karumuri, S. Turuvekere, N. Dasgupta, and A. Dasgupta, “A Continuous Analytical Model for 2-DEG Charge Density in AlGaN/GaN HEMTs Valid for All Bias Voltages,” *IEEE Trans. Electron Devices*, vol. 61, no. 7, pp. 2343–2349, Jul. 2014.

[26] W. J. Moore and R. T. Holm, “Infrared dielectric constant of gallium arsenide,” *J. Appl. Phys.*, vol. 80, no. 12, pp. 6939–6942, Dec. 1996.

[27] S. T. Murphy, A. Chroneos, C. Jiang, U. Schwingenschlögl, and R. W. Grimes, “Deviations from Vegard’s law in ternary III-V alloys,” *Phys. Rev. B*, vol. 82, no. 7, p. 73201, Aug. 2010.

[28] M. W. Allen and S. M. Durbin, “Influence of oxygen vacancies on Schottky contacts to ZnO,” *Appl. Phys. Lett.*, vol. 92, no. 12, p. 122110, Mar. 2008.

Chapter 2

Systems for Fabrication and Characterization of MgZnO/ZnO based Heterostructures

In the advancement of science and technology, the discovery of novel materials those are having varied characteristics and applications have played an important role. In this chapter, the equipment has been briefly described used for the growth and characterization of MgZnO/ZnO heterostructures. For the heterostructure deposition, Dual Ion Beam Sputtering (DIBS) system has been used. Different characterization techniques were utilized to evaluate their structural, elemental, and electrical properties of these heterostructures. The crystal structure of the samples was characterized using X-Ray diffraction (XRD) system. The electrical properties of these heterostructures were characterized by Hall, *I-V*, and *C-V* measurement. The atomic composition of the different elements present in samples was investigated by energy dispersive X-Ray (EDX). The quality of the material interface of the MgZnO/ZnO was investigated by high-resolution transmission electron microscopy (HRTEM) measurement. These systems were discussed in details in this chapter of the thesis.

2.1 Growth Equipment

The DIBS system is used for thin films growth and MgZnO/ZnO heterostructures fabrication in this research work. The DIBS system is explained concisely in the following section.

2.1.1 Dual Ion Beam Sputtering System

Dual Ion Beam Sputtering System is a very effective physical vapor deposition technique for thin film deposition as well as fabrication of electronics and optoelectronics devices in ultrahigh vacuum conditions [1]. DIBS system is equipped with *radio-frequency* (RF) deposition ion beam source and *direct-coupled* assist ion source as shown in Fig. 2.1. The

deposition ion source is deployed to sputter materials from a target fixed in a four target assembly, and the assist ion source is implemented to pre-clean the substrate surface before film deposition and to hinder island formation and remove weak dangling bonds during the actual sputtering process [2]. The angle between the deposition ion source and the sputtering target is fixed at 45^{o} off normal while the angle between the assist ion source and the substrate is maintained at 60^{o}. A few other unique features of the DIBS system are high-quality growth with reduced surface roughness, increased growth uniformity on a larger substrate area and in-situ substrate pre-cleaning before growth. The system consists of a single process chamber with automatic substrate loading. The actual image of a dual ion beam sputtering system is shown in Fig. 2.2. The main components of this system are deposition ion source, assist ion source, a deposition chamber, load lock chamber, vacuum pumps, vacuum gauges, heater assembly, water chiller and controlling unit [2].

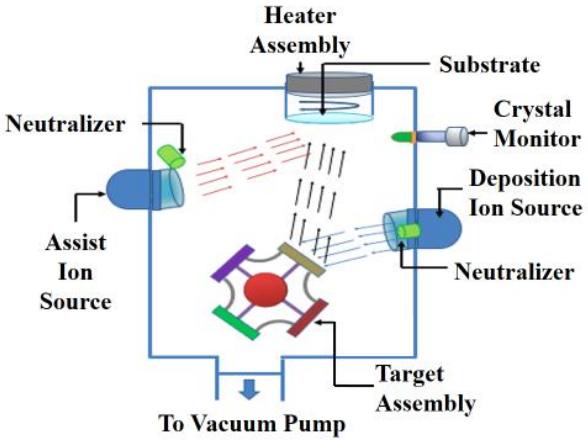

Fig. 2.1: Schematic illustration of DIBS system.

Fig. 2.2: The actual image of DIBS System.

In the DIBS system, Kauffman Robinson ion sources are used, which produces a positive ion beam, which is spatially well confined and mono-energetic [3]. Essentially, an ion beam source is a plasma source fitted with a set of grids enabling a stream of ions to be extracted. The deposition ion source has three main parts: the discharge chamber, grids, and neutralizer. Ions are produced in the discharge chamber by subjecting a gas (usually Argon) to an RF field. The gas is fed into a quartz or alumina chamber with an RF powered coil around it. The RF field excites free electrons until they have enough energy to break gas atoms into ions and electrons; this is referred to as "inductive coupling." The gas is thus ionized, and plasma is established. These ions are extracted as the beam from the discharge chamber by applying various voltages on grids. Deposition source consists of three-grids to extract ions and to reduce the beam spread. The neutralizer (hollow cathode electron source) is used in the deposition source assembly to neutralize the positive ion beam [3]. The schematic diagram of the deposition ion source is shown in Fig. 2.3.

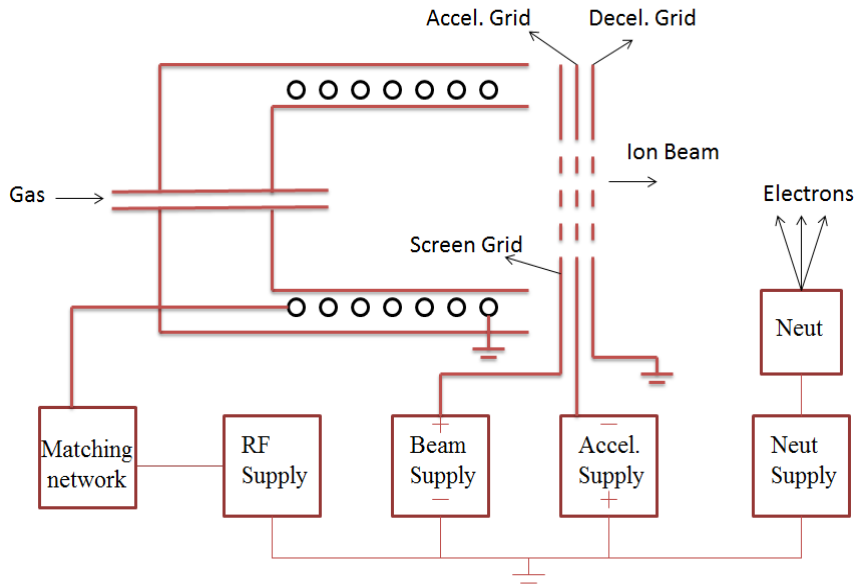

Fig. 2.3: Schematic illustration of the deposition ion beam source.

The assist ion source consists of mainly End-Hall 400 ion source module and hallow-cathode neutralizer assembly. This system has three types of power supplies (1) Keeper power supply (2) Emission power supply (3) Discharge power supply. A keeper and emission power supply are used for hollow cathode neutralizer. Discharge power supply provides voltage and current to End-Hall 400 ion source module. The assist ion source has the natural advantages of lower cost, broad ion-beam coverage, and greater reliability. The assist ion source also has much larger ion-current capabilities at low ion energies (200 eV and less) permitting useful etch rates [2]. Fig. 2.4 shows the schematic diagram of the assist ion source. The discharge power supply provides voltage and current to the anode of the End-Hall 400 ion source module and produces a positive ion beam. The keeper power supply provides voltage and current to the hollow cathode neutralizer, for igniting the hollow cathode and keeping the cathode hot enough for thermionic emission of electrons [2]. The emission power supply provides a negative voltage to the hollow cathode after it is ignited by the keeper power supply and controls the electron beam emitted from the hollow cathode neutralizer to neutralize the positive ion beam of End-Hall 400 ion source.

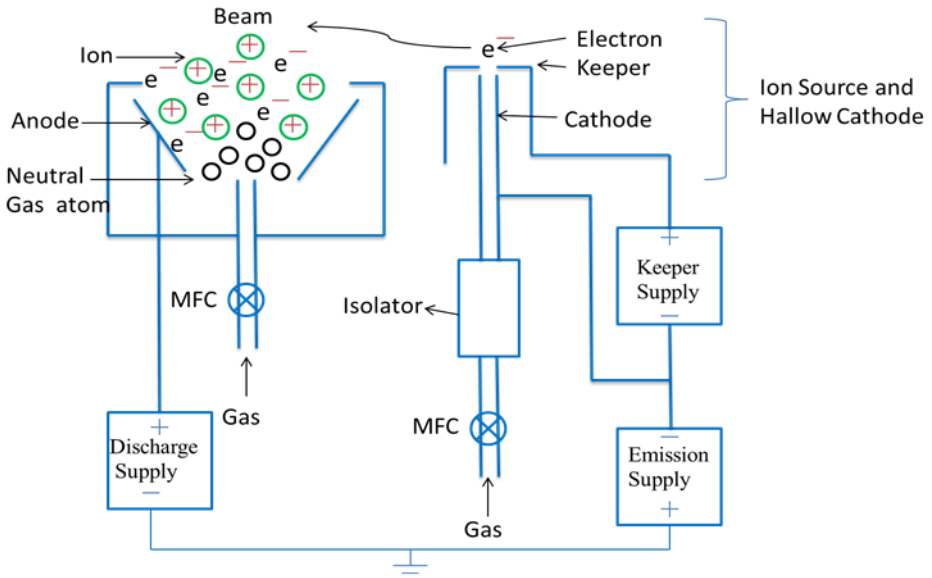

Fig. 2.4: Schematic illustration of assist ion source.

The deposition chamber of DIBS is known as the main chamber in which growth processes were performed. It is mostly made up of stainless steel or Pyrex glass as these materials are non-corrodible, non-magnetic, easy to weld and clean, highly malleable and have good outgassing characteristics [2]. The chamber has typically a large number of ports, i.e., for the pumping system, gas inlets; pressure monitoring, substrate loading, ion beam sources, and viewports. The load lock chamber is used to load the substrate into the deposition chamber by a robotic arm. A set of rotary and turbomolecular vacuum pumps are used for creating an ultra-high vacuum inside the deposition chamber and load lock chamber. Vacuum gauges are used to measure the vacuum level in the deposition and load lock chamber. The background pressure inside the deposition chamber and the load lock chamber are maintained at 10^{-8} mbar and 10^{-9} mbar respectively. The heater assembly above the deposition chamber is used to heat the sample from room temperature to 1000 °C during growth as well as annealing processes. The water chiller is employed to remove heat from the deposition chamber, target assembly, and vacuum pumps. DIBS system growth parameters, i.e., deposition temperature, gas pressure, gas composition and RF power are controlled by the parameter controlling unit of the DIBS system [1], [2].

In this research work, the growth of undoped ZnO, Ga-doped MgZnO thin films, and the fabrication of ZnO-based heterostructures was performed by Elettrorava DIBS system [1], [2].

2.2 Characterization Techniques

The equipment used for the characterization of thin films and heterostructures in this research work are demonstrated briefly in the following sections.

2.2.1 Hall Measurement System

The electrical transport properties of the MgZnO thin films and MgZnO/ZnO heterostructures were characterized by Hall Effect measurements using the Van der Pauw configuration. The Hall Effect provides a relatively simple way of determining the type of semiconductor, measuring the carriers (electrons and holes) concentration, electrical resistivity, and the mobility of carriers in semiconductors. When a current-carrying semiconductor is kept in a magnetic field, the charge carriers of the semiconductor experience a force in a direction perpendicular to both the magnetic field and the current. At equilibrium, a voltage appears at the semiconductor edges. The appeared voltage at the semiconductor edge is called as Hall voltage (V_H). The V_H determination is the first step to determine the type of semiconductor and the carrier concentration in the semiconductor. Once the V_H is determined the sheet carrier concentration of the semiconductor is determined by [4]

$$n_S = \frac{IB}{q|V_H|} \tag{2.1}$$

Where I is the current flowing in the semiconductor, B is the applied magnetic field and q is the elementary charge. For the determination of bulk carrier concentration, accurate measurement of the thickness of the sample (d) is required since bulk carrier concentration is the product of sheet carrier concentration and thickness of the film/sample. If the Van der Pauw configuration is used for the measurement, then for *n*-type sample V_H is

negative, and for the *p*-type sample, the V_H is positive [4]. Different sample geometry with contact placements as shown in Fig. 2.5 is used in Van der Pauw configuration.

The sheet resistance R_S of the semiconductor can be conveniently determined by use of the Van der Pauw resistivity measurement technique [5].

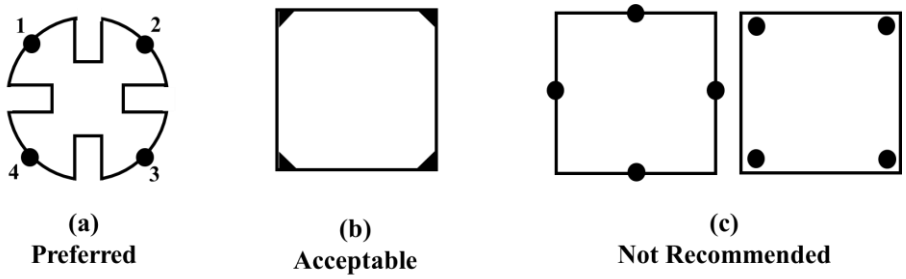

Fig. 2.5: Some possible contact placement in Van der Pauw configuration.

The Hall mobility of the semiconductor is measured with the help of sheet carrier concentration and sheet resistance and is given by the relation

$$\mu = \frac{1}{qn_S R_S} \tag{2.2}$$

Fig. 2.6 is showing the photographic image of our Hall measurement setup installed in our laboratory. Our setup includes a solenoidal magnet with a maximum strength of 1 Tesla magnetic field strength, a gauss meter, sample holder, and source meter (Keithley 2612 A).

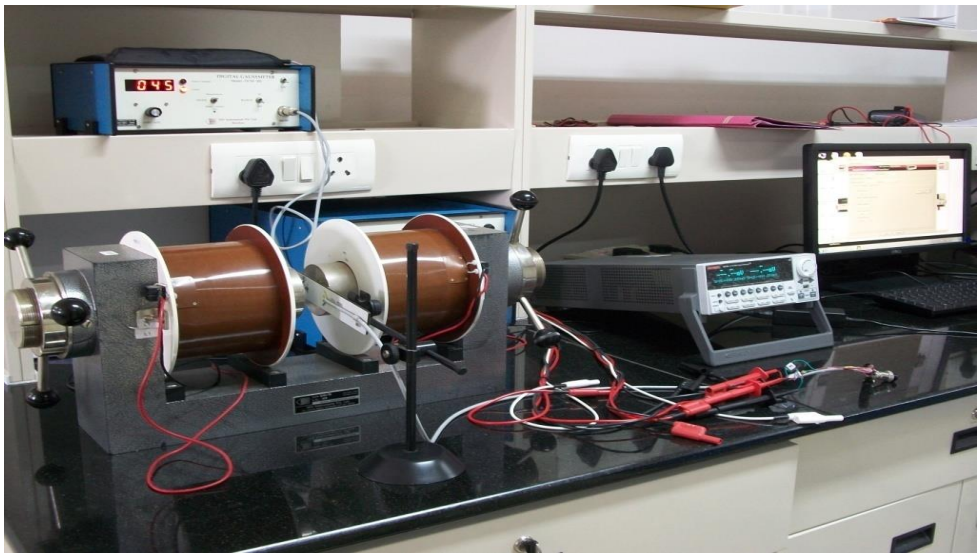

Fig. 2.6: Photographic image of Hall measurement system installed in our laboratory.

In this research work, the electrical properties, i.e., resistivity, sheet carrier concentration and mobility of MgZnO thin film, undoped ZnO, and MgZnO/ZnO heterostructure were measured using Hall measurement setup in Van der Pauw geometry using Keithley source meter (model 2612A) with the magnetic field of ~0.5 Tesla.

The sample structure used in my study is of size 1 cm × 1 cm. The ohmic contacts were made of Indium by soldering followed by annealing for 15 min at 250 °C. Finally, the electrical properties were measured using Van der Pauw method. The limitation of our setup is that we require only square sample of size ranging from 0.5 cm × 0.5 cm to 1 cm × 1 cm. Other limitations are the measurement limitation of our source meter Keithly 2612A.

2.2.2 I-V and C-V Measurement system

The current-voltage (*I-V*) measurement is an important characterization to characterize the metal contact properties. It is used to identify ohmic and Schottky metal contact on the semiconductor. It is also used to evaluate contact properties like contact resistance in the case of ohmic contact. For Schottky contact, it is used to determine the barrier height, ideality factor, and reverse saturation current. The details of *I-V* characterization is present in later chapters of this thesis.

The capacitance-voltage (*C-V*) measurement method is used to determine the majority carrier concentration in semiconductors. *C-V* measurements are capable of yielding quantitative information about the diffusion potential and doping concentration in semiconductor materials. The technique employs *p-n* junctions, metal-semiconductor (MS) junctions (Schottky barriers), electrolyte-semiconductor junctions, metal-insulator-semiconductor (MIS) capacitors, and MIS field effect transistors (MISFETSs). *C-V* measurements yield accurate information about doping concentrations of majority carriers as a function of distance (depth) from the junction. The detail capacity of the *C-V* characterization is present in [6].

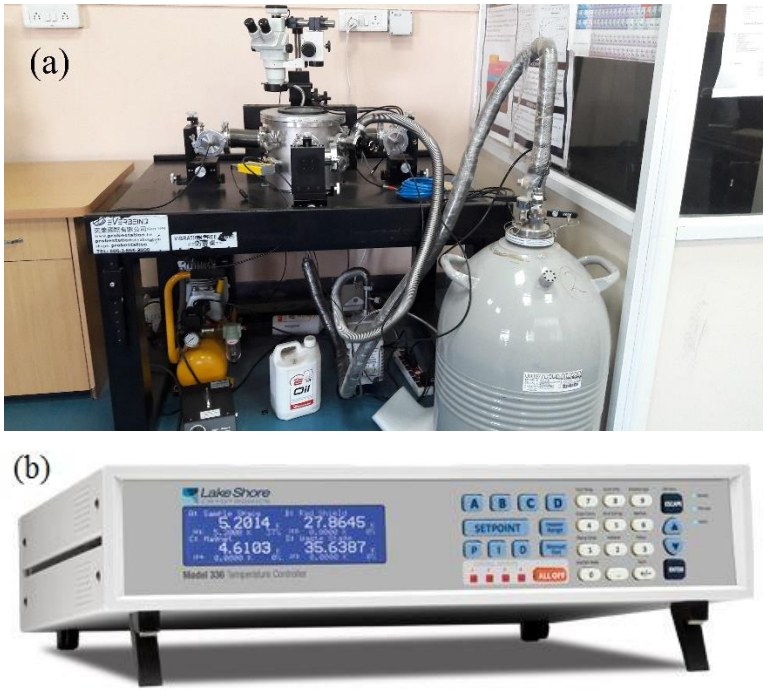

Fig. 2.7: Photographs of (a) probe station and (b) temperature controller.

Fig. 2.7 and Fig. 2.8 shows the photographic images of *I-V* and *C-V* measurement setup. The setup includes Everbeing cryogenic probe station with the temperature range of 80 K to 350 K, source meter Keithley 2612 A, and semiconductor parameter analyzer (4200A SCS).

In this research work, *I-V* measurement is used to measure ideality factor, barrier height, and reverse saturation current of Au Schottky contact on MgZnO. *C-V* measurement is used to characterize the barrier height of Au Schottky contact on MgZnO and depth profiling of MgZnO/ZnO based heterostructures.

(b)

Fig. 2.8: Images of (a) Keithley 2612A and (b) Keithley 4200A semiconductor parameter analyzer.

Our setups are capable to measure the I-V and C-V of different sizes and shapes of thin film samples, but in my case, I have used mainly the square samples and rectangular samples of area not more than 2 cm^2. The limitation of our setup is that we can only measure the I-V and C-V in the temperature range of 77 K to 450 K.

2.2.3 X-Ray Diffraction Measurement

X-Ray diffraction (XRD) is an important technique to examine the crystallinity, phase, strain, and preferred orientation, etc. of samples [7]. A collimated beam of X-Rays is incident on a sample and diffracted by the crystalline phases in the sample according to Bragg's law such that:

$$n\lambda = 2d\ sin\theta \qquad (2.3)$$

Where λ is the wavelength of the incident X-Ray beam, d is the inter-plane separation of lattice between atomic planes in the crystalline phase, θ is the angle between atomic planes and the incident X-Rays beam. Where n is an integer that represents the interference order.

The intensity of the diffracted X-Rays is measured as a function of the diffraction angle 2θ. This diffraction pattern is used to identify the sample crystal orientation [7]. It is well known that atoms of a pure solid are arranged in a regular periodic pattern called 'lattice.' The inter-atomic distance and interaction of atoms in any crystalline lattice is unique and results in a unique XRD pattern to identify its crystal structure. The XRD

patterns include peak position and intensity of the diffracted beam, which provides a variety of information about the samples.

In this research work, the crystal structure of MgZnO and ZnO based thin films were characterized using Rigaku SmartLab, Automated Multipurpose X-Ray Diffractometer equipped with a copper target (Cu-Kα) to generate the incident X-Rays of wavelength λ = 0.154178 nm for the diffraction measurement in Bragg Brentano configuration. The actual image of this XRD system is shown in Fig. 2.9.

Fig. 2.9: Photograph of Rigaku SmartLab, Automated Multipurpose X-Ray Diffractometer.

The sample structure used in my study for XRD measurement were mainly square samples of size less than 2 cm^2.

2.2.4 Energy-dispersive X-Ray spectroscopy

Energy Dispersive X-Ray Spectroscopy (EDS or EDX) is a chemical microanalysis technique used in conjunction with scanning electron microscopy (SEM). The EDX technique detects X-Rays emitted from the sample during the bombardment by an electron beam to characterize the elemental composition of the analyzed volume. Features or phases as small as 1 μm or less can be analyzed [8].

When the sample is bombarded by the SEM's electron beam, electrons are ejected from the atoms comprising the sample's surface. The resulting electron vacancies are filled by electrons from a higher state, and an X-Ray is emitted to balance the energy difference between the two electrons' states. The X-Ray energy is characteristic of the element from which it was emitted.

The EDX X-Ray detector measures the relative abundance of emitted X-Rays versus their energy. The detector is typically lithium-drifted silicon, solid-state device. When an incident X-Ray strikes the detector, it creates a charge pulse that is proportional to the energy of the X-Ray. The charge pulse is converted to a voltage pulse (which remains proportional to the X-Ray energy) by a charge-sensitive preamplifier. The signal is then sent to a multichannel analyzer where the pulses are sorted by voltage. The energy, as determined by the voltage measurement, for each incident X-Ray is sent to a computer for display and further data evaluation. The spectrum of X-Ray energy versus counts is evaluated to determine the elemental composition of the sampled volume. Quantitative results can be obtained from the relative X-Ray counts at the characteristic energy levels for the sample constituents [8].

In this research work, the composition of different elements in MgZnO was characterized using energy dispersive X-Ray (EDX, Zeiss Supra 55). The actual image of this EDX system is shown in Fig. 2.10.

Fig. 2.10: Photograph of EDX, Zeiss Supra 55.

2.2.5 Variable Angle Variable Wavelength Spectroscopic Ellipsometry Measurement System

Ellipsometry technique measures a change in polarization as light reflects or transmits from a material structure [9], [10]. The polarization change is represented as an amplitude ratio, Ψ, and the phase difference, Δ. The measured response depends on optical properties and thickness of individual materials. Thus, ellipsometry is primarily used to determine film thickness and optical constants. However, it is also applied to characterize composition, crystallinity, roughness, doping concentration, and other material properties associated with a change in optical response [9], [10].

The incident light is linear with both *p*- and *s*- components. The reflected light from the sample has undergone amplitude and phase changes for both *p*- and *s*- polarized light, and ellipsometry measures their changes. The change in polarization is the ellipsometry measurement, commonly written as:

$$\rho = \frac{r_p}{r_s} = \tan\psi\, e^{i\Delta} \tag{2.4}$$

Where r_p and r_s are the amplitude reflection coefficients for the *p*- and *s*-polarized light, respectively, tan(Ψ) is the ratio of the amplitude reflection coefficients, and Δ is the phase difference between *s*- and *p*-polarized light.

The primary components of the ellipsometry system are a light source, polarization generator, sample, polarization analyzer, and detector [9]. The polarization generator and analyzer are constructed of optical components that manipulate the polarization: polarizers, compensators, and phase modulators. In this research work, the thickness of thin films was measured by M-2000D J. A. Woollam Variable Angle Variable Wavelength Spectroscopic Ellipsometer. In this system, the measurement can be performed at different angles for the wavelength range of 200-1000 nm. The photographic image of Variable Angle Variable Wavelength Spectroscopic Ellipsometer is shown in Fig. 2.11.

Fig. 2.11: Photographic image of Variable Angle Variable Wavelength Spectroscopic Ellipsometry system.

In my case I have used spectroscopic ellipsometry measurement to determine the thickness of samples only.

2.2.6 High-Resolution Transmission Electron Microscopy

To understand the operating principle of high-resolution transmission electron microscopy (HRTEM), one needs to first understand the operating principle of transmission electron microscopy (TEM). TEM is a technique

that uses the interaction of energetic electrons with the sample and provides morphological, compositional and crystallographic information. The electron emitted from filament passes through the multiple electromagnetic lenses and makes contact with the screen where the electrons are converted into light, and an image is obtained. The speed of electrons is directly related with the electron wavelength and determines the image resolution. A modern TEM is composed of an illumination system, a condenser lens system, an objective lens system, a magnification system, and the data recording system. A set of condenser lens that focuses the beam on the sample and an objective lens collects all the electrons after interacting with the sample and form image of the sample and determines the limit of image resolution. Finally, a set of intermediate lenses that magnify this image and projects them on a phosphorous screen or a charge coupled device (CCD). TEM can be used for imaging and diffraction mode [11].

The high-resolution transmission electron microscopy (HRTEM) uses both the transmitted and the scattered beams to create an interference image. It is a phase contrast image and can be as small as the unit cell of the crystal. In this case, the outgoing modulated electron waves at very low angles interfere with itself during propagation through the objective lens. All electrons emerging from the specimen are combined at a point in the image plane. HRTEM has been extensively and successfully used for analyzing crystal structures and lattice imperfections in various kinds of advanced materials on an atomic resolution scale. It can be used for the characterization of point defects, stacking faults, dislocations, precipitates grain boundaries, and surface structures [11].

In this research work, the quality of MgZnO/ZnO interface was studied using HRTEM. The photographic image of HRTEM is shown in Fig. 2.12.

Fig. 2.12: Photographic image representation of HRTEM.

2.3 References

[1] S. Kumar Pandey, S. Kumar Pandey, V. Awasthi, A. Kumar, U. P. Deshpande, M. Gupta, and S. Mukherjee, "p-type conduction from Sb-doped ZnO thin films grown by dual ion beam sputtering in the absence of oxygen ambient," *J. Appl. Phys.*, vol. 114, no. 16, p. 163107, Oct. 2013.

[2] F. Quaranta, A. Valentini, F. R. Rizzi, and G. Casamassima, "Dual-ion-beam sputter deposition of ZnO films," *J. Appl. Phys.*, vol. 74, no. 1, pp. 244–248, Jul. 1993.

[3] H. R. Kaufman, R. S. Robinson, and R. I. Seddon, "End-Hall ion source," *J. Vac. Sci. Technol. A Vacuum, Surfaces, Film.*, vol. 5, no. 4, pp. 2081–2084, Jul. 1987.

[4] O. Bierwagen, T. Ive, C. G. Van de Walle, and J. S. Speck, "Causes of incorrect carrier-type identification in van der Pauw–Hall measurements," *Appl. Phys. Lett.*, vol. 93, no. 24, p. 242108, Dec. 2008.

[5] A. A. Ramadan, R. D. Gould, and A. Ashour, "On the Van der Pauw

method of resistivity measurements," *Thin Solid Films*, vol. 239, no. 2, pp. 272–275, Mar. 1994.

[6] P. A. Barnes, "Capacitance-Voltage (C-V) Characterization of Semiconductors," in *Characterization of Materials*, Hoboken, NJ, USA: John Wiley & Sons, Inc., 2012.

[7] H. Kim, C. M. Gilmore, A. Piqué, J. S. Horwitz, H. Mattoussi, H. Murata, Z. H. Kafafi, and D. B. Chrisey, "Electrical, optical, and structural properties of indium–tin–oxide thin films for organic light-emitting devices," *J. Appl. Phys.*, vol. 86, no. 11, pp. 6451–6461, Dec. 1999.

[8] S. T. D. Ellingham, T. J. U. Thompson, and M. Islam, "Scanning Electron Microscopy-Energy-Dispersive X-Ray (SEM/EDX): A Rapid Diagnostic Tool to Aid the Identification of Burnt Bone and Contested Cremains," *J. Forensic Sci.*, vol. 63, no. 2, pp. 504–510, Mar. 2018.

[9] L. Arsov, M. Ramasubramanian, and B. N. Popov, "Ellipsometry," in *Characterization of Materials*, Hoboken, NJ, USA: John Wiley & Sons, Inc., 2012, pp. 1–11.

[10] P. Sharma, Aaryashree, V. Garg, and S. Mukherjee, "Optoelectronic properties of phosphorus doped p-type ZnO films grown by dual ion beam sputtering," *J. Appl. Phys.*, vol. 121, no. 22, p. 225306, Jun. 2017.

[11] J. M. Howe, B. Fultz, and S. Miao, "Transmission Electron Microscopy," in *Characterization of Materials*, Hoboken, NJ, USA: John Wiley & Sons, Inc., 2012, pp. 1–46.

Chapter 3

Analytical Modelling for Estimation of 2DEG Density in MgZnO/ZnO Heterostructures

3.1 Introduction

Zinc oxide (ZnO) material and its heterostructures have emerged as promising materials for thin film transistors, solar cells, bio-compatible devices, ultra-violet (UV) light-emitting diodes and lasers [1]–[4]. A two-dimensional electron gas (2DEG) is formed in MgZnO/ZnO heterostructure, similar to that in AlGaN/GaN, due to strong spontaneous and piezoelectric polarization effects [5]. MgZnO/ZnO heterostructure has several advantages over the AlGaN/GaN material system including a higher saturation velocity, a lower lattice mismatch, and the capability for bulk growth [6]–[9]. Usually, a higher 2DEG is obtained by increasing Mg composition (x) which lies within the range $0.05 < x < 0.6$ in the barrier layer. Since MgO is found stable as rocksalt structure in nature, for higher Mg composition ($x > 0.62$) phase separation is reported [10]. Also, for higher values of Mg composition, 2DEG density increases but two-dimensional electron mobility (2DEM) reduces due to optical phonon scattering [11]. In order to enhance 2DEM, a cap layer of ZnO can be added similar to GaN in the case of AlGaN/GaN which increases 2DEM [11], [12].

The dominant polarization in ZnO based heterostructures governing the 2DEG formation requires careful analysis for improved performance. Models for n_s (2DEG density), yet known, are primarily based on numerical calculations, semi-empirical model expressions, or simplifying approximations [13]–[15]. There exist few physics-based models in the literature [16]–[19], for calculation of 2DEG density, but they consider mainly the simple bilayer (barrier layer and buffer layer) structure consisting of buffer and barrier layers or are developed for either AlGaAs/GaAs or AlGaN/GaN system. For the MgZnO/ZnO system, very

few analytical models for the estimation of 2DEG density are reported [20]. Analytical models incorporating the effect of the cap layer on the variation of 2DEG density are also not available.

In this chapter, we develop a physics-based analytical model for the calculation of 2DEG density in a graded MgZnO/ZnO heterostructure with a cap layer. Graded heterostructures with different doping concentration in the barrier layer, find use in high gain [21] and high breakdown [22] devices. A graded MgZnO/ZnO heterostructure in this chapter is considered as a structure in which layers of MgZnO with different Mg compositions are deposited over ZnO buffer layer. A graded MgZnO structure with a modulation doping layer which resulted in higher 2DEG values has been utilized by Huang *et al.*, [23] and Cohen *et al.*, [24] for the design of transparent electronics and modulation-doped field-effect transistors. The generic model developed in this chapter can be reduced to a relatively simple bilayer structure of barrier layer on top of ZnO (buffer) layer. The proposed model includes the strongly dominant effect of total polarization charge (spontaneous and piezoelectric) in estimating 2DEG density. The influence of technology parameters such as MgZnO layer thickness and Mg composition (x) on 2DEG density is also analyzed. The developed model is a useful tool for the design and optimization of 2DEG and threshold voltage (V_{OFF}) in ZnO based heterostructures.

3.2 2DEG Density Model Development

We present a model for the calculation of 2DEG density (n_s) in a generalized heterostructure (structure I), (Fig. 3.1 (a)) which can be simplified for the other three structures. The structures I and III have a cap layer of ZnO, while structures II and IV are without a cap layer as shown in Fig. 3.1 (a). The graded structure is analyzed by considering different mole fractions (x and y) of Mg as shown in structure I. For structure I, the Poisson equation has been solved at all interfaces, i.e., at the top ZnO surface, interface III (ZnO/$Mg_yZn_{1-y}O$), interface II ($Mg_yZn_{1-y}O$/Mg_xZn_{1-}

$_x$O), and interface I ($Mg_xZn_{1-x}O$/ZnO). The analysis is further simplified by the

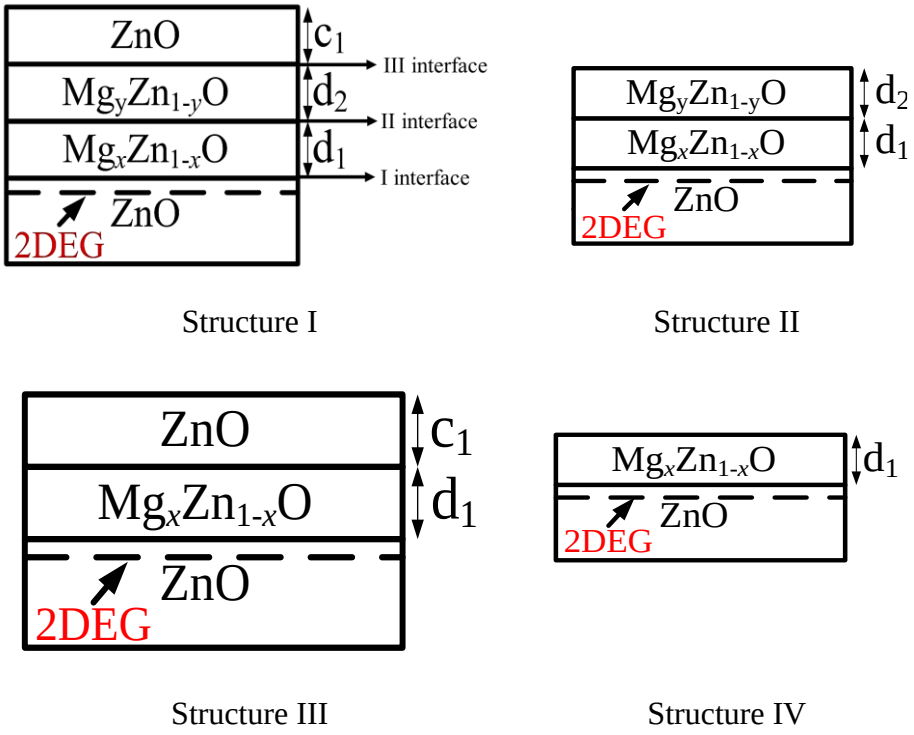

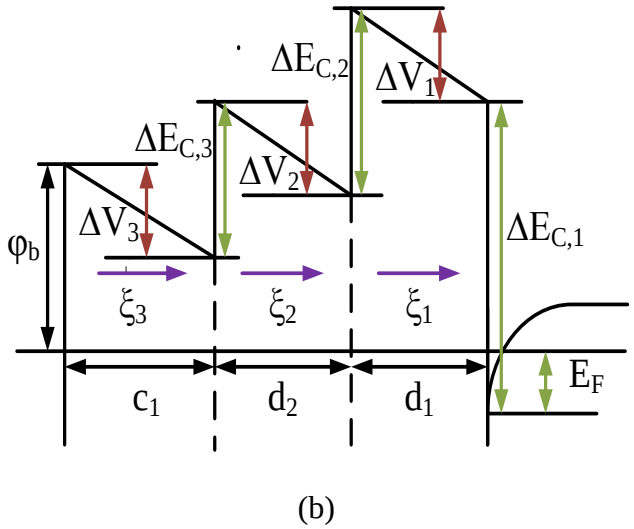

Fig. 3.1: (a) Schematic of structure I, II, III and IV. (b) A generic representation of energy band diagram of structure I showing electric field and conduction band offsets. The exact slope of bands and band offsets will depend on the Mg molar composition in different layers.

assumption of same permittivity ϵ for all layers, since their values are quite close [25].

The energy band diagram of the generalized structure (structure I) is shown in Fig. 3.1 (b). Considering Fig. 3.1 (b), we observe that to maintain dielectric boundary conditions at III and II interfaces, the electric fields ξ_3, ξ_2 and ξ_1 in layer 3 (ZnO cap layer), layer 2 ($Mg_yZn_{1-y}O$), and layer 1 ($Mg_xZn_{1-x}O$), respectively, can be expressed as.

$$\epsilon\xi_3 = \epsilon\xi_2 + q\sigma_{net_3} \tag{3.1}$$

$$\epsilon\xi_2 = \epsilon\xi_1 + q\sigma_{net_2} \tag{3.2}$$

where $\sigma_{net_3}(= \sigma_2\text{-}\sigma_3)$ and $\sigma_{net_2}(= \sigma_1\text{-}\sigma_2)$ are the net polarization sheet charge densities at ZnO/$Mg_yZn_{1-y}O$ and $Mg_yZn_{1-y}O$/$Mg_xZn_{1-x}O$ interfaces, respectively, and σ_3, σ_2, and σ_1 are the polarization charge densities of layer 3, layer 2, and layer 1, respectively and q is the charge of the electron. The polarization charge density of any layer is comprised of two components, namely spontaneous (P_{sp}) and piezoelectric (P_{zp}).

Fig. 3.2 shows the calculated critical thickness of $Mg_xZn_{1-x}O$ for different possible combinations of heterostructures in discussed structures, as a function of Mg composition. The critical thickness (h_c) of different layer combinations in the given four structures is calculated using $h_C = \left(\frac{1}{1+\nu}\right)\left(\frac{1}{4\pi}\right)\left(\frac{b}{f}\right)\left[\ln\left(\frac{h_C}{b}\right) + 1\right]$, where, $\nu = 0.271$ is Poisson's ratio, $b = 6.137$ Å is Burger's vector, and f is the misfit which is expressed as $f = |(a_s - a_0)/a_s|$, a_0 is unstrained lattice constant of the deposited layer and a_s is the lattice constant of the lower layer which is substrate for MgZnO/ZnO heterostructures [26]. It is observed that for $Mg_xZn_{1-x}O$/ZnO heterostructures (curve A), the critical thickness decreases as the Mg molar composition increases. This is due to increase in the misfit with the increase in Mg molar composition. The curve B rises steeply as x approaches x = 0.3 is due to zero misfit for x = 0.3. Similarly, the curve C rises steeply as x approaches 0.6 [26]. Matsui *et al.*, [27] reported that for $Mg_{0.37}ZnO_{0.63}$/ZnO heterostructure, the experimental critical thickness is

approx. 38-65 nm. Analytical value using the discussed equation for critical thickness, for $Mg_{0.37}ZnO_{0.63}$/ZnO heterostructure, is ~ 30 nm. This deviates approx. 10-35 nm from experimental value. Due to the lack of experimental evidences for different Mg compositions, we have assumed all the layers to be fully strained up to 30 nm thickness in all the discussed heterostructures.

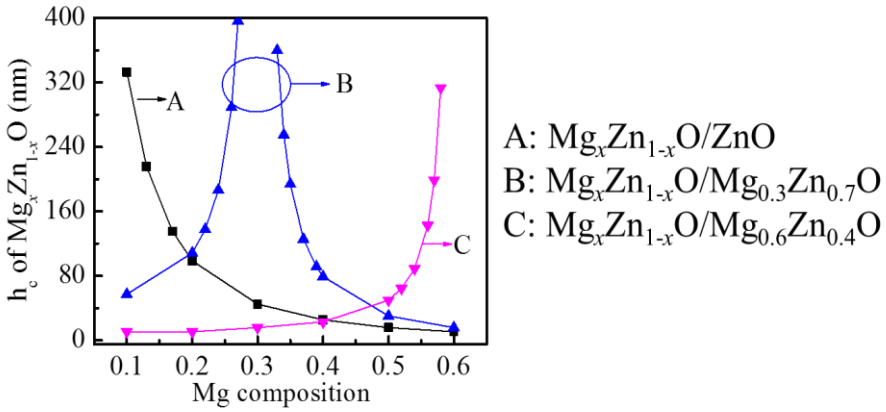

Fig. 3.2: Critical layer thickness of $Mg_xZn_{1-x}O$ for different combinations.

The piezoelectric polarization component in MgZnO layers is given as [18]

$$P_{zp} = 2\left(\frac{a_s - a_0}{a_0}\right)\left(E_{31} - \frac{E_{33}C_{13}}{C_{33}}\right) \tag{3.3}$$

Components for the calculation of composition-dependent piezoelectric polarization, spontaneous polarization, lattice constants, bandgap, relative permittivity, and bare surface barrier height are given in Table 3.1.

In the absence of gate potential at the cap layer c_1, ξ_3 can be deduced from the energy band diagram Fig. 3.1 (b) as

$$\xi_3 = \frac{-\phi_b - E_F - \xi_1 d_1 - \xi_2 d_2 - \Delta E_{C,net}}{c_1} \tag{3.4}$$

where, ϕ_b is the bare surface barrier height (as given in Table 3.1), d_1, d_2, and c_1 are the thicknesses of the barrier layer ($Mg_xZn_{1-x}O$), modulation layer

($Mg_yZn_{1-y}O$), and a cap layer (ZnO), respectively. E_F is the Fermi energy level with respect to the bottom of the conduction band at the $Mg_xZn_{1-x}O$/ZnO interface and $\Delta E_{C,net}(= \Delta E_{C,3} + \Delta E_{C,2} - \Delta E_{C,1})$ is the net conduction band offset, $\Delta E_{C,3}$, $\Delta E_{C,2}$ and $\Delta E_{C,1}$ are conduction band offset at III, II, and I interface, respectively, and are equal to 0.9 times the difference of band gaps of surfaces making that interface [20].

Table 3.1: Parameters of MgZnO calculated from mole fraction (x) at room temperature.

Parameters	Description	$Mg_xZn_{1-x}O$
a	Lattice constant (nm)	$0.3246 + 0.0016x + 0.0109x^2$ [28]
c	Lattice constant (nm)	$0.5206 – 0.0111x$ [29]
C_{13}	Elastic stiffness constant (GPa)	$84 + 4x$ [29]
C_{33}	Elastic stiffness constant (GPa)	$176 - 9x + 55x^2$ [29]
e_{31}	Piezoelectric constant (C/m^2)	$- 0.55 - 0.23x$ [29]
e_{33}	Piezoelectric constant (C/m^2)	$1.24 - 1.10x$ [29]
P_{SP}	Spontaneous polarization (C/m^2)	$- 0.057 - 0.066x$ [30]
E_g	Bandgap (eV)	$3.37 + 2.145x$ [20]
ϵ_A/ϵ_0	Relative permittivity	$8.75 + 1.08x$ [20]
ϕ_b	Barrier height (eV)	$5.81x^2 - 3.12x + 1.12$ [31]

Combining (3.1) and (3.4), we obtain the field (ξ_2) as

$$\xi_2 = \frac{-\phi_b - E_F - \xi_1 d_1 - \Delta E_{C,net} - \frac{q\sigma_{net_3} c_1}{\epsilon}}{c_1 + d_2} \qquad (3.5)$$

From (3.2) and (3.5), we can calculate the field (ξ_1) as

$$\xi_1 = \frac{1}{d_1 + d_2 + c_1}\left(-\phi_b - E_F - \Delta E_{C,net} - \frac{q\sigma_{net_3}c_1}{\epsilon} - \frac{q\sigma_{net_2}(d_2 + c_1)}{\epsilon}\right) \tag{3.6}$$

Furthermore, the thickness of the net charge developed at $Mg_xZn_{1-x}O$ and ZnO (buffer layer) interface is very small compared to the cross-sectional area of the interface [18]. Hence, ξ_1 can also be expressed as

$$\xi_1 = \frac{qn_s - q\sigma_{net_1}}{\epsilon} \tag{3.7}$$

where, σ_{net_1} is 0.029×Mg composition in layer 1 [32] is the net polarization sheet charge density at $Mg_xZn_{1-x}O$/ZnO interface. Expression for n_s obtained by equating (3.6) and (3.7) can be written as

$$n_s = \frac{\epsilon}{qd_T}\left[V_g - \phi_b - \Delta E_{C,net} - E_F + \frac{q}{\epsilon}\sigma_{net_1}(d_2 + d_1 + c_1) - \frac{q}{\epsilon}\left(\sigma_{net_3}c_1 + \sigma_{net_2}(d_2 + c_1)\right)\right] \tag{3.8}$$

Equation (3.8) can be reduced to a more compact expression as

$$n_s = \frac{\epsilon}{qd_T}\left[V_g - V_{OFF} - E_F\right] \tag{3.9}$$

where d_T *(=* d_1+d_2+c_1*)* is the total thickness of layers over the buffer layer (bottom ZnO layer) and V_g is the applied gate voltage. V_{OFF} is the threshold voltage and is given as

$$V_{OFF} = \phi_b + \Delta E_{C,net} + \frac{q}{\epsilon}\left(\sigma_{net_3}c_1 + \sigma_{net_2}(d_2 + c_1) - \sigma_{net_1}(d_1 + d_2 + c_1)\right) \tag{3.10}$$

The variation of E_F with n_s in the triangular potential well can be expressed as [16]

$$n_s = DV_t \left\{ \ln\left[exp\left(\frac{E_F - E_0}{V_t}\right) + 1 \right] + \ln\left[exp\left(\frac{E_F - E_1}{V_t}\right) + 1 \right] \right\} \quad (3.11)$$

where $D = 1.1 \times 10^{18}\ m^{-2}V^{-1}$ is the two dimensional density of states [16] and $V_t = kT/q$ is the thermal voltage where k is Boltzmann's constant, T is absolute temperature and , q is the charge of the electron. E_0 and E_1 are the position of first and second sub-bands, respectively, in triangular potential well.

The occupancy in second sub-band of 2DEG in the triangular potential well is not considered because the energy level of E_1 is higher than E_F [19] for nearly all practical operating voltages as shown in Fig. 3.3 (a) and Fig. 3.3 (b), for all structures. The value of E_F, E_0, and E_1 for all structures are calculated by a numerical technique based on (3.9) and (3.11). Ignoring the occupancy in the second sub-band of the 2DEG in a triangular potential well, n_s is expressed in terms of E_F as

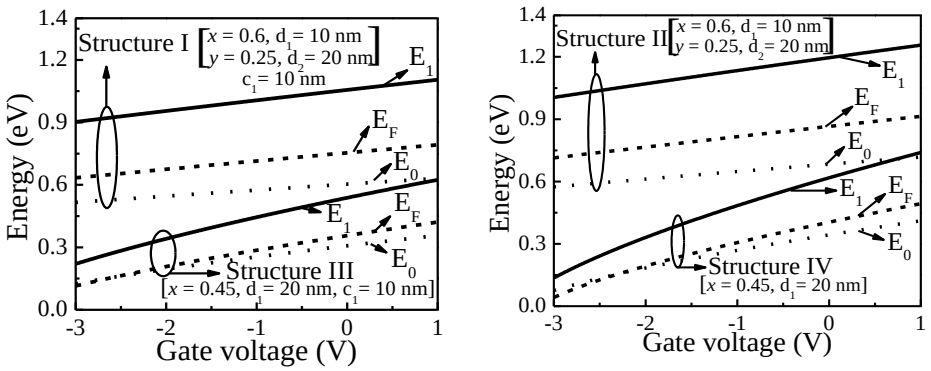

(a) (b)

Fig. 3.3: Values of Fermi energy and the first two sub-band energy levels in the triangular potential well for (a) Structures I and III, and (b) Structures II and IV.

$$n_s = DV_t \ln\left[exp\left(\frac{E_F - E_0}{V_t}\right) + 1 \right] \quad (3.12)$$

where $E_0=\gamma_0(n_s)^{2/3}$, and $\gamma_0=2 \times 10^{-12}\text{V}\cdot\text{m}^{4/3}$ is a parameter which is determined experimentally [16]. Equation (3.9) and (3.12) when solved

simultaneously gives an expression of n_s independent of E_F [19]

$$n_s = \frac{C_g V_{g0}}{q} \frac{V_{g0} + V_t\left[1 - \ln(\beta V_{gon})\right] - \frac{\gamma_0}{3}\left(\frac{C_g V_{g0}}{q}\right)^{2/3}}{V_{g0}\left(1 + \frac{V_t}{V_{god}}\right) + \frac{2\gamma_0}{3}\left(\frac{C_g V_{g0}}{q}\right)^{2/3}} \tag{3.13}$$

where $C_g = \epsilon/(d_1 + d_2 + c_1)$, $\beta = C_g/(qDV_t)$, $V_{g0} = V_g - V_{\mathrm{OFF}}$, and V_{gon} and V_{god} are functions of V_{go} given by the interpolation expression [19]

$$V_{g0x} = V_{g0}\alpha_x / \sqrt{V_{g0}^2 + \alpha_x^2} \tag{3.14}$$

where $\alpha_n = e/\beta$, and $\alpha_d = 1/\beta$. The above-discussed derivation process is generic and can be reduced for the remaining three structures (shown in Fig. 3.1 (a)) by substituting that layer's thickness and interface band offset as zero which is not a part of the structure. The parameters, which are affected, are C_g, β, and V_{OFF}. The expression of V_{OFF} for structure II, structure III, and structure IV are listed in Table 3.2.

Table 3.2 Expression of V_{OFF} for structure II, structure III, and structure IV.

Structure	Expression of V_{OFF}
II	$V_{OFF} = \phi_b + \Delta E_{C,2} - \Delta E_{C,1} + \frac{q}{\epsilon}\left(\sigma_{net_2} d_2 - \sigma_{net_1}(d_1 + d_2)\right)$
III	$V_{OFF} = \phi_b + \Delta E_{C,2} - \Delta E_{C,1} + \frac{q}{\epsilon}\left(\sigma_{net_2} c_1 - \sigma_{net_1}(d_1 + c_1)\right)$
IV	$V_{OFF} = \phi_b - \Delta E_{C,1} - \frac{q}{\epsilon}\sigma_{net_1} d_1$

3.3 Results and Discussion

2DEG density (n_s) and threshold voltage (V_{OFF}) in four different heterostructures as shown in Fig. 3.1 (a) are investigated for the effects of variation in layers' thickness and Mg composition. Each layer thickness and Mg composition is varied independently while maintaining other

layers' parameters constant. Fig. 3.4 (a) compares the n_s in structure I and structure II varying the thickness (d_2) of modulation layer with different Mg compositions (y) while keeping barrier layer parameters like Mg composition (x = 0.6) and thickness (d_1 = 10 nm) constant. Fig. 3.4 (a) shows 2DEG density increasing almost linearly for lower d_2 for all Mg compositions, and saturating for higher d_2 values. The reason for this observation in structure II is the existence of surface donor-like states. In the literature, these states are widely accepted to be the source of the 2DEG electrons [32]–[35]. Assuming these donor-like surface states are located quite deep in the $Mg_yZn_{1-y}O$ band gap, they will all be occupied with small values of d_2. As the thickness of the modulation layer increases, the Fermi energy level at the surface approaches the deep donor level. As the thickness of the modulation layer is increased further, 2DEG density will tend to saturate as the Fermi energy level gets pinned by the surface states. Therefore, variation in layer thickness modulates the effective two-dimensional density of states (D) participating in the formation of 2DEG.

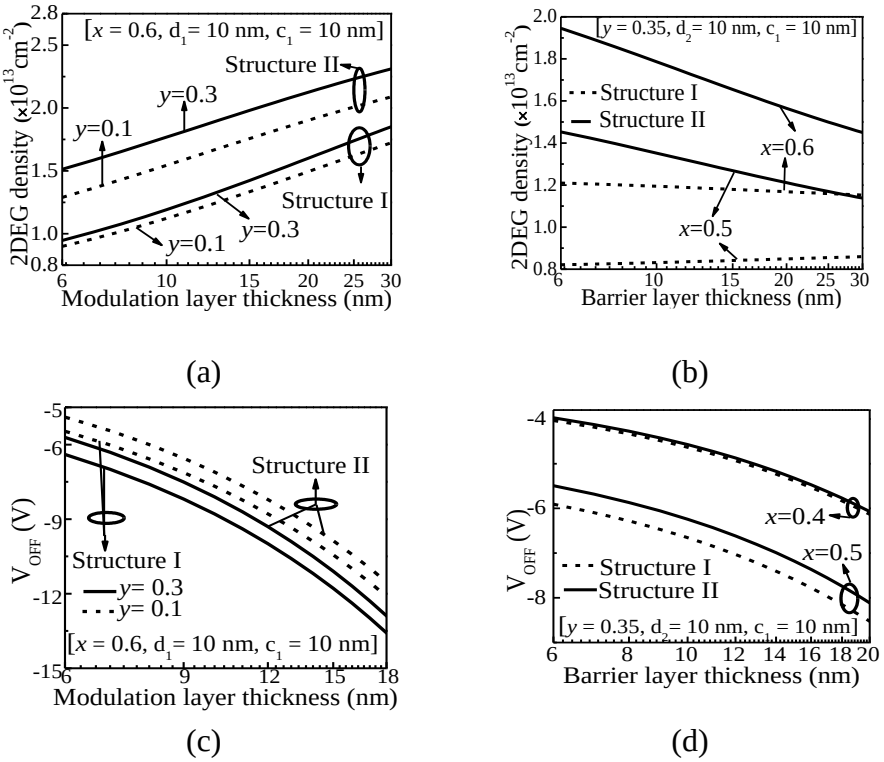

Fig. 3.4: Variation of 2DEG density with (a) Modulation layer thickness (d_2), and (b) Barrier layer thickness (d_1). Dependence of threshold voltage on (c) Modulation layer thickness (d_2), and (d) Barrier layer thickness (d_1).

Furthermore, it is also observed that, with higher Mg composition in the modulation layer, greater n_s is exhibited for both structures I and II. This increase in n_s with increasing Mg composition can be attributed to the enhanced degree of polarization [36]. It is also observed in Fig. 3.4 (a) that 2DEG density in capped structure (structure I) is lower than 2DEG density in the structure without a cap layer (structure II). A reduced n_s in structure I then structure II is a consequence of the fact that the ZnO cap layer introduces a negative polarization charge at the cap-modulation interface which introduces a two-dimensional hole gas (2DHG) at the cap-modulation interface. This 2DHG absorbs some of the electron coming from the surface donor states to neutralize the top surface of the heterostructure causing the n_s to decrease [34]. This effect is captured as the by σ_{net_3} whose value becomes negative as the net polarization charge in the modulation layer is greater than the cap layer.

Fig. 3.4 (b) shows the variation of 2DEG as a function of the barrier layer thickness (d_1) of structure I and structure II for different Mg compositions (x) of the barrier layer, keeping modulation layer Mg composition and thickness constant at 0.35 and 10 nm, respectively. In these cases, n_s decreases initially and then saturate. Here, structure II can be treated as a special case of bilayer $Mg_xZn_{1-x}O$/ZnO heterostructure with cap layer having higher net polarization due to 0.35 Mg composition. This higher net polarization of the modulation layer forms a 2DEG at the modulation-barrier interface which gives a positive value of σ_{net_2} in the model. The decrease in n_s with increasing barrier layer thickness can again be attributed to surface donor states which are present at the top surface of modulation layer. Initially, the donor states in this specific case are all depleted since the thickness of modulation layer is 10 nm which is the critical thickness to deplete all the donor states present at the top surface of modulation layer for 0.35 Mg composition [32]. Therefore, the 2DEG density is high for lower barrier layer thickness. When the barrier layer thickness increases, E_F decreases and then saturates.

Fig. 3.4 (c) and Fig. 3.4 (d) shows the variation of threshold voltage V_{OFF}, which is defined as the voltage, which is required to be applied on the gate terminal to fully deplete the 2DEG, of structure I and II with modulation and barrier layers, respectively. The threshold voltage of structure I is higher in magnitude in comparison to structure II. This is because, in addition to depleting 2DEG density, a barrier layer, and modulation layer, an additional potential is required to deplete cap layer in structure I.

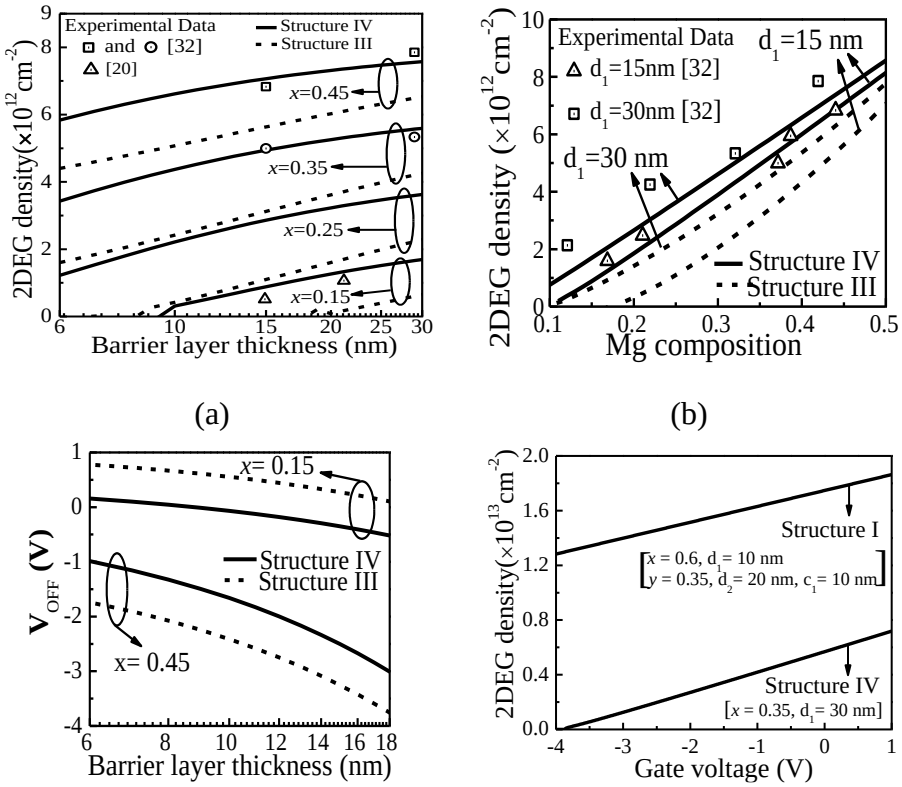

Fig. 3.5: Variation of 2DEG density with (a) Barrier layer thickness (d_1), and (b) Mg composition (x) (c) Dependence of threshold voltage on barrier layer thickness (d_1). The thickness of the cap layer (c_1) is 10 nm (d) Dependency of 2DEG density on the gate voltage. The experimental data in (a) & (b) is only for structure IV.

Effect of barrier layer thickness (d_1) and Mg composition (x) on 2DEG density of bilayer structure, without (structure IV) and with a 10 nm cap layer (structure III), is shown in Fig. 3.5 (a). The 2DEG density is seen to increase linearly for lower barrier layer thickness and saturates for higher barrier layer thickness. This can also be explained by the existence of the surface donor-like states, as discussed for structure II for Fig. 3.4 (a). A similar trend is also obtained by Tampo *et al.* [32] for MgZnO/ZnO heterostructure. This behavior is also as reported by Ibbetson *et al.* [35] for AlGaN/GaN heterostructure. Also, the 2DEG density of the capped structure III is lower than structure IV, the reason for which is similar to the discussion for the structure I in Fig. 3.4 (a).

Effect of variation of Mg composition (x) of the barrier layer on n_s is evaluated in Fig. 3.5 (b) for the barrier layer thickness of 15 nm, and 30 nm. The value of 2DEG density increases almost linearly with Mg composition and has a small dependence on the barrier layer thickness. This is because with the increase of Mg composition in barrier layer the net polarization sheet charge density at barrier/buffer interface increases monotonically i.e. σ_{net_1} increases. A similar trend is also observed in O-polar or Zn-polar $Zn_{1-x}Mg_xO/ZnO$ structures grown by MBE [30], [32]. The calculated n_s from the simplified model of the discussed generic model, for structure IV, is in good agreement with the experimental data reported in the literature [20], [32] as can be seen in Fig. 3.5 (a) and Fig. 3.5 (b). The V_{OFF} of capped structure (structure III) is higher in magnitude than structure IV, as shown in Fig. 3.5 (c). The higher magnitude of V_{OFF} for higher Mg composition in layers can be attributed to the additional potential required to deplete the increased 2DEG density.

Fig. 3.5 (d) shows the variation of 2DEG density as a function of gate voltage (V_g) for structure I and structure IV. It is observed that for both the structures, 2DEG density increases with gate voltage because the increase in gate voltage increases E_F, thereby increasing 2DEG density [18].

It should be noted that our model fits experimentally obtained data beyond 10 nm barrier layer thickness with good approximation, but deviates far from experimental data for below 10 nm. This is due to the fact that the net polarization sheet charge density difference at the barrier-buffer interface has been kept constant at $0.029x$ as was obtained experimentally by Tampo *et al*. [32]. However, a lower theoretical value $0.024x$ (obtained by standard first-principles approximation) [37] fits experimental data below 10 nm but deviates for higher thickness values as can be seen in Fig. 3.6. This anomaly can be attributed to the high strain for the very small thickness of barrier layer which makes piezoelectric polarization dominant and since polarization directions of spontaneous and piezoelectric components are opposite in MgZnO [20], they tend to decrease the net polarization in the barrier layer. In this work, $\sigma(x) = 0.029x - (q/d_1^2)x$ is proposed as the

net polarization sheet charge density difference at the barrier-buffer interface which fits the experimentally obtained data beyond 5 nm barrier layer thickness with good approximation.

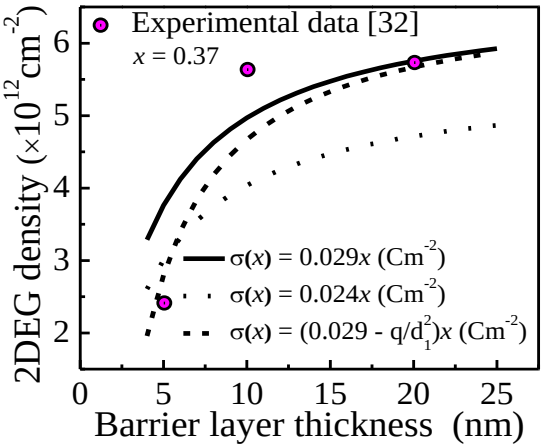

Fig. 3.6: 2DEG density with varying barrier layer thickness of structure IV, for theoretical and experimental value of total polarization in the barrier layer.

A comparative analysis of bilayer (structure IV) and graded (structure II) heterostructures, both without a cap layer, is presented in Fig. 3.7 (a) and (b). The thickness of modulation layer (d_2), with different Mg compositions (y), of structure II is varied while keeping barrier layer thickness (10 nm) and Mg composition (0.6) constant. In structure IV, barrier layer thickness (d_1) is varied, with different Mg compositions (x). In both structures, n_s increases with increasing Mg composition of barrier and modulation layers. Also, n_s obtained in graded structure for 20 nm modulation layer thickness, 10 nm barrier layer thickness and y = 0.45, x = 0.6 is (nearly 2.3 times higher) 2.1×10^{13} cm^{-2} as against to 9.2×10^{12} cm^{-2} in the bilayer structure with barrier layer thickness as 20 nm and Mg composition as 0.6, as shown in Fig. 3.7 (a). The enhanced n_s comes at the expense of more negative V_{OFF} which is -14.1 V, at same observation point as for n_s, against -4.3 V for bilayer structure, as shown in Fig. 3.7 (b).

A less negative V_{OFF} value is desirable because if V_{OFF} is more negative, higher negative voltage will be required to deplete the 2DEG and turn OFF the device, which is not suitable in the low power high-frequency circuits. The general values of V_{OFF} published in the literature for the conventional bilayer AlGaN/GaN HEMT is in the range of -8 V to -4 V [38]. To attain a compromise between a high 2DEG density and less negative V_{OFF} voltage, a graded heterostructure without cap layer and thickness of each layer being in the range of 10 nm to 15 nm is suggested. This is based on the study of structure II, with barrier layer thickness as 10 nm and Mg composition in the barrier and modulation layers as 0.6 and 0.45, respectively, as the thickness of modulation layer is varied from 10 nm to 30 nm. The 2DEG density and V_{OFF} changes from 1.8×10^{13} cm^{-2} to 2.3×10^{13} cm^{-2} (~1.3 times) and -8.1 V to -20 V (~2.5 times), respectively, in 10 nm to 30 nm range (not shown in the graph). While in 10 nm to 20 nm range the 2DEG density increases from 1.8×10^{13} cm^{-2} to 2.1×10^{13} cm^{-2} (~1.2 times) but V_{OFF} changes from -8.1 V to -14.1 V (~1.7 times). Therefore, for lower thickness region, V_{OFF} remains low in magnitude without much change in the 2DEG density. An addition of a 10 nm cap layer will demand an additional 0.7 V V_{OFF} with a reduction of ~30% 2DEG. Thus, a thinner (< 10 nm) cap layer may be employed. The proposed model can be used to analyze various structures, structure optimization, and performance prediction.

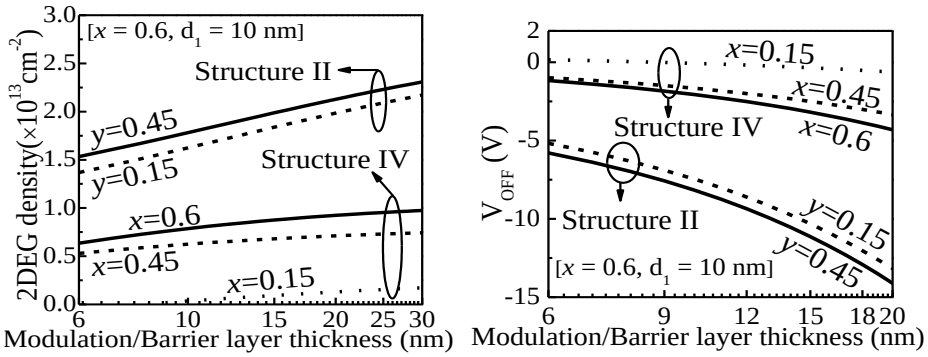

Fig. 3.7: Comparison of structure II and structure IV in terms of 2DEG density and threshold voltage. (a) 2DEG density at different values of modulation/barrier layer thickness, and (b) Threshold voltage at different values of modulation/barrier layer thickness.

3.4 Conclusion

A physics-based analytical model for generic graded MgZnO/ZnO heterostructure with cap layer is developed for the calculation of 2DEG density and V_{OFF}. The generic model can be easily reduced for relatively simpler structures. Calculated n_s values suggest the use of graded MgZnO layer significantly increases (2.3 times higher) the sheet carrier concentration in MgZnO/ZnO heterostructure but at the expense of an increased threshold voltage. A graded structure with a low thickness of layers is proposed, to achieve a compromise between high 2DEG density and V_{OFF}, based on the developed model. An alternate expression for net polarization sheet charge density difference at barrier-buffer interface to overcome the existing discrepancy with experimental data has also been suggested. The proposed model will be a useful tool for the design and optimization of 2DEG and V_{OFF} in ZnO based heterostructures.

3.5 References

[1] K. Ramanathan, M. A. Contreras, C. L. Perkins, S. Asher, F. S. Hasoon, J. Keane, D. Young, M. Romero, W. Metzger, R. Noufi, J.

Ward, and A. Duda, “Properties of 19.2% efficiency ZnO/CdS/CuInGaSe2 thin-film solar cells,” *Prog. Photovoltaics Res. Appl.*, vol. 11, no. 4, pp. 225–230, Jun. 2003.

[2] F. M. Hossain, J. Nishii, S. Takagi, A. Ohtomo, T. Fukumura, H. Fujioka, H. Ohno, H. Koinuma, and M. Kawasaki, “Modeling and simulation of polycrystalline ZnO thin-film transistors,” *J. Appl. Phys.*, vol. 94, no. 12, p. 7768, Aug. 2003.

[3] D. M. Bagnall, Y. F. Chen, Z. Zhu, T. Yao, S. Koyama, M. Y. Shen, and T. Goto, “Optically pumped lasing of ZnO at room temperature,” *Appl. Phys. Lett.*, vol. 70, no. 17, pp. 2230–2232, Apr. 1997.

[4] Y.-S. Choi, J.-W. Kang, D.-K. Hwang, and S.-J. Park, “Recent Advances in ZnO-Based Light-Emitting Diodes,” *IEEE Trans. Electron Devices*, vol. 57, no. 1, pp. 26–41, Jan. 2010.

[5] O. Ambacher, J. Smart, J. R. Shealy, N. G. Weimann, K. Chu, M. Murphy, W. J. Schaff, L. F. Eastman, R. Dimitrov, L. Wittmer, M. Stutzmann, W. Rieger, and J. Hilsenbeck, “Two-dimensional electron gases induced by spontaneous and piezoelectric polarization charges in N- and Ga-face AlGaN/GaN heterostructures,” *J. Appl. Phys.*, vol. 85, no. 6, pp. 3222–3233, Mar. 1999.

[6] J. D. Albrecht, P. P. Ruden, S. Limpijumnong, W. R. L. Lambrecht, and K. F. Brennan, “High field electron transport properties of bulk ZnO,” *J. Appl. Phys.*, vol. 86, no. 12, pp. 6864–6867, Dec. 1999.

[7] A. Ohtomo, M. Kawasaki, T. Koida, K. Masubuchi, H. Koinuma, Y. Sakurai, Y. Yoshida, T. Yasuda, and Y. Segawa, “MgxZn1−xO as a II–VI widegap semiconductor alloy,” *Appl. Phys. Lett.*, vol. 72, no. 19, pp. 2466–2468, May 1998.

[8] A. Ohtomo, M. Kawasaki, I. Ohkubo, H. Koinuma, T. Yasuda, and Y. Segawa, “Structure and optical properties of ZnO/Mg0.2Zn0.8O

superlattices," *Appl. Phys. Lett.*, vol. 75, no. 7, pp. 980–982, Aug. 1999.

[9] A. N. Westmeyer, S. Mahajan, K. K. Bajaj, J. Y. Lin, H. X. Jiang, D. D. Koleske, and R. T. Senger, "Determination of energy-band offsets between GaN and AlN using excitonic luminescence transition in AlGaN alloys," *J. Appl. Phys.*, vol. 99, no. 1, p. 13705, Jan. 2006.

[10] W. Yang, S. S. Hullavarad, B. Nagaraj, I. Takeuchi, R. P. Sharma, T. Venkatesan, R. D. Vispute, and H. Shen, "Compositionally-tuned epitaxial cubic MgxZn1−xO on Si(100) for deep ultraviolet photodetectors," *Appl. Phys. Lett.*, vol. 82, no. 20, pp. 3424–3426, May 2003.

[11] A. Asgari, M. Kalafi, and L. Faraone, "The effects of GaN capping layer thickness on two-dimensional electron mobility in GaN/AlGaN/GaN heterostructures," *Phys. E Low-dimensional Syst. Nanostructures*, vol. 25, no. 4, pp. 431–437, Jan. 2005.

[12] K. Jeganathan, T. Ide, M. Shimizu, and H. Okumura, "Two-dimensional electron gases induced by polarization charges in AlN/GaN heterostructure grown by plasma-assisted molecular-beam epitaxy," *J. Appl. Phys.*, vol. 94, no. 5, pp. 3260–3263, Sep. 2003.

[13] X. Cheng, M. Li, and Y. Wang, "Physics-based compact model for AlGaN/GaN MODFETs with close-formed I-V and C-V characteristics," *IEEE Trans. Electron Devices*, vol. 56, no. 12, pp. 2881–2887, Dec. 2009.

[14] X. Cheng and Y. Wang, "A Surface-Potential-Based Compact Model for AlGaN/GaN MODFETs," *IEEE Trans. Electron Devices*, vol. 58, no. 2, pp. 448–454, Feb. 2011.

[15] N. Goyal and T. A. Fjeldly, "Analytical modeling of

AlGaN/AlN/GaN heterostructures including effects of distributed surface donor states," *Appl. Phys. Lett.*, vol. 105, no. 2, p. 23508, Jul. 2014.

[16] D. Delagebeaudeuf and N. T. Linh, "Metal-(n) AlGaAs-GaAs two-dimensional electron gas FET," *IEEE Trans. Electron Devices*, vol. 29, no. 6, pp. 955–960, Jun. 1982.

[17] Rashmi, A. Kranti, S. Haldar, M. Gupta, and R. S. Gupta, "Comprehensive analysis of small-signal parameters of fully strained and partially relaxed high Al-content lattice mismatched Al/sub m/Ga/sub 1-m/N/GaN HEMTs," *IEEE Trans. Microw. Theory Tech.*, vol. 51, no. 2, pp. 607–617, Feb. 2003.

[18] N. Karumuri, S. Turuvekere, N. Dasgupta, and A. Dasgupta, "A Continuous Analytical Model for 2-DEG Charge Density in AlGaN/GaN HEMTs Valid for All Bias Voltages," *IEEE Trans. Electron Devices*, vol. 61, no. 7, pp. 2343–2349, Jul. 2014.

[19] S. Khandelwal, N. Goyal, and T. A. Fjeldly, "A Physics-Based Analytical Model for 2DEG Charge Density in AlGaN/GaN HEMT Devices," *IEEE Trans. Electron Devices*, vol. 58, no. 10, pp. 3622–3625, Oct. 2011.

[20] J. D. Ye, S. Pannirselvam, S. T. Lim, J. F. Bi, X. W. Sun, G. Q. Lo, and K. L. Teo, "Two-dimensional electron gas in Zn-polar ZnMgO/ZnO heterostructure grown by metal-organic vapor phase epitaxy," *Appl. Phys. Lett.*, vol. 97, no. 11, p. 111908, Sep. 2010.

[21] R. Grundbacher, M. Nishimoto, T. P. Chin, Y. C. Chen, R. Lai, D. Yamauchi, M. Barsky, E. Sabin, R. Elmadjian, H. Rodgers, G. Schreyer, T. Block, V. Medvedev, and D. Streit, "Graded-barrier graded-channel InP pseudomorphic power HEMT with 40% power added efficiency and 200 mW output power at 60 GHz," in *1999 57th Annual Device Research Conference Digest (Cat. No.99TH8393)*, 1994, pp. 154–155.

[22] H. Yu, S. B. Lisesivdin, B. Bolukbas, O. Kelekci, M. K. Ozturk, S. Ozcelik, D. Caliskan, M. Ozturk, H. Cakmak, P. Demirel, and E. Ozbay, "Improvement of breakdown characteristics in AlGaN/GaN/AlxGa1−xN HEMT based on a grading AlxGa1−xN buffer layer," *Phys. status solidi*, vol. 207, no. 11, pp. 2593–2596, Nov. 2010.

[23] C.-I. Huang, H.-A. Chin, Y.-R. Wu, I.-C. Cheng, J. Z. Chen, K.-C. Chiu, and T.-S. Lin, "Mobility Enhancement of Polycrystalline MgZnO/ZnO Thin Film Layers With Modulation Doping and Polarization Effects," *IEEE Trans. Electron Devices*, vol. 57, no. 3, pp. 696–703, Mar. 2010.

[24] D. J. Cohen and S. A. Barnett, "Predicted electrical properties of modulation-doped ZnO-based transparent conducting oxides," *J. Appl. Phys.*, vol. 98, no. 5, p. 53705, Sep. 2005.

[25] H. Tampo, H. Shibata, K. Maejima, A. Yamada, K. Matsubara, P. Fons, S. Niki, T. Tainaka, Y. Chiba, and H. Kanie, "Strong excitonic transition of Zn1−xMgxO alloy," *Appl. Phys. Lett.*, vol. 91, no. 26, p. 261907, Dec. 2007.

[26] H. Matsui, H. Tabata, N. Hasuike, and H. Harima, "Critical thickness and lattice relaxation of Mg-rich strained Mg0.37Zn0.63O (0001) layers towards multi-quantum-wells," *J. Appl. Phys.*, vol. 99, no. 2, p. 24902, Jan. 2006.

[27] H. Matsui, N. Hasuike, H. Harima, T. Tanaka, and H. Tabata, "Stranski-Krastanov growth in Mg0.37Zn0.63O?ZnO heteroepitaxy: Self-organized nanodots and local composition separation," *Appl. Phys. Lett.*, vol. 89, no. 9, p. 91909, Aug. 2006.

[28] S. H. Park and D. Ahn, "Spontaneous and piezoelectric polarization effects in wurtzite ZnO/MgZnO quantum well lasers," *Appl. Phys. Lett.*, vol. 87, no. 25, p. 253509, Dec. 2005.

[29] S.-H. Jang and S. F. Chichibu, “Structural, elastic, and polarization parameters and band structures of wurtzite ZnO and MgO,” *J. Appl. Phys.*, vol. 112, no. 7, p. 73503, Oct. 2012.

[30] M. Yano, K. Hashimoto, K. Fujimoto, K. Koike, S. Sasa, M. Inoue, Y. Uetsuji, T. Ohnishi, and K. Inaba, “Polarization-induced two-dimensional electron gas at Zn1-xMgxO/ZnO heterointerface,” *J. Cryst. Growth*, vol. 301–302, no. SPEC. ISS., pp. 353–357, Apr. 2007.

[31] H. Tampo, H. Shibata, K. Maejima, T.-W. Chiu, H. Itoh, A. Yamada, K. Matsubara, P. Fons, Y. Chiba, T. Wakamatsu, Y. Takeshita, H. Kanie, and S. Niki, “Band profiles of ZnMgO/ZnO heterostructures confirmed by Kelvin probe force microscopy,” *Appl. Phys. Lett.*, vol. 94, no. 24, p. 242107, Jun. 2009.

[32] H. Tampo, H. Shibata, K. Maejima, A. Yamada, K. Matsubara, P. Fons, S. Kashiwaya, S. Niki, Y. Chiba, T. Wakamatsu, and H. Kanie, “Polarization-induced two-dimensional electron gases in ZnMgO/ZnO heterostructures,” *Appl. Phys. Lett.*, vol. 93, no. 20, p. 202104, Nov. 2008.

[33] I. P. Smorchkova, C. R. Elsass, J. P. Ibbetson, R. Vetury, B. Heying, P. Fini, E. Haus, S. P. DenBaars, J. S. Speck, and U. K. Mishra, “Polarization-induced charge and electron mobility in AlGaN/GaN heterostructures grown by plasma-assisted molecular-beam epitaxy,” *J. Appl. Phys.*, vol. 86, no. 8, pp. 4520–4526, Oct. 1999.

[34] S. Heikman, S. Keller, Y. Wu, J. S. Speck, S. P. DenBaars, and U. K. Mishra, “Polarization effects in AlGaN/GaN and GaN/AlGaN/GaN heterostructures,” *J. Appl. Phys.*, vol. 93, no. 12, pp. 10114–10118, Jun. 2003.

[35] J. P. Ibbetson, P. T. Fini, K. D. Ness, S. P. DenBaars, J. S. Speck, and U. K. Mishra, “Polarization effects, surface states, and the source of electrons in AlGaN/GaN heterostructure field effect

transistors," *Appl. Phys. Lett.*, vol. 77, no. 2, pp. 250–252, Jul. 2000.

[36] H.-A. Chin, I.-C. Cheng, C.-I. Huang, Y.-R. Wu, W.-S. Lu, W.-L. Lee, J. Z. Chen, K.-C. Chiu, and T.-S. Lin, "Two dimensional electron gases in polycrystalline MgZnO/ZnO heterostructures grown by rf-sputtering process," *J. Appl. Phys.*, vol. 108, no. 5, p. 54503, Sep. 2010.

[37] A. Malashevich and D. Vanderbilt, "First-principles study of polarization in Zn1-xMgxO," *Phys. Rev. B*, vol. 75, no. 4, p. 45106, Jan. 2007.

[38] Y. Zhang, M. Sun, S. J. Joglekar, T. Fujishima, and T. Palacios, "Threshold voltage control by gate oxide thickness in fluorinated GaN metal-oxide-semiconductor high-electron-mobility transistors," *Appl. Phys. Lett.*, vol. 103, no. 3, p. 33524, Jul. 2013.

Chapter 4

Fabrication of Au Schottky Contact on MgZnO

4.1 Introduction

As discussed in the previous chapter, the research activities are focused on ZnO and the alloy of ZnO i.e. MgZnO. ZnO and MgZnO are used as high-efficiency ultraviolet (UV) photodetectors, sensors, and heterojunction transistors such as high electron mobility transistors (HEMTs), which are further applied in defense applications, secure communications, radio telescopes, and high speed integrated circuits [1]–[5] due to their wide and direct band gap and large exciton binding energy. To realize these applications, the formation of high quality and reliable Schottky metal contact is one of the first crucial steps. As a typical wide bandgap semiconductor, MgZnO alloy have attracted increasing interest recently as a potential candidate for HEMT and detector applications. The fabrication of Au/MgZnO Schottky contact (SC) is crucial for sensor [6], ultraviolet (UV) detectors [7]–[9], and high electron mobility transistor (HEMT) [10] applications. For MgZnO based photodetectors, formation of a good-quality SC is essential on top of MgZnO layer [11]. In HEMTs based on MgZnO/ZnO heterostructure, in which MgZnO layer acts as the barrier layer [12], a good quality SC is essential on top of MgZnO layer, which acts as gate terminal to control the charge in the channel [10]. Formation of an efficient and reliable SC is one of the most crucial steps towards technology development and utilizing the potential of wide bandgap semiconductors for variety of applications.

For MgZnO to be a suitable alternative for HEMT-like applications, it is necessary for the transistor gate, which is a Schottky contact, to function in a reliable manner over a wider temperature range especially in lower ambient temperature as HEMT has applications in space technologies. Hence, an extensive temperature dependent study on MgZnO based Schottky contacts is undertaken here.

A number of techniques such as sol-gel mechanism [13], metal-organic chemical vapour deposition (MOCVD) [14], pulsed laser deposition (PLD) [15], molecular beam epitaxy (MBE) [16],and magnetron sputtering [17], [18] are deployed to grow MZO films. However, dual ion beam sputtering (DIBS) system is noteworthy to produce high-quality thin films with reasonably superior compositional stoichiometry, uniformity, and better film adhesion on larger substrate surface area [19], [20]. Other prime features of DIBS system are high-quality growth with reduced surface roughness (0.5 to 3.7 nm) [21] on a larger substrate area, *in-situ* substrate pre-cleaning before carrying out growth process, *in-situ* post-growth annealing, and better adhesion of film to the substrate [20], [22]. To the best of authors' knowledge, there have not been any reports available in the literature regarding an elaborated study on DIBS-grown SC formation on ZnO-materials. In this chapter, we discuss the formation and characterization of stable and reliable SC on $Mg_{0.05}Zn_{0.95}O$ film (MZO) grown by DIBS system. Previously, a number of pre-contact treatments of ZnO surface in oxidizing conditions, such as a remote O_2 plasma [23], ozone [24], or hydrogen peroxide [25], [26] are reported by researchers to reduce oxygen vacancies on the top surface of ZnO so that a reliable Schottky contact is formed. Interestingly, in our case, a reliable and stable Schottky contact formation is realized without any surface pre-treatments. In this chapter, we have discussed successful fabrication of efficient, reliable and stable Schottky metal contact of Au (100 nm) on $Mg_{0.05}Zn_{0.95}O$ (400 nm), grown on *p*-Si (111) substrate without any buffer layer by DIBS system for potential use in UV detectors, sensors and HEMTs.

4.2 Experimental Details

DIBS system, equipped with *radio-frequency* (RF) deposition ion beam source and *direct-coupled* assist ion source, has been deployed to deposit 400 nm MZO film, at 80% oxygen partial pressure (4 standard cubic centimeters per minute) and 300 °C growth temperature on *p*-Si (111) (~resistivity 2.4-3.6 ohm-cm) substrate utilizing a commercial 4-inch diameter $Mg_{0.05}Zn_{0.95}O$ target (99.99% pure). The working pressure inside the DIBS chamber is kept at 2.43×10^{-4} mbar. Prior to film deposition, the

substrate was ultrasonically cleaned in dilute hydrofluoric (HF) acid solution (HF to water volume ratio ~1:50) following meticulous rinsing in trichloroethane, acetone, and iso-propanol for 10 minutes each and then cleaned thoroughly in de-ionized water and subsequently purged by 5N purity (99.999%) nitrogen gas in order to remove organic contaminants.

For SC formation, 100 nm thick and 12.3816 μm^2 Au layer, has been grown on MZO, by using Au sputtering target at room temperature. For ohmic contact formation, indium contacts are soldered on MZO. The distance between Schottky and ohmic contacts is measured to be 0.9 mm. The electrical properties such as resistivity, carrier concentration, and mobility of MZO film are measured by four-probe Hall-effect measurement technique deploying the van der pauw configuration. The crystalline phase and crystal orientations of MZO film are determined by X-Ray diffraction (XRD) using Rigaku SmartLab system with Cu-Kα radiation (λ = 1.54 Å). The temperature dependent current-voltage (*I-V*) measurements are performed using 2612A Keithley source meter and Everbeing cryogenic probe station in the temperature range of 80 K to 300 K. The temperature dependent capacitance-voltage (*C-V*) measurements are accomplished with Hioki 3532-50 LCR Hi-Tester and Everbeing cryogenic probe station in the temperature range of 80 K to 300 K at 1 MHz. The thickness and roughness of film is measured by M-2000D J. A. Woollam rotating compensator spectroscopic ellipsometer. The elemental composition of MZO film is inspected by Energy Dispersive X-Ray (EDX, Zeiss Supra 55).

4.3 Results and Discussion

4.3.1 Material Characterization

XRD measurement demonstrates that MgZnO film is polycrystalline in nature with preferred MgZnO crystal orientation in (002) plane at 2θ = ~34.4°, which is associated with hexagonal wurtzite structure as shown in Fig. 4.1. The grain size is calculated as 43.55 nm by Scherrer's formula [27]. Resistivity, carrier concentration, and mobility of MZO film are evaluated to be 0.12 Ω-cm, 6.05×10^{17} cm^{-3}, 85.12 $cm^2V^{-1}s^{-1}$, respectively at room temperature. The thickness and roughness of the MZO film is

found to be (400 ± 0.48) nm and (3.45 ± 0.07) nm, respectively. The elemental composition of the deposited MZO film is confirmed by EDX measurement. EDX results presented in this paper is actually average values of the EDX spectra measured at different spatial locations on MZO sample. These points are taken over a large surface area (100 µm × 100 µm) to achieve an accurate chemical composition of MZO films. The atomic composition obtained from EDX in MZO film are: Mg- 4.66%, Zn- 34.35%, and O- 60.99%. The obtained stoichiometric composition of each element is in good agreement with the specified composition of the commercial sputtering target.

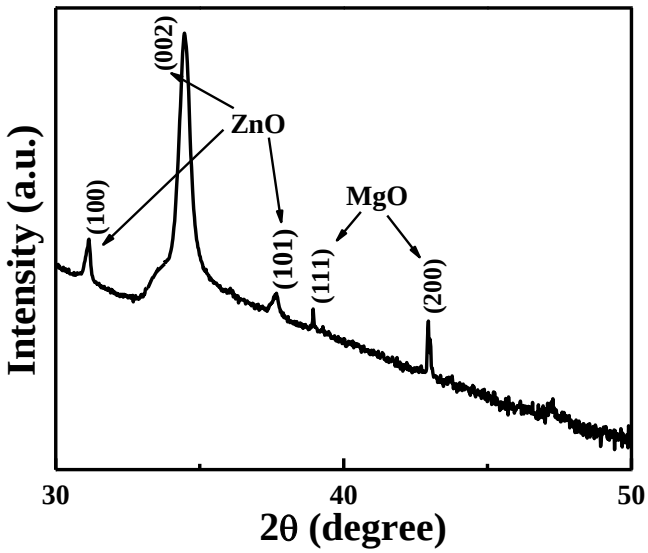

Fig. 4.1: XRD spectrum of MZO on Si.

4.3.2 *I-V* Characteristics

According to thermionic emission (TE) theory [28]**,** the *I-V* characteristics of the Schottky diode are given by equation (4.1).

$$I = I_0 \exp\left(\frac{q(V - IR_S)}{\eta kT}\right)\left[1 - \exp\left(-\frac{q(V - IR_S)}{kT}\right)\right] \quad (4.1)$$

where V is the applied voltage, R_S is the series resistance, η is the ideality factor, k is the Boltzmann constant and T is the absolute temperature. Saturation current, I_0 is given by equation (4.2).

$$I_0 = AA^*T^2 \exp\left(-\frac{q\phi_{(I-V)}}{kT}\right) \quad (4.2)$$

where, $\phi_{(I-V)}$ is the zero bias or apparent Schottky barrier height (SBH), A^* is the Richardson constant (theoretical value of A^* is 32 A.cm^{-2}.K^{-2} (for $m^* = 0.27m_e$)) for electrons in *n*-type ZnO and *A* is the effective Schottky contact area.

Fig. 4.2 (a) shows the forward and reverse *I-V* characteristics of Au/MZO Schottky diode, measured in the temperature range of 80-300 K in step of 20 K. Inset in Fig. 4.2 (a) shows the vertical cross-sectional schematic of the device. The diode has exhibited a good quality rectifying behavior and temperature-dependent current characteristics. The forward bias current displays an exponential increment with increasing bias voltage while reverse bias current shows relatively weaker voltage dependence. It is observed from the *I-V* curve that reverse saturation current decreases with decreasing temperature, which is in agreement to the predictions from TE theory. The value of experimentally obtained saturation current (I_0) is derived from the *y*-axis intercept of the linear portion of ln(*I*) versus *V* and ideality factor (η) is obtained from the slope of the forward bias ln(*I*)-*V*, for $V > 3kT/q$ and is given by equation (4.3) [28].

$$\eta = \frac{q}{kT}\left(\frac{dV}{d(\ln(I))}\right) \quad (4.3)$$

The values for $\phi_{(I-V)}$ are obtained using equation (4.2) and experimentally obtained values of I_0 at various temperature. The value of $\phi_{(I-V)}$ and η varies from 0.16 to 0.67 eV and 9.52 to 1.98, respectively, when temperature changes from 80 to 300 K. Different parameters obtained from the analysis of *I-V* measurement of Au/MZO in 80-300 K is listed in Table 4.1.

The temperature-dependent η and $\phi_{(I-V)}$ are shown in Fig. 4.2 (b). As shown in Fig. 4.2 (b), the value of η decreases while apparent barrier height, $\phi_{(I-V)}$ increases at approximately 2.27 meV/K with increasing ambient temperature within the range 80 to 300 K. The obtained results are in good

agreement with earlier reports by Asghar *et al*. [16]. In earlier reports, the non-ideal behavior of η and SBH have been attributed to various current conduction mechanisms apart from TE at the Schottky interface. Barrier tunneling and generation-recombination in depletion region are some of the mechanisms mostly referred to address such anomalous temperature-dependent behavior of η and SBH.

Table 4.1 Experimentally obtained parameters from I-V measurements of Au/MZO over the temperature range of 80-300 K.

Temperature, T (K)	Reverse saturation current, I_o (μA)	Apparent Schottky barrier height, $\phi_{(I-V)}$ (eV)	Ideality factor, η	Rectification ratio, $\frac{I_F}{I_R}$ at 1.5 V
80	1.16	0.16	9.52	34.38
100	1.25	0.21	8.48	22.42
120	1.39	0.25	6.63	22.10
140	1.72	0.30	6.38	21.38
160	1.84	0.34	4.97	19.26
180	1.87	0.39	4.81	24.25
200	1.85	0.43	4.20	23.63
220	1.87	0.48	3.31	22.69
240	2.06	0.53	3.17	21.70
260	2.25	0.57	2.54	20.68
280	2.13	0.62	2.37	19.70
300	2.36	0.67	1.98	18.40

Werner and Güttler [29] has attributed the non-idealities of SBH to BH inhomogeneities. BH inhomogeneity can be caused due to a number of factors including non-uniform metal thickness, interface layer composition, grain boundaries etc. Moreover, it was suspected that the localization of

electric field in certain patches might contribute to a lateral reduction of SBH [30]. By the ballistic electron emission microscopy investigations, it has been demonstrated that the metal-semiconductor (MS) interface has an inhomogeneous area consisting of patches of relatively lower or higher values of BH with respect to the mean value of BH [31]. Tung [32] and Sullivan *et al*. [33] has proposed a modified TE theory of patchy Schottky barriers for explaining SBH inhomogeneities at MS interface.

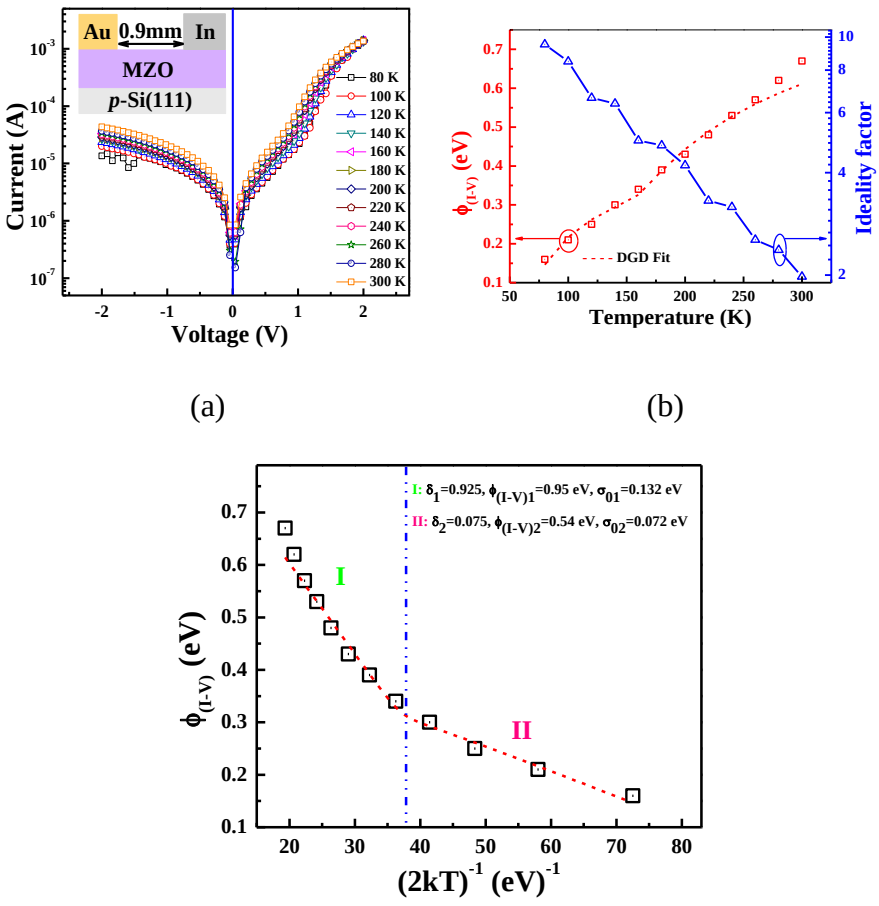

(a) (b)

(c)

Fig. 4.2: (a) Semi-log I-V plots of Au/MZO Schottky diode in the temperature range of 80-300 K. Inset shows schematic structure of Schottky diode. (b) Effect of measurement temperature on ideality factor and barrier height of Schottky diode with analytical DGD fitting the experimentally obtained SBH. (c) Zero-bias apparent barrier height versus 1/2kT curve of Au/MZO Schottky diode fitted by a DGD (red broken line) of SBH at MS interface.

Song *et al*. [30] introduced a model for current in low and moderate temperatures by considering a Gaussian distribution (GD) of BH [34], [35]. This model assumes the MS interface of a Schottky barrier to be comprising of a number of parallel diodes with different BHs and every patch could contribute independently to the total flow of current. Then, a normalized GD function $f(\phi_{(I-V)})$ for BH inhomogeneity, provided $\sum_i \delta_i$,=1, can be written as in equation (4.4).

$$f(\phi_{(I-V)}) = \sum_{i=1}^{N} \frac{\delta_i}{\sigma_{0i}\sqrt{2\pi}} \exp\left[-\frac{\phi_{(I-V)i} - \phi_{(I-V)}}{2\sigma_{0i}^2}\right] \qquad (4.4)$$

where δ_i, σ_{0i} and $\phi_{(I-V)i}$ represent weight, standard deviation, and the mean value of i^{th} GD of BH, respectively. It was pointed out by Tung [32] that if the SC patch with lower BH has lateral dimensions comparable to the depletion width of MS junction then depending on such local lateral barrier patches, applied bias voltage, and temperature of operation, SC may get pinched-off. The current across an MS interface with BH inhomogeneities actually flows through these patches following equation (4.1) with different values of temperature-dependent $\phi_{(I-V)i}$ and η. The temperature-dependent $\phi_{(I-V)}$ for an inhomogeneous Schottky barrier with multiple GD is given in equation (4.5) [36]–[38].

$$\phi_{(I-V)} = \frac{kT}{q}\, ln \sum_{i=1}^{N} \delta_i \exp\left[\frac{q\phi_{(I-V)i}}{kT} - \frac{1}{2}\left(\frac{q\sigma_{0i}}{kT}\right)^2\right] \qquad (4.5)$$

For single BH (SBH) patch (N=1) with inhomogeneous barrier distribution of σ_{01}, equation (4.5) can be represented by equation (4.6).

$$\phi_{(I-V)} = \phi_{(I-V)1} - \frac{q\sigma_{01}^2}{2kT} \qquad (4.6)$$

The plot of $\phi_{(I-V)}$ versus $(2kT)^{-1}$, as per equation (4.6), should have been a straight line curve with a slope of σ_{01}^2 and intercept of $\phi_{(I-V)1}$. However, the experimentally obtained temperature-dependent characteristics of $\phi_{(I-V)}$, as in Fig. 4.2 (c), does not correspond to SBH condition; instead it

represented two separate straight line curves with a transition at 160 K. This signifies the presence of a double Gaussian distribution (DGD) of BH at Schottky interface [34], [38], [39], which can be mathematically represented as in equation (4.7).

$$\phi_{(I-V)} = \frac{kT}{q} \ln \left[\delta_1 \exp\left(\frac{q\phi_{(I-V)1}}{kT} - \frac{1}{2}\left(\frac{q\sigma_{01}}{kT}\right)^2 \right) + \delta_2 \exp\left(\frac{q\phi_{(I-V)2}}{kT} - \frac{1}{2}\left(\frac{q\sigma_{02}}{kT}\right)^2 \right) \right] \quad (4.7)$$

The red broken line with two different values of slope and intercept, designated as region I and II as in Fig. 4.2 (c), is the theoretically obtained $\phi_{(I-V)}$ with fitting parameters of δ_1= 0.925, $\phi_{(I-V)1}$= 0.95 eV and σ_{01}= 0.131 eV for 160-300 K and δ_2= 0.075, $\phi_{(I-V)2}$= 0.54 eV and σ_{02}= 0.072 eV for 80-160 K and is fitted with experimentally obtained $\phi_{(I-V)}$. The perfect correlation of the theoretical approach with the experimental results, as in Fig. 4.2 (c), indicates that the DGD model can precisely describe the BH inhomogeneity for our Au/MZO device. Experimentally obtained temperature-dependent $\phi_{(I-V)}$ and the corresponding DGD fitting curve are displayed in Fig. 4.2 (b).

A high value of weight, δ_1 (> 0.9) for region I, as in Fig. 4.2 (c), shows the dominance of SC patches with comparatively larger values of BH at MS interface. Moreover, a high value of standard deviation (0.131 eV, which is deviated by 10% as compared to the value of $\phi_{(I-V)1}$) for region I represents the presence of high SBH inhomogeneity at Schottky interface. This larger inhomogeneity is associated with the surface interface traps induced by the chemical reaction between Au and MZO during the formation of SC. Such defects trigger the formation of a large density of interface states, which are continuously distributed within the band gap energy and cause leakage currents to flow across the device. Since, the grain size, as observed by XRD, is ~43.55 nm, grain boundaries may also contribute to trap states. Moreover, bulk defects in films may also induce trap states, which on the other hand, may have some impact on the Schottky barrier in wide band gap semiconductors [40].

However, in this work, it is observed that $\phi_{I-V} < \phi_{C-V}$ (Apparent Schottky barrier height from C-V measurements), which is discussed in detail in later section. This observation suggests that bulk defects have no significant contribution in electrical performance of SC formed [40]. The carrier trapping defect states introduced by grain boundaries are significantly smaller in number compared to carrier-trapping defect states introduced by bulk defects in MZO film and thus the effect of grain boundaries does not play a significant role in this case [41], [42].

Table 4.2 Comparison of η and $\phi_{(I-V)}$ at room temperature with corresponding reported values in literature.

Parameter	This work	Ref. [43]	Ref. [16]	Ref. [44]	Ref. [45]	Ref. [46]
Ideality factor (η)	**1.98**	4.56	2.15	1.84	2.36	1.82
Apparent Schottky barrier height ($\phi_{(I-V)}$) (eV)	**0.67**	0.48	0.6	0.79	0.67	0.61
Schottky junction	$\frac{\boldsymbol{Au}}{\boldsymbol{MZO}}$	$\frac{Au}{MgZnO}$	$\frac{Au}{ZnO}$	$\frac{Au}{ZnO}$	$\frac{Au}{MgZnO}$	$\frac{Au}{ZnO}$
Deposition method	**DIBS**	MOCVD	MBE	Hydrothermal	PLD	MOCVD

Table 4.2 shows the comparative study of obtained values of η and $\phi_{(I-V)}$ from DIBS-grown Schottky diode with the corresponding values of diode, as reported in literature. The values of ideality factor and barrier height of

Au/MZO Schottky contact fabricated by DIBS is found to be comparable and in some cases better than those from Schottky junctions formed by MOCVD, PLD, MBE, and hydrothermal processes [16], [43]–[46].

It should be noted that in the analysis of SC, the doping (i.e. charge carrier) concentration and Mg composition in MZO film are kept constant. However, researchers have reported the variation of η and $\phi_{(I-V)}$ with doping level and Mg composition. Brillson *et al* [41] have reported that the value of ideality factor increases and Schottky barrier height decreases with an increase in native defects in MgZnO. The increase in native defect implies an increase in electron concentration in MgZnO [42]. The increase in carrier concentration is attributed to the tunnelling effect which, in turn, decreases the Schottky barrier height and increases the ideality factor. The values of $\phi_{(I-V)}$ and η are observed to decline when Mg composition (x) in $Mg_xZn_{1-x}O$ is changed from 0-5% [9]. However, Wenckstern *et al* [47] have reported random variation of $\phi_{(I-V)}$ and η with Mg composition.

In order to comprehend the barrier inhomogeneity variation at metal/semiconductor interface temperature dependent investigation is necessary [48]. The performance and reliability of Schottky-based devices is governed by the density of interface states as well as the distribution of such states [49] and thus, it is discussed in the later section.

4.3.3 *C-V* Characteristics

The *C-V* measurements of Au/MZO Schottky diode has been carried out to determine the quality of metal-semiconductor interface as well as barrier height. Fig. 4.3 (a) represents the experimental reverse bias C^{-2}-V characteristics of the Schottky contact over the temperature range of 80–300 K. The metal-semiconductor junction capacitances are measured at 1 MHz operating frequency. In Schottky diodes, the depletion layer capacitance is expressed as in equation (4.8) [50].

$$\frac{1}{C^2} = \left(\frac{2}{\epsilon_S q N_D A^2}\right)\left(V_{bi} - \frac{kT}{q} - V\right) \tag{4.8}$$

where N_D, A, and ϵ_S are ionized donar concentration, area of the Schottky contact, and permittivity of the semiconductor ($\epsilon_s = 8.8\epsilon_0$, ϵ_0 is permittivity of free-space), respectively. The x-axis intercept of the C^{-2}-V plot gives the diffusion potential (V_o) and it is related to the built-in potential (V_{bi}) as:

$$V_{bi} = V_o + \frac{kT}{q} \tag{4.9}$$

The Apparent Schottky barrier height from C-V measurements ($\phi_{(C-V)}$) thus can be calculated using:

$$\phi_{(C-V)} = V_{bi} + \frac{kT}{q}\ln\left(\frac{N_C}{N_D}\right) - \Delta\phi_b \tag{4.10}$$

Where, N_C is the density of states in conduction band:

$$N_C = 2\left(\frac{2\pi m^* kT}{h^2}\right)^{\frac{3}{2}} \tag{4.11}$$

where m^* is the effective mass of electron ($m^* = 0.27m_o$), m_o is the rest mass of electron and $\Delta\phi_b$ is the image force barrier lowering:

$$\Delta\phi_b = \left(\frac{qE_m}{4\pi\epsilon_S}\right)^{\frac{1}{2}} \tag{4.12}$$

where E_m is maximum electric field and is given as:

$$E_m = \left(\frac{2qV_0N_D}{4\pi\epsilon_S}\right)^{\frac{1}{2}} \tag{4.13}$$

In Table 4.3, values of experimentally determined diffusion potential (V_o), built-in potential (V_{bi}), image force barrier lowering ($\Delta\phi_b$) and SBH ($\phi_{(C-V)}$) are listed.

Table 4.3 Experimentally obtained parameters from C-V measurements of Au/MZO over the temperature range of 80-300 K.

Temperature, T (K)	Diffusion potential, V_0 (eV)	Built-in potential, V_{bi} (eV)	Image force barrier lowering, $\Delta\phi_b$ (eV)	Apparent Schottky barrier height, $\phi_{(C-V)}$ (eV)
80	1.98	1.99	0.0121	2.02
100	1.90	1.91	0.0121	1.95
120	1.70	1.71	0.0119	1.77
140	1.56	1.57	0.0117	1.64
160	1.46	1.47	0.0116	1.56
180	1.35	1.37	0.0115	1.46
200	1.23	1.25	0.0113	1.36
220	1.09	1.11	0.0111	1.24
240	1.00	1.02	0.0109	1.16
260	0.90	0.92	0.0108	1.08
280	0.81	0.83	0.0106	1.00
300	0.69	0.71	0.0103	0.90

As demonstrated in Fig. 4.3 (b), $\phi_{(C-V)}$ reduces with the corresponding rise in measurement temperature. The temperature dependence of $\phi_{(C-V)}$ can be expressed as [29]

$$\phi_{(C-V)} = \phi_{(C-V)}(0\ K) + \alpha T \qquad (4.14)$$

where $\phi_{(C-V)}$ (0 K) is the barrier height extrapolated to 0 K and α is the temperature coefficient of the barrier height.

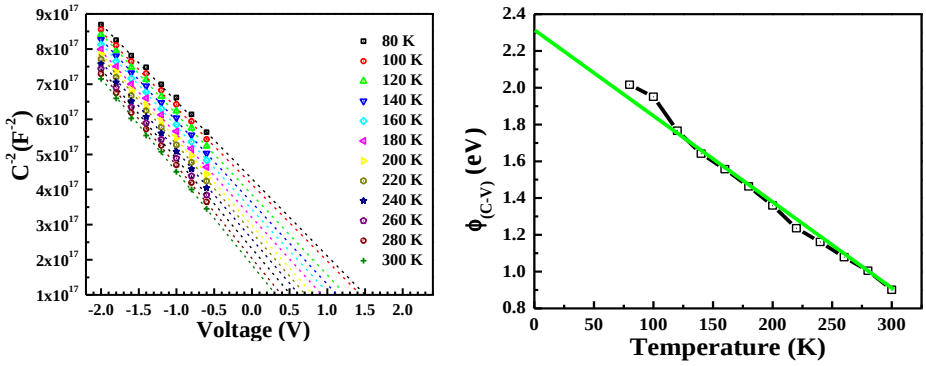

(a) (b)

Fig. 4.3: (a) C^{-2} vs. V characteristics of Au/MZO Schottky diode in the temperature range of 80-300 K. (b) $\phi_{(C-V)}$ vs. measurement temperature for Au/MZO Schottky contact.

From the linear fitting of experimental $\phi_{(C-V)}$ data shown in Fig. 4.3 (b), the $\phi_{(C-V)}$ (0 K) and α are evaluated to be 2.30 eV and -4.68×10^{-3} eVK^{-1}, respectively. The temperature dependence of the barrier height follows the temperature dependence of the band gap of MZO. This is due to the decrease in barrier height (BH) with increasing temperature associated with the shrinking of the band gap of MZO at higher temperature [51], [52]. The values of BH obtained from temperature dependent *C-V* (C-V-T) measurements are larger than those obtained from temperature dependent *I-V* (I-V-T) measurements. The reason for this discrepancy is that current in the *I-V* measurement is dominated by the current component which flows through the region of low SBH, and thus the measured *I-V* SBH is significantly lower than the weighted arithmetic average of the SBHs of different SB patches present at MS interface. On the other hand, SBH measured from the *C-V* is influenced by the distribution of charges at the depletion region boundary and this charge distribution follows the weighted arithmetic average of the SBHs [29].

4.3.4 Interface States

Fig. 4.4 (a) shows a schematic description of interface states present at the interface of Au/MZO. The evaluation of the interface states density (N_{SS}) and relative interfacial layer thickness (δ) can be performed using the method described by Card and Rhoderick [28] and Kolnik and Ozvold [53]. The energy of the interface states (E_{SS}) with respect to the bottom of the conduction band (E_C) at the surface of an *n*-type MZO is given by [54]–[59]:

$$E_C - E_{SS} = q(\phi_e - V) \tag{4.15}$$

where ϕ_e is the effective barrier height, and *V* is applied bias voltage. The voltage dependence of the effective barrier height (ϕ_e) is expressed as [60]:

$$\phi_e = \phi_{(C-V)} + \left(1 - \frac{1}{\eta}\right)(V - IR_S) \tag{4.16}$$

For MS junction having interface states in equilibrium with the semiconductor, the ideality factor (η) becomes greater than unity, as proposed by Card and Rhoderick [28], and is given by [60]:

$$\eta = 1 + \frac{\delta}{\epsilon_i}\left(\frac{\epsilon_s}{W} + qN_{ss}\right) \tag{4.17}$$

The value of N_{SS} can be obtained by using equation (4.17).

$$N_{SS} = \frac{1}{q}\left[\frac{\epsilon_i}{\delta}(\eta - 1) - \frac{\epsilon_s}{W}\right] \tag{4.18}$$

where *W* is the space charge width and ϵ_s and ϵ_i are the permittivities of the semiconductor and the interfacial layer, respectively. The space charge width W that can be written as:

$$W = \frac{\epsilon_S A}{C(V)} \tag{4.19}$$

The value of δ/ϵ_i is determined by [53], [61].

$$\frac{\delta}{\epsilon_i} = \left[\frac{\epsilon_s}{W}\left(\frac{1}{\beta_r} - 1\right)\right] \tag{4.20}$$

The interfacial layer thickness (δ) is evaluated using the interfacial layer permittivity, $\epsilon_i = 4\epsilon_0$ [62] and β_r which is the slope of the reverse bias I-V curve and is given by [63]:

$$\beta_r = \left(\frac{kT}{q}\right)\frac{d(\ln I)}{dV} \tag{4.21}$$

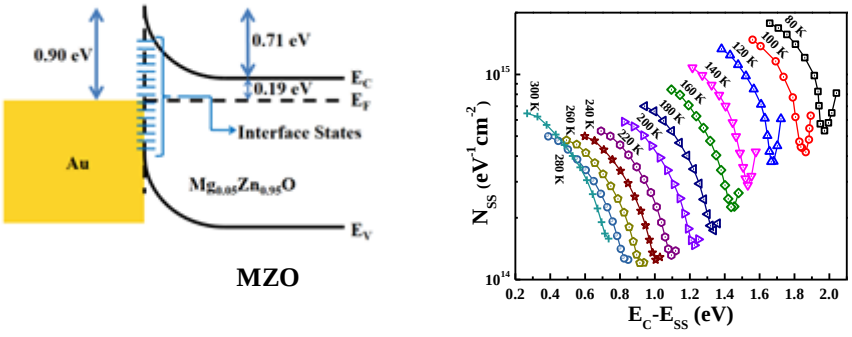

(a) (b)

Fig. 4.4: (a) Energy band diagram of the Au/MZO interface at 300 K, (b) energy distribution profiles of interface states obtained from the forward bias I-V characteristics of Schottky diode in the temperature range of 80-300 K.

Equations (4.15) - (4.21), along with the forward and reverse bias *I-V* characteristics are used to determine the interface states density (N_{SS}) as a function of difference of energy of interface states (E_{SS}) from the bottom of conduction band (E_C). Fig. 4.4 (b) demonstrates interface state density distribution profiles measured at 20 K interval in the temperature range of 80-300 K. As can be observed in Fig. 4.4 (b), the value of N_{SS} decreases with the increasing values of (E_C-E_{SS}) at each measured temperature. The temperature-dependent variation of interface state density at the Schottky junction is noticed to follow that of temperature-dependent ideality factor, as observed in Fig. 4.2 (b) [28]. The value of interface state density measured at 300 K, varies from 6.46×10^{14} $eV^{-1}cm^{-2}$ at E_C-0.27 eV to

1.58×10^{14} $eV^{-1}cm^{-2}$ at E_C-0.74 eV. Aydogan *et al*. have reported a value of 1.73×10^{14} $eV^{-1}cm^{-2}$ for Au/ZnO Schottky diode [64]. Kim *et al.* have reported the interface state density has changed from 1.72×10^{13} $eV^{-1}cm^{-2}$ at E_C-0.32 eV to 1.68×10^{12} $eV^{-1}cm^{-2}$ at E_C-0.54 eV for Ag/ZnO Schottky diode [65]. Our reported values of N_{SS} from DIBS-grown SC are comparable to those obtained by Aydogan *et al* [64].

4.4 Conclusion

We have realized Au/MZO Schottky contact fabricated using DIBS system. A thorough electrical characterization is performed to obtain (or extract) various parameters of a Schottky contact. The values of barrier height and ideality factor of Schottky junction formed using DIBS are found to be comparable and in some cases better than those obtained from SC as fabricated by other traditional fabrication processes. Temperature dependent study for the SC is undertaken to ascertain causes for deviation of *I-V* and *C-V* characteristics from their ideal behavior. Numerical calculations reveal that with increasing measurement temperature, the barrier height increases and ideality factor decreases, as evaluated from *I-V* measurements. This anomalous temperature dependence of the barrier height and ideality factor can be associated with the nature of inhomogeneous Schottky barrier consisting of a combination of low and high barrier patches. Temperature-dependent SBH describes a DGD with mean apparent barrier heights of 0.95 and 0.54 eV and standard deviations of 0.131 and 0.074 eV in the temperature range of 160-300 K and 80-160 K, respectively. The larger value of SBH inhomogeneity is attributed to interface states at MS junction. The interface state density at 300 K varies from 6.46×10^{14} $eV^{-1}cm^{-2}$ at E_C-0.27 eV to 1.58×10^{14} $eV^{-1}cm^{-2}$ at E_C-0.74 eV. Thus, it is concluded that the presence of barrier inhomogeneity and interface state density is the main reason for deviation of Schottky junction characteristics from its ideal behavior.

4.5 References

[1] T. Mimura, "The early history of the high electron mobility transistor (HEMT)," *IEEE Trans. Microw. Theory Tech.*, vol. 50, no. 3, pp. 780–782, Mar. 2002.

[2] P. Sharma, A. Mansingh, and K. Sreenivas, "Ultraviolet photoresponse of porous ZnO thin films prepared by unbalanced magnetron sputtering," *Appl. Phys. Lett.*, vol. 80, no. 4, pp. 553–555, Jan. 2002.

[3] S. A. Studenikin, N. Golego, and M. Cocivera, "Carrier mobility and density contributions to photoconductivity transients in polycrystalline ZnO films," *J. Appl. Phys.*, vol. 87, no. 5, pp. 2413–2421, Mar. 2000.

[4] Y. Takahashi, M. Kanamori, A. Kondoh, H. Minoura, and Y. Ohya, "Photoconductivity of Ultrathin Zinc Oxide Films," *Jpn. J. Appl. Phys.*, vol. 33, no. Part 1, No. 12A, pp. 6611–6615, Dec. 1994.

[5] D. H. Zhang and D. E. Brodie, "Effects of annealing ZnO films prepared by ion-beam-assisted reactive deposition," *Thin Solid Films*, vol. 238, no. 1, pp. 95–100, Jan. 1994.

[6] S. K. Mohanta, A. Nakamura, G. Tabares, A. Hierro, Á. Guzmán, E. Muñoz, and J. Temmyo, "Electrical characterization of Schottky contacts to n-MgZnO films," *Thin Solid Films*, vol. 548, pp. 539–545, Dec. 2013.

[7] Y. An, A. Behnam, E. Pop, and A. Ural, "Metal-semiconductor-metal photodetectors based on graphene/ p -type silicon Schottky junctions," *Appl. Phys. Lett.*, vol. 102, no. 1, p. 013110, Jan. 2013.

[8] T. Ikenoue, N. Kameyama, and S. Fujita, "Fabrication of PEDOT:PSS/ZnMgO Schottky-type ultraviolet sensors on glass substrates with solution-based mist deposition technique and hard-mask patterning," *Phys. status solidi*, vol. 8, no. 2, pp. 613–615, Feb.

2011.

[9] S. Singh, G. R. Dillip, S. Vyas, M. Roqibul Hasan, I.-K. Park, P. Chakrabarti, and S.-H. Park, "Fabrication and characterization of hydrothermally grown MgZnO nanorod films for Schottky diode applications," *Microsyst. Technol.*, vol. 23, no. 1, pp. 39–46, Jan. 2017.

[10] I.-C. Cheng, B.-S. Wang, H.-H. Hou, and J.-Z. Chen, "MgZnO/ZnO Heterostructure Field-Effect Transistors Fabricated by RF-Sputtering," *ECS Trans.*, vol. 50, no. 8, pp. 83–93, Mar. 2013.

[11] R. Liu, D. Jiang, M. Zhou, G. Yang, L. Sun, C. Tian, S. Gao, Q. Liang, J. Zhao, and J. Hou, "A practicable route to improve the responsivity of Mg0.2Zn0.8O ultraviolet photodetectors," *Opt. Commun.*, vol. 346, pp. 43–46, Jul. 2015.

[12] H.-A. Chin, I.-C. Cheng, C.-K. Li, Y.-R. Wu, J. Z. Chen, W.-S. Lu, and W.-L. Lee, "Electrical properties of modulation-doped rf-sputtered polycrystalline MgZnO/ZnO heterostructures," *J. Phys. D. Appl. Phys.*, vol. 44, no. 45, p. 455101, Nov. 2011.

[13] M. Wang, E. J. Kim, S. Kim, J. S. Chung, I.-K. Yoo, E. W. Shin, S. H. Hahn, and C. Park, "Optical and structural properties of sol–gel prepared MgZnO alloy thin films," *Thin Solid Films*, vol. 516, no. 6, pp. 1124–1129, Jan. 2008.

[14] W. Liu, S. Gu, S. Zhu, J. Ye, F. Qin, S. Liu, X. Zhou, L. Hu, R. Zhang, Y. Shi, and Y. Zheng, "The deposition and annealing study of MOCVD ZnMgO," *J. Cryst. Growth*, vol. 277, no. 1–4, pp. 416–421, Apr. 2005.

[15] M.-H. Liang, Y.-T. Ho, W.-L. Wang, C.-Y. Peng, and L. Chang, "Growth of ZnMgO/ZnO films on r-plane sapphires by pulsed laser deposition," *J. Cryst. Growth*, vol. 310, no. 7–9, pp. 1847–1852, Apr. 2008.

[16] M. Asghar, K. Mahmood, F. Malik, and M. A. Hasan, “Growth and interface properties of Au Schottky contact on ZnO grown by molecular beam epitaxy,” *J. Phys. Conf. Ser.*, vol. 439, no. 1, p. 012031, Jun. 2013.

[17] S. Kumar, V. Gupte, and K. Sreenivas, “Structural and optical properties of magnetron sputtered Mg x Zn 1− x O thin films,” *J. Phys. Condens. Matter*, vol. 18, no. 13, pp. 3343–3354, Apr. 2006.

[18] T. Minemoto, T. Negami, S. Nishiwaki, H. Takakura, and Y. Hamakawa, “Preparation of Zn1−xMgxO films by radio frequency magnetron sputtering,” *Thin Solid Films*, vol. 372, no. 1–2, pp. 173–176, Sep. 2000.

[19] S. K. Pandey, S. K. Pandey, V. Awasthi, A. Kumar, M. Gupta, V. Sathe, and S. Mukherjee, “Behavior of dual ion beam sputtered MgZnO thin films for different oxygen partial pressure,” *J. Mater. Sci. Mater. Electron.*, vol. 25, no. 2, pp. 772–777, Feb. 2014.

[20] S. K. Pandey, S. Kumar Pandey, V. Awasthi, M. Gupta, U. P. Deshpande, and S. Mukherjee, “Influence of in-situ annealing ambient on p-type conduction in dual ion beam sputtered Sb-doped ZnO thin films,” *Appl. Phys. Lett.*, vol. 103, no. 7, p. 072109, Aug. 2013.

[21] S. K. Pandey, S. K. Pandey, C. Mukherjee, P. Mishra, M. Gupta, S. R. Barman, S. W. D’Souza, and S. Mukherjee, “Effect of growth temperature on structural, electrical and optical properties of dual ion beam sputtered ZnO thin films,” *J. Mater. Sci. Mater. Electron.*, vol. 24, no. 7, pp. 2541–2547, Jul. 2013.

[22] S. K. Pandey, S. K. Pandey, U. P. Deshpande, V. Awasthi, A. Kumar, M. Gupta, and S. Mukherjee, “Effect of oxygen partial pressure on the behavior of dual ion beam sputtered ZnO thin films,” *Semicond. Sci. Technol.*, vol. 28, no. 8, p. 085014, Aug. 2013.

[23] H. L. Mosbacker, Y. M. Strzhemechny, B. D. White, P. E. Smith, D. C. Look, D. C. Reynolds, C. W. Litton, and L. J. Brillson, "Role of near-surface states in ohmic-Schottky conversion of Au contacts to ZnO," *Appl. Phys. Lett.*, vol. 87, no. 1, p. 012102, Jul. 2005.

[24] K. Ip, B. . Gila, A. . Onstine, E. . Lambers, Y. . Heo, K. . Baik, D. . Norton, S. . Pearton, S. Kim, J. . LaRoche, and F. Ren, "Effect of ozone cleaning on Pt/Au and W/Pt/Au Schottky contacts to n-type ZnO," *Appl. Surf. Sci.*, vol. 236, no. 1–4, pp. 387–393, Sep. 2004.

[25] S.-H. Kim, H.-K. Kim, and T.-Y. Seong, "Effect of hydrogen peroxide treatment on the characteristics of Pt Schottky contact on n-type ZnO," *Appl. Phys. Lett.*, vol. 86, no. 11, p. 112101, Mar. 2005.

[26] R. Schifano, E. V. Monakhov, U. Grossner, and B. G. Svensson, "Electrical characteristics of palladium Schottky contacts to hydrogen peroxide treated hydrothermally grown ZnO," *Appl. Phys. Lett.*, vol. 91, no. 19, p. 193507, Nov. 2007.

[27] S. Kahraman, F. Bayansal, H. A. Çetinkara, H. M. Çakmak, and H. S. Güder, "Characterization of CBD grown ZnO films with high c-axis orientation," *Mater. Chem. Phys.*, vol. 134, no. 2–3, pp. 1036–1041, Jun. 2012.

[28] H. C. Card and E. H. Rhoderick, "Studies of tunnel MOS diodes I. Interface effects in silicon Schottky diodes," *J. Phys. D. Appl. Phys.*, vol. 4, no. 10, p. 319, Oct. 1971.

[29] J. H. Werner and H. H. Güttler, "Barrier inhomogeneities at Schottky contacts," *J. Appl. Phys.*, vol. 69, no. 3, pp. 1522–1533, Feb. 1991.

[30] Y. P. Song, R. L. Van Meirhaeghe, W. H. Laflère, and F. Cardon, "On the difference in apparent barrier height as obtained from capacitance-voltage and current-voltage-temperature measurements on Al/p-InP Schottky barriers," *Solid. State. Electron.*, vol. 29, no.

6, pp. 633–638, Jun. 1986.

[31] G. M. Vanalme, R. L. Van Meirhaeghe, F. Cardon, and P. Van Daele, “A ballistic electron emission microscopy (BEEM) study of the barrier height change of Au/n-GaAs Schottky barriers due to reactive ion etching,” *Semicond. Sci. Technol.*, vol. 12, no. 7, pp. 907–912, Jul. 1997.

[32] R. T. Tung, “Electron transport at metal-semiconductor interfaces: General theory,” *Phys. Rev. B*, vol. 45, no. 23, pp. 13509–13523, Jun. 1992.

[33] J. P. Sullivan, R. T. Tung, M. R. Pinto, and W. R. Graham, “Electron transport of inhomogeneous Schottky barriers: A numerical study,” *J. Appl. Phys.*, vol. 70, no. 12, pp. 7403–7424, Dec. 1991.

[34] S. Chand and J. Kumar, “Evidence for the double distribution of barrier heights in Schottky diodes from I - V - T measurements,” *Semicond. Sci. Technol.*, vol. 11, no. 8, pp. 1203–1208, Aug. 1996.

[35] R. T. Tung, J. P. Sullivan, and F. Schrey, “On the inhomogeneity of Schottky barriers,” *Mater. Sci. Eng. B*, vol. 14, no. 3, pp. 266–280, Aug. 1992.

[36] I. Ohdomari and K. N. Tu, “Parallel silicide contacts,” *J. Appl. Phys.*, vol. 51, no. 7, pp. 3735–3739, Jul. 1980.

[37] B. Abay, “Measurement and modelling of the characteristic parameters for silver Schottky contacts on layered p-GaSe compound in a wide temperature range,” *J. Alloys Compd.*, vol. 506, no. 1, pp. 51–56, Sep. 2010.

[38] N. Yıldırım, A. Turut, and V. Turut, “The theoretical and experimental study on double-Gaussian distribution in inhomogeneous barrier-height Schottky contacts,” *Microelectron. Eng.*, vol. 87, no. 11, pp. 2225–2229, Nov. 2010.

[39] Y.-L. Jiang, G.-P. Ru, F. Lu, X.-P. Qu, B.-Z. Li, and S. Yang, “Ni/Si solid phase reaction studied by temperature-dependent current-voltage technique,” *J. Appl. Phys.*, vol. 93, no. 2, pp. 866–870, Jan. 2003.

[40] M. W. Allen and S. M. Durbin, “Influence of oxygen vacancies on Schottky contacts to ZnO,” *Appl. Phys. Lett.*, vol. 92, no. 12, p. 122110, Mar. 2008.

[41] L. J. Brillson, H. L. Mosbacker, M. J. Hetzer, Y. Strzhemechny, G. H. Jessen, D. C. Look, G. Cantwell, J. Zhang, and J. J. Song, “Dominant effect of near-interface native point defects on ZnO Schottky barriers,” *Appl. Phys. Lett.*, vol. 90, no. 10, p. 102116, Mar. 2007.

[42] A. Janotti and C. G. Van de Walle, “Fundamentals of zinc oxide as a semiconductor,” *Reports Prog. Phys.*, vol. 72, no. 12, p. 126501, Dec. 2009.

[43] S. Han, J. Y. Zhang, Z. Z. Zhang, L. K. Wang, Y. M. Zhao, J. Zheng, J. M. Cao, B. Yao, D. X. Zhao, and D. Z. Shen, “Contact Properties of Au/Mg 0.27 Zn 0.73 O by Different Annealing Processes,” *J. Phys. Chem. C*, vol. 114, no. 49, pp. 21757–21761, Dec. 2010.

[44] J.-D. Hwang, C.-Y. Kung, and Y.-L. Lin, “Non-Surface-Treated Au/ZnO Schottky Diodes Using Pre-Annealed Hydrothermal or Sol-Gel Seed Layer,” *IEEE Trans. Nanotechnol.*, vol. 12, no. 1, pp. 35–39, Jan. 2013.

[45] J. H. Lee, C. H. Kim, A. R. Kim, H. S. Kim, N. W. Jang, Y. Yun, J.-G. Kim, M. W. Pin, and W. J. Lee, “Schottky Diodes Prepared with Ag, Au, or Pd Contacts on a MgZnO/ZnO Heterostructure,” *Jpn. J. Appl. Phys.*, vol. 51, no. 9 PART3, p. 09MF07, Sep. 2012.

[46] S. Lee, Y. Lee, D. Y. Kim, and T. Won Kang, “Impact of defect distribution on transport properties for Au/ZnO Schottky contacts

formed with H2O2-treated unintentionally doped n-type ZnO epilayers," *Appl. Phys. Lett.*, vol. 96, no. 14, p. 142102, Apr. 2010.

[47] H. von Wenckstern, K. Brachwitz, M. Schmidt, C. P. Dietrich, M. Ellguth, M. Stölzel, M. Lorenz, and M. Grundmann, "The E3 Defect in MgxZn1−x O," *J. Electron. Mater.*, vol. 39, no. 5, pp. 584–588, May 2010.

[48] I. Hussain, M. Y. Soomro, N. Bano, O. Nur, and M. Willander, "Systematic study of interface trap and barrier inhomogeneities using I-V-T characteristics of Au/ZnO nanorods Schottky diode," *J. Appl. Phys.*, vol. 113, no. 23, p. 234509, Jun. 2013.

[49] L. Huang and D. Wang, "Barrier inhomogeneities and electronic transport of Pt contacts to relatively highly doped n-type 4H-SiC," *J. Appl. Phys.*, vol. 117, no. 20, p. 204503, May 2015.

[50] N. Yıldırım, K. Ejderha, and A. Turut, "On temperature-dependent experimental I-V and C-V data of Ni/n-GaN Schottky contacts," *J. Appl. Phys.*, vol. 108, no. 11, p. 114506, Dec. 2010.

[51] C. Lu and S. N. Mohammad, "Validity/invalidity of Schottky-Mott rules for Schottky contacts to III-V nitride semiconductor heterostructures," *Appl. Phys. Lett.*, vol. 89, no. 16, p. 162111, Oct. 2006.

[52] M. O. Aboelfotoh, "Electrical characteristics of W-Si(100) Schottky barrier junctions," *J. Appl. Phys.*, vol. 66, no. 1, pp. 262–272, Jul. 1989.

[53] J. Kolník and M. Ožvold, "The Influence of Inversion Surface Layers on the Evaluation of the Interface State Energy Distribution from Schottky-DiodeI–U Characteristics," *Phys. status solidi*, vol. 122, no. 2, pp. 583–588, Dec. 1990.

[54] C. Barret and A. Vapaille, "Interface states in a cleaved metal-silicon junction," *J. Appl. Phys.*, vol. 50, no. 6, pp. 4217–4222, Jun. 1979.

[55] P. Cova and A. Singh, “Temperature dependence of I-V and C-V characteristics of Ni/n-CdF2 Schottky barrier type diodes,” *Solid. State. Electron.*, vol. 33, no. 1, pp. 11–19, Jan. 1990.

[56] S. Hardikar, M. K. Hudait, P. Modak, S. B. Krupanidhi, and N. Padha, “Anomalous current transport in Au/low-doped n-GaAs Schottky barrier diodes at low temperatures,” *Appl. Phys. A Mater. Sci. Process.*, vol. 68, no. 1, pp. 49–55, Jan. 1999.

[57] M. K. Hudait and S. B. Krupanidhi, “Effects of thin oxide in metal–semiconductor and metal–insulator–semiconductor epi-GaAs Schottky diodes,” *Solid. State. Electron.*, vol. 44, no. 6, pp. 1089–1097, Jun. 2000.

[58] A. Singh, “Characterization of interface states at Ni/nCdF2 Schottky barrier type diodes and the effect of CdF2 surface preparation,” *Solid. State. Electron.*, vol. 28, no. 3, pp. 223–232, Mar. 1985.

[59] A. Singh, K. C. Reinhardt, and W. A. Anderson, “Temperature dependence of the electrical characteristics of Yb/ p -InP tunnel metal-insulator-semiconductor junctions,” *J. Appl. Phys.*, vol. 68, no. 7, pp. 3475–3483, Oct. 1990.

[60] A. Turut, M. Saglam, H. Efeoglu, N. Yalcin, M. Yildirim, and B. Abay, “Interpreting the nonideal reverse bias C-V characteristics and importance of the dependence of Schottky barrier height on applied voltage,” *Phys. B Condens. Matter*, vol. 205, no. 1, pp. 41–50, Jan. 1995.

[61] Z. J. Horváth, “Evaluation of the interface state energy distribution from Schottky I - V characteristics,” *J. Appl. Phys.*, vol. 63, no. 3, pp. 976–978, Feb. 1988.

[62] L. R. Dahal, D. Sainju, N. J. Podraza, S. Marsillac, and R. W. Collins, “Real time spectroscopic ellipsometry of Ag/ZnO and Al/ZnO interfaces for back-reflectors in thin film Si:H

photovoltaics," *Thin Solid Films*, vol. 519, no. 9, pp. 2682–2687, Feb. 2011.

[63] M. K. Hudait and S. B. Krupanidhi, "Interface states density distribution in Au/n-GaAs Schottky diodes on n-Ge and n-GaAs substrates," *Mater. Sci. Eng. B*, vol. 87, no. 2, pp. 141–147, Nov. 2001.

[64] Ş. Aydoğan, K. Çınar, H. Asıl, C. Coşkun, and A. Türüt, "Electrical characterization of Au/n-ZnO Schottky contacts on n-Si," *J. Alloys Compd.*, vol. 476, no. 1–2, pp. 913–918, May 2009.

[65] H. Kim, H. Kim, and D.-W. Kim, "Analysis of interface states and series resistance in Ag/m-plane ZnO Schottky diodes," *J. Korean Phys. Soc.*, vol. 63, no. 10, pp. 2034–2038, Nov. 2013.

Chapter 5

Realization of 2DEG in MgZnO/ZnO Heterostructures

5.1 Introduction

In the previous chapters, it has been discussed that due to lower lattice mismatch and higher conduction band offset for MgZnO/ZnO heterostructures, MgZnO/ZnO material system is considered as promising candidate for two-dimensional electron gas (2DEG) density and its applications in heterostructure field-effect transistors (HFETs) [1]–[6]. By alloying MgO in ZnO, the energy band gap and degree of polarization can be fine-tuned in $Mg_xZn_{1-x}O$ [7]. 2DEG formation in single-crystalline MgZnO/ZnO systems has been reported in many published literatures [2], [3], [7], [8], however, report on such 2DEG formation in polycrystalline MgZnO/ZnO system is limited [2], [3]. It is reported that the polarization effect induces large amount of sheet carrier concentration and, thereby, significantly enhances the electrical conductance of high-quality single crystalline or polycrystalline systems. However, such enhancement in conductance is mostly demonstrated by molecular beam epitaxy (MBE) [1], pulsed-laser deposition (PLD) [8], or metal organic vapor phase epitaxy (MOVPE) [9], which are not suitable for low-cost, large-area electronic applications.

This work investigates formation of 2DEG in bilayer and capped MgZnO/ZnO heterostructures, deposited by dual ion beam sputtering (DIBS) system. To the best of our knowledge, there have not been any reports available in the literature regarding an elaborate study on DIBS-grown 2DEG formation in MgZnO/ZnO material system.

5.2 Experimental Details

As shown in Fig. 5.1 (a) and (b), firstly, a ZnO buffer layer of 1 μm thickness was deposited on Si (100) substrate. Subsequently, $Mg_xZn_{1-x}O$ (x = 5, 15, 20, and 30 at. %) barrier layers were deposited to form bilayer heterostructures with constant barrier layer thickness (d) of 30 nm, to study the effect of Mg composition (x) on sheet carrier concentration (n_s). A perfect wurtzite crystalline $Mg_xZn_{1-x}O$ alloy could be formed up to x = 30 at.% [10]. Thus, in our work, the variation of Mg composition is considered up to 30 at.%. Afterwards, a ZnO cap layer of 10 nm thickness (c) was deposited over bilayer heterostructures. To study the effect of variation of thickness of barrier and cap layer on n_s, bilayer heterostructures with different barrier layer thicknesses were grown (d = 5-40 nm and x = 0.3) and capped heterostructures with different ZnO cap layer thicknesses (c = 5-50 nm, d = 30 nm, and x = 0.3) were grown.

Constant substrate temperature of 300 °C, beam voltage of 800 V, deposition ion beam power of 44 W and working pressure inside the DIBS chamber of 2.43×10^{-4} mbar were maintained for all film depositions. The growth environment was oxygen rich (O_2 : Ar = 3:2) with oxygen flow rate of 3 sccm (standard cubic centimeter per minute). The commercially available MgZnO and ZnO sputtering targets were utilized to deposit different layers. Prior to film deposition, in order to remove organic contaminants and native oxide, Si substrate was cleaned, details of which was described in chapter 4 section 4.2. To perform *C-V* characterization, a 100 nm thick and 0.5 mm^2 Pt layer was grown on 30 nm thick MgZnO layer (x = 0.3) in bilayer heterostructure and 10 nm thick ZnO layer (d = 30 nm and x = 0.3) in capped heterostructure, by sputtering a Pt target at room temperature by DC sputtering. Indium ohmic contacts were deposited at 400 °C on the top surface of both the heterostructures. The lateral distance between rectifying (Pt) and ohmic (In) contacts was 1 mm for both heterostructures.

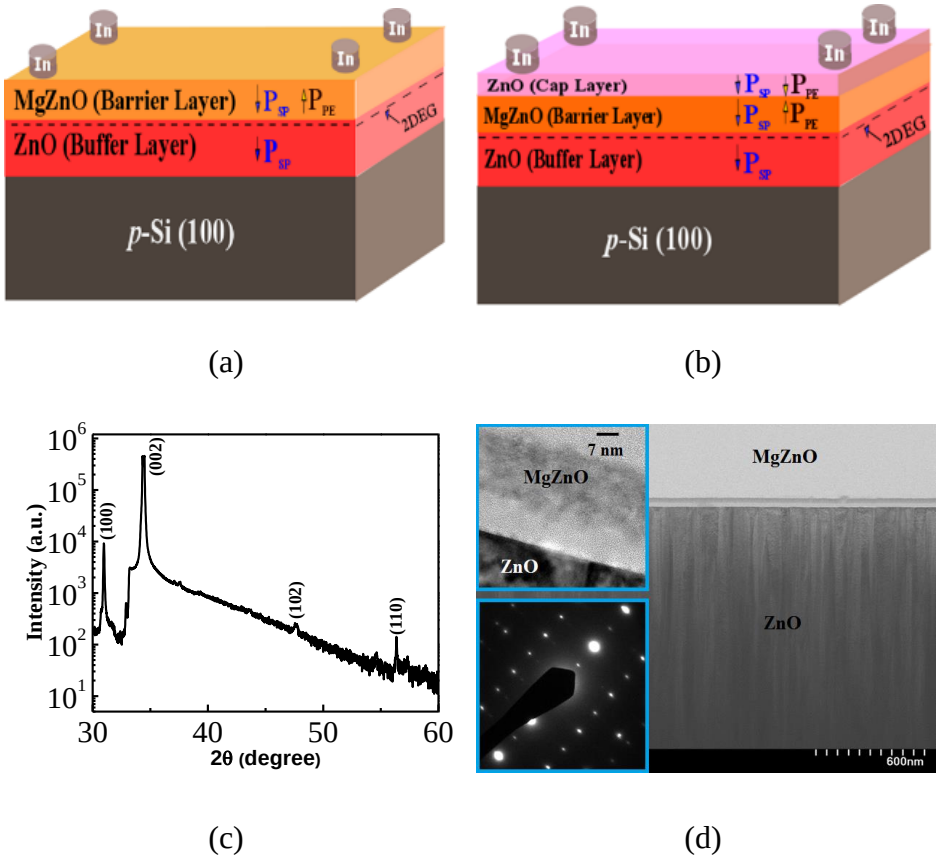

Fig. 5.1: Schematics of (a) bilayer and (b) capped heterostructures with indium contacts on top. Arrow mark shows the direction of spontaneous (P_{SP}) and piezoelectric (P_{PE}) polarization in different layers. (c) XRD pattern of ZnO (buffer) layer on Si (100) substrate. All peaks are indexed according to JCPDS card no. 36-1451. (d) Cross-sectional HRTEM image of $Mg_{0.2}Zn_{0.8}O$/ZnO. Top left inset shows the magnified image of the hetero-interface of $Mg_{0.2}Zn_{0.8}O$/ZnO and bottom left inset shows the corresponding SAED pattern.

Sheet resistivity, sheet carrier concentration, and mobility of the *as-grown* heterostructures were measured by Hall-effect measurement using van der pauw configuration. The crystalline phase and crystal orientations of ZnO (buffer layer) film were determined by X-ray diffraction (XRD) technique using Rigaku Smart Lab system with Cu-Kα radiation (λ = 1.54 Å). The quality of material interface at MgZnO/ZnO was investigated by high-resolution transmission electron microscopy (HRTEM) measurements using TEM: JEOL, JEM-2010; EDX+STEM: Hitachi, HD2300A. The *C-V* measurements were accomplished with a Hioki 3532–50 LCR Hi-Tester

and an Everbeing cryogenic probe station at 300 K and at 1 MHz. The thickness of all the layers were estimated by average deposition rate. The Mg composition in the MgZnO films were investigated by energy dispersive X-Ray (EDX, Zeiss Supra 55) and is found to be approximately same (± 10 % variation) as the Mg composition in the commercially available MgZnO targets.

5.3 Results and Discussion

Fig. 5.1 (c) shows XRD pattern of ZnO film, suggesting the formation of wurtzite crystal which is highly oriented in *c*-axis or <002> crystallographic direction on the Si (100) substrate. Fig. 5.1 (d) shows the cross-sectional HRTEM image for $Mg_{0.2}Zn_{0.8}O$/ZnO heterostructure (d = 30 nm). The image clearly demonstrates the $Mg_{0.2}Zn_{0.8}O$ layer with an abrupt interface to the ZnO layer. HRTEM measurements also confirm high crystal quality of heterojunction interface and flatness of ZnO buffer layer. Inset of Fig. 5.1 (d) shows the selected area electron diffraction (SAED) pattern of the ZnO buffer layer, which could be attributed to the pattern observed from [ī 2 ī 0] axis of wurtzite crystal [11]. This result is consistent with the XRD pattern discussed above, which also confirms the formation of *c*-axis oriented high quality wurtzite crystal of the ZnO buffer layer on the Si (100) substrate. Owing to the high crystalline quality of ZnO buffer layer, 2DEG formation is observed in our DIBS-grown heterostructures [2].

Fig. 5.2 (a) shows n_s of bilayer and capped heterostructures as a function of Mg composition in barrier layer at room temperature (RT). The value of n_s is found to increase with Mg composition for both the heterostructures, attaining values of 1.11×10^{14} cm^{-2} and 1.13×10^{14} cm^{-2} for x = 0.3 for bilayer and capped heterostructure, respectively from ~5×10^{12} cm^{-2} for bare ZnO. The increase in n_s of both the heterostructures are attributed to the creation of a 2DEG at barrier-buffer interface. The monotonic increase in n_s with x in bilayer heterostructure is due to the enhancement in the degree of polarization in barrier layer, which introduces more carriers at the

MgZnO/ZnO interface. The value of n_s in *as-grown* heterostructures is ~10 times larger in magnitude than that grown by radical source MBE [7]. This is probably due to the high defect density [2] or high fixed positive interface states charge, contributing more carriers to the interface. Delagebeaudeuf *et al.* [12] also suggested in their analytical model for the estimation of $n_{s,}$ a provision of interface states charge for defect prone interface. Therefore, interface states charge can be a probable cause for such high n_s in our sputtered samples. Similar observations are reported in MgZnO/ZnO heterostructures grown by radio frequency (RF) sputtering [2], [3], [13] and pulsed laser deposition (PLD) [8].

Further, the slightly enhanced value of n_s in capped heterostructure compared to bilayer heterostructures can be attributed to the piezoelectric polarization in ZnO cap layer which is tensile in nature, unlike that in GaN cap layer [9], [14]. In case of ZnO cap layer in MgZnO/ZnO heterostructure, the cap layer introduces a positive polarization charge at the cap-barrier interface, resulting in a reduced electric field in MgZnO and therefore increases n_s [15]. The orientation of spontaneous (P_{SP}) and piezoelectric (P_{PE}) polarizations in different layers in heterostructures is depicted in Fig. 5.1 (a-b).

The inset of Fig. 5.2 (a) shows the generic conduction energy band diagram of bilayer and capped heterostructures in which φ_b is the bare surface barrier height, E_F is the Fermi energy level with respect to the bottom of the conduction band at the MgZnO/ZnO interface, and ΔE_{C1} and ΔE_{C2} are conduction band offsets at barrier-buffer and cap-barrier interfaces, respectively. As the Mg composition in MgZnO increase the ΔE_{C1} increases for both the heterostructures which deepens the triangular potential well formed at barrier-buffer interface where 2DEG electrons are captured [16], [17]. With the deepening of the triangular potential well the number of 2D density of states involved in the formation of 2DEG increases enhancing the n_s. The depth of triangular potential well is further increased in capped heterostructures due to tensile strain in ZnO cap layer.

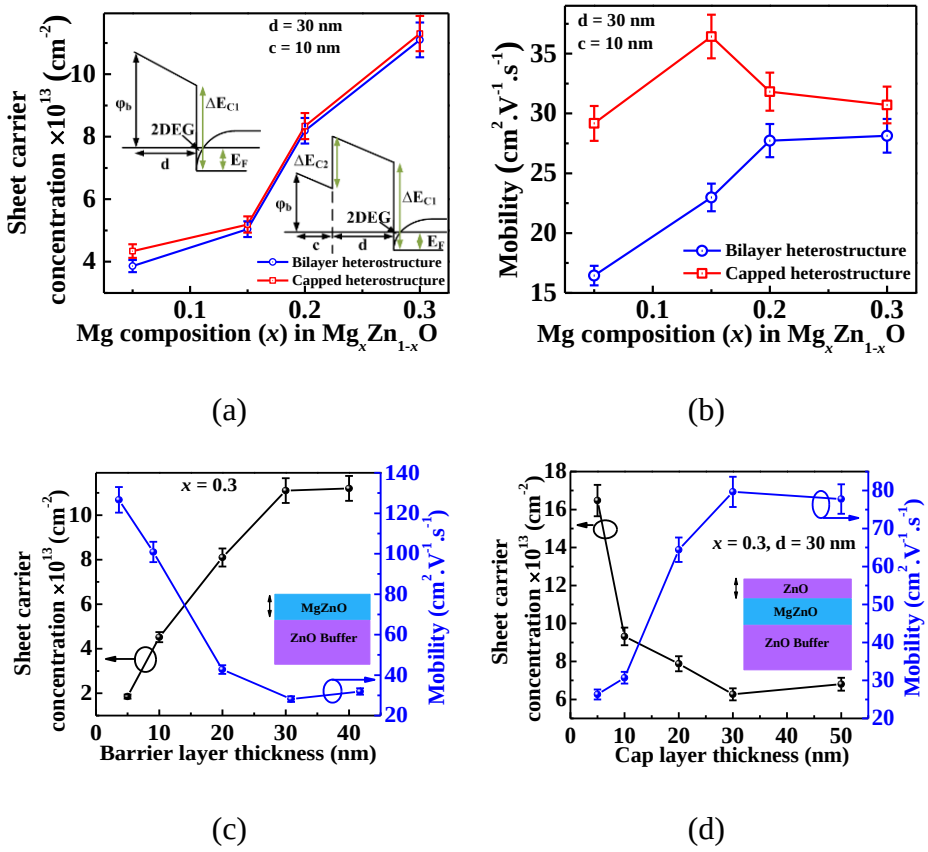

Fig. 5.2: The variation of (a) n_s and (b) mobility in bilayer and capped heterostructures with different Mg composition in barrier layer at room temperature. Insets in figure (a) shows the generic representation of conduction energy band diagrams of bilayer (left) and capped (right) heterostructures. The dependence of n_s and mobility as a function of (c) barrier layer thickness and (d) cap layer thickness. Insets in figures (c) and (d) show the device structure and the double headed arrows indicate the layer whose thickness is varied. The y-error bar depicts the average deviation in Hall measurements.

Fig. 5.2 (b) shows the mobility of charge carriers in 2DEG, in bilayer and capped heterostructures, for different Mg compositions in barrier layer at RT. The value of mobility increases from 16.45 to 28.13 $cm^2.V^{-1}.s^{-1}$ for bilayer heterostructure with the corresponding increase in Mg composition from 5 to 30 at. % in barrier layer as compared to the mobility value of ~1.8 $cm^2.V^{-1}.s^{-1}$ for bare buffer ZnO. The increase in mobility with increase in Mg composition is ascribed to the enhancement of screening effects and

the suppression of alloy scattering due to very large conduction band offset [18], [19] (ΔE_c) similar to that observed for AlGaN/GaN heterostructures [20]. The mobility value in capped heterostructures is slightly higher in magnitude than that observed in case of its bilayer counterpart. Also, the value of mobility of the capped heterostructures show little variation with change in Mg composition. The possible reasons for these are the simultaneous enhancement of screening effect due to increase in Mg composition and suppression of optical phonon scattering due to addition of ZnO cap layer. At the MgZnO/ZnO interface, only first energy sub-band is filled and other higher sub-bands are empty, as shown in our previous simulation work [16]. Thus, only the intra-sub-band scattering within the first sub-band is important in the polar optical phonon scattering mechanism. Within this regime, increase in 2DEG density leads to increase in mobility. This effect can be related to the screening effect of longitudinal optical phonon scattering. It should also be mentioned that screening effects can have significant effect on intra-sub-band polar optical scattering, whereas the inter-sub-band scattering rates are virtually unaffected by screening effects [21].

In general, the value of the 2DEG mobility depends on different scattering mechanisms. The main scattering mechanisms governing the 2DEG mobility are acoustic deformation potential, piezoelectric, polar optic phonon, alloy disorder, interface roughness, dislocation, and remote modulation doping [17], [22]. If a clearer understanding of roles of different scattering mechanisms on mobility is required, that can be done by fitting the experimental value of mobility with the mobility value due to each scattering mechanism. This type of fitting requires detailed analysis and development of analytical model of mobility, which is beyond the scope of present work and thus cannot be discussed here. A comparative analysis of values of n_s and mobility in $Mg_{0.2}Zn_{0.8}O$/ZnO bilayer heterostructures grown by different deposition techniques is presented in Table 5.1. It is observed that value of n_s in our work is comparable to that in heterostructures grown by RF sputtering [2] and PLD [8] and higher than those reported by MBE [7]. The value of mobility of reported here is

comparable to RF sputtering and PLD, however, an order lower as compared to that realized in MBE growth.

Table 5.1 Comparative analysis of sheet carrier concentration and mobility at room temperature for $Mg_{0.2}Zn_{0.8}O/ZnO$ bilayer heterostructure with corresponding reported values in literature.

Parameters	**This work**	**Ref.** [2]	**Ref.** [7]	**Ref.** [8]
Sheet Carrier Concentration $\times 10^{13}$ (cm^{-2})	8.19	8.68	0.43	11.7
Mobility ($cm^2/V.s$)	27.73	26.68	249.01	32.14
Deposition Technique	DIBS	RF sputtering	MBE	PLD

Fig. 5.2 (c) shows the variation of n_s and mobility as a function of barrier layer thickness for x = 0.3 in bilayer heterostructure. The value of n_s increases with increasing barrier layer thickness from 1.85×10^{13} cm^{-2} at 5 nm to 1.11×10^{14} cm^{-2} at 30 nm and saturates beyond 30 nm. The trend of variation of mobility follows the inverse relationship with that of n_s because as the n_s increases, the cumulative scattering increases which reduces the mobility. The saturation behavior of n_s with barrier layer thickness is due to the presence of ionized donor like surface states present at the top surface of MgZnO layer for the formation of 2DEG [7], [23]. Similar trends were observed for MgZnO/ZnO system by Tampo *et al* [7] and for AlGaN/GaN heterostructure by Ibbetson *et al* [23]. Fig. 5.2 (d) shows the change in n_s and mobility as a function of ZnO cap layer thickness for a fixed barrier layer x = 0.3 and d = 30 nm in capped heterostructures. The value of n_s decreases with increase of cap layer thickness from 1.65×10^{14} cm^{-2} at 5 nm to 6.80×10^{13} cm^{-2} for 50 nm thick ZnO cap layer. Mobility increases from 25 $cm^2.V^{-1}.s^{-1}$ at 5 nm to 78 $cm^2.V^{-1}.s^{-1}$ at 50 nm due to suppressed scattering of carriers with decreased density. The decrease in n_s with cap layer thickness might be due to the reduction of piezoelectric polarization

in cap layer with increasing cap layer thickness [16]. Similar reduction in n_s is also observed in GaN/AlGaN/GaN material system [15], [21].

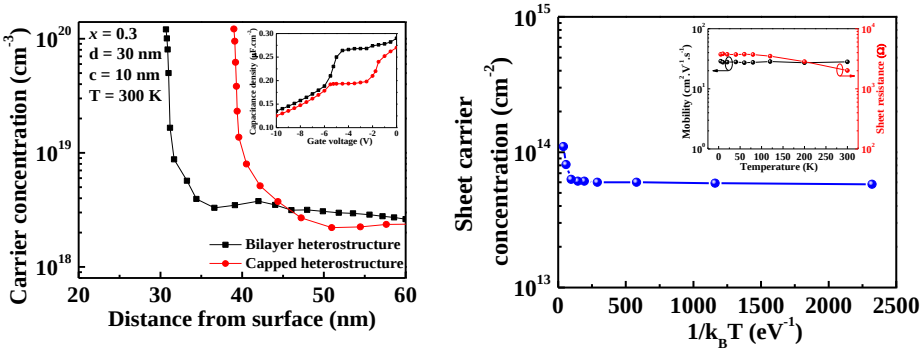

(a) (b)

Fig. 5.3: (a) C-V measurement for MgZnO/ZnO and ZnO/MgZnO/ZnO heterostructures. The inset shows the C-V measurement data for both heterostructures. (b) Temperature dependence of sheet carrier concentration of $Mg_{0.3}Zn_{0.7}O$/ZnO heterostructure with $Mg_{0.3}Zn_{0.7}O$ barrier layer thickness of ~30 nm. The inset shows the temperature dependence of Hall mobility and sheet resistance.

Fig. 5.3 (a) shows *C-V* measurement for a bilayer and capped heterostructures, with x = 0.3, d = 30 nm, and c = 10 nm. The carrier concentrations in MgZnO barrier layer was estimated to be ~2×10^{18} cm^{-3}. The peak in carrier concentration at 30 nm for bilayer heterostructure and 40 nm for capped heterostructure from the barrier layer surface and cap layer surface, respectively confirms the confinement of electrons at the barrier-buffer interface and therefore, suggest formation of 2DEG. The equation used for the extraction of carrier concentration ($N_{C\text{-}V}$) from *C-V* measurement is as follows [24]:

$$N_{C-V}(W) = \frac{2}{qk_s\epsilon_0 A^2}\left[\frac{-1}{d(1/C^2)/dV}\right] \qquad (5.1)$$

The depth dependency of $N_{C\text{-}V}$ can be determined from the measured capacitance, C

$$W = \frac{k_s \epsilon_0 A}{C} \tag{5.2}$$

where W, k_s, ϵ_0, A, q, and V are distance from surface, relative dielectric constant, permittivity of free space, area of Schottky contact, elementary charge, and applied voltage, respectively. A similar method of extraction for $N_{C\text{-}V}$ is also used for AlGaN/GaN heterostructure [25] and inverse MgZnO/ZnO heterostructure [26]. The carrier concentration was calculated assuming the relative dielectric constants of MgZnO and ZnO to be the same at 8.75 [9].

To further validate that the charges are indeed two-dimensional, we perform low temperature Hall measurement to obtain variation in n_s, mobility, and sheet resistance as a function of temperature. Fig. 5.3 (b) shows the temperature dependence of n_s. It can be observed that the n_s is almost constant in the entire temperature range from 5 K to 300 K. More data points at lower temperature range are taken to check whether the carriers are frozen. The carriers are observed not to freeze at lower temperature indicating that the carriers have actually originated from the MgZnO/ZnO interface and not from thermal activation of bulk donors of ZnO and MgZnO [3], [7], [27], [28], which confirms the formation of 2DEG. A slight increase in n_s beyond 120 K, however, is due to the contribution of some thermally activated shallow donors in bulk ZnO and MgZnO layers. Similar increase of n_s is also reported for MgZnO/ZnO heterostructures [27], [29]. The possible shallow donors in our samples may be zinc interstitial (Zn_i), as reported by Look *et al* [30] having activation energy of about 25-30 meV in ZnO or Hydrogen as suggested elsewhere [31]. The inset of Fig. 5.3 (b) shows the temperature dependence of sheet resistance (R_s) and mobility. As observed in the figure, the sheet resistance changes from 3.8 KΩ to 2 KΩ for the corresponding change of temperature from 5 to 300 K. At low temperatures (T < 120 K), the carrier

concentration and mobility are constant which result in almost constant sheet resistance implying a metal-like behavior [28]. The observation of metal-like behavior further confirms the formation 2DEG. In our case, the resistance slightly decreases with increase in temperature because at higher temperature apart from 2DEG, some thermally excited electrons also participate in the conduction as confirmed in the above discussion. Our sample also shows a temperature independent trend on carrier mobility, which is related to surface roughness scattering of 2DEG at MgZnO/ZnO interface [32].

5.4 Conclusion

ZnO based 2DEG yielding heterostructures, with MgZnO as barrier layer, were fabricated by DIBS system and probed for variation of n_s and mobility as a function of Mg composition in barrier layer, barrier layer thickness, and cap layer thickness. XRD and HRTEM results show high crystallinity of the buffer ZnO and flat and uniform heterointerface, which is essential for the formation of 2DEG. The values of n_s is observed to increase with the corresponding rise in Mg composition for both bilayer and capped structures. At $x = 0.3$, for bilayer structure, the values of n_s and mobility are 1.11×10^{14} cm^{-2} and 28.13 $cm^2/V.s$, respectively at RT. The observed n_s saturates at higher barrier layer thickness for bilayer heterostructure. The effect of variation in cap layer thickness suggests enhanced n_s for thinner cap layer thickness (1.65×10^{14} cm^{-2}) which decreases and saturates at higher cap layer thickness. The carrier profiling done by *C-V* measurement indicates high carrier concentration (~10^{20} cm^{-3}) at 30 nm from top surface for bilayer heterostructure, which is the barrier-buffer interface indicating the confinement of charge carriers at barrier-buffer interface. The observation of *C-V* measurements and temperature dependent Hall measurement confirm the formation of 2DEG in the heterostructures. Results of this study suggests DIBS system as one of the possible options to fabricate cost-effective and large area MgZnO/ZnO based HEMTs.

5.5 References

[1] H. Tampo, H. Shibata, K. Matsubara, A. Yamada, P. Fons, S. Niki, M. Yamagata, and H. Kanie, "Two-dimensional electron gas in Zn polar ZnMgO/ZnO heterostructures grown by radical source molecular beam epitaxy," *Appl. Phys. Lett.*, vol. 89, no. 13, p. 132113, Sep. 2006.

[2] H.-A. Chin, I.-C. Cheng, C.-I. Huang, Y.-R. Wu, W.-S. Lu, W.-L. Lee, J. Z. Chen, K.-C. Chiu, and T.-S. Lin, "Two dimensional electron gases in polycrystalline MgZnO/ZnO heterostructures grown by rf-sputtering process," *J. Appl. Phys.*, vol. 108, no. 5, p. 54503, Sep. 2010.

[3] H.-A. Chin, I.-C. Cheng, C.-K. Li, Y.-R. Wu, J. Z. Chen, W.-S. Lu, and W.-L. Lee, "Electrical properties of modulation-doped rf-sputtered polycrystalline MgZnO/ZnO heterostructures," *J. Phys. D. Appl. Phys.*, vol. 44, no. 45, p. 455101, Nov. 2011.

[4] A. Thongnum, V. Sa-yakanit, and U. Pinsook, "Two-dimensional electron transport in MgZnO/ZnO heterostructures: role of interface roughness," *J. Phys. D. Appl. Phys.*, vol. 44, no. 32, p. 325109, Aug. 2011.

[5] S. Sasa, T. Maitani, Y. Furuya, T. Amano, K. Koike, M. Yano, and M. Inoue, "Microwave performance of ZnO/ZnMgO heterostructure field effect transistors," *Phys. status solidi*, vol. 208, no. 2, pp. 449–452, Feb. 2011.

[6] B.-S. Wang, Y.-S. Li, and I.-C. Cheng, "Mobility Enhancement in RF-Sputtered MgZnO/ZnO Heterostructure Thin-Film Transistors," *IEEE Trans. Electron Devices*, vol. 63, no. 4, pp. 1545–1549, Apr. 2016.

[7] H. Tampo, H. Shibata, K. Maejima, A. Yamada, K. Matsubara, P.

Fons, S. Kashiwaya, S. Niki, Y. Chiba, T. Wakamatsu, and H. Kanie, "Polarization-induced two-dimensional electron gases in ZnMgO/ZnO heterostructures," *Appl. Phys. Lett.*, vol. 93, no. 20, p. 202104, Nov. 2008.

[8] A. K. Das, P. Misra, R. S. Ajimsha, M. P. Joshi, and L. M. Kukreja, "Effects of electron interference on temperature dependent transport properties of two dimensional electron gas at MgZnO/ZnO interfaces," *Appl. Phys. Lett.*, vol. 107, no. 10, p. 102104, Sep. 2015.

[9] J. D. Ye, S. Pannirselvam, S. T. Lim, J. F. Bi, X. W. Sun, G. Q. Lo, and K. L. Teo, "Two-dimensional electron gas in Zn-polar ZnMgO/ZnO heterostructure grown by metal-organic vapor phase epitaxy," *Appl. Phys. Lett.*, vol. 97, no. 11, p. 111908, Sep. 2010.

[10] S. Choopun, R. D. Vispute, W. Yang, R. P. Sharma, T. Venkatesan, and H. Shen, "Realization of band gap above 5.0 eV in metastable cubic-phase MgxZn1−xO alloy films," *Appl. Phys. Lett.*, vol. 80, no. 9, pp. 1529–1531, Mar. 2002.

[11] M. T. Htay, Y. Tani, Y. Hashimoto, and K. Ito, "Synthesis of optical quality ZnO nanowires utilizing ultrasonic spray pyrolysis," *J. Mater. Sci. Mater. Electron.*, vol. 20, no. S1, pp. 341–345, Jan. 2009.

[12] D. Delagebeaudeuf and N. T. Linh, "Metal-(n) AlGaAs-GaAs two-dimensional electron gas FET," *IEEE Trans. Electron Devices*, vol. 29, no. 6, pp. 955–960, Jun. 1982.

[13] I.-C. Cheng, B.-S. Wang, H.-H. Hou, and J.-Z. Chen, "MgZnO/ZnO Heterostructure Field-Effect Transistors Fabricated by RF-Sputtering," *ECS Trans.*, vol. 50, no. 8, pp. 83–93, Mar. 2013.

[14] O. Ambacher, B. Foutz, J. Smart, J. R. Shealy, N. G. Weimann, K. Chu, M. Murphy, A. J. Sierakowski, W. J. Schaff, L. F. Eastman, R. Dimitrov, A. Mitchell, and M. Stutzmann, "Two dimensional electron gases induced by spontaneous and piezoelectric polarization

in undoped and doped AlGaN/GaN heterostructures," *J. Appl. Phys.*, vol. 87, no. 1, pp. 334–344, Jan. 2000.

[15] S. Heikman, S. Keller, Y. Wu, J. S. Speck, S. P. DenBaars, and U. K. Mishra, "Polarization effects in AlGaN/GaN and GaN/AlGaN/GaN heterostructures," *J. Appl. Phys.*, vol. 93, no. 12, pp. 10114–10118, Jun. 2003.

[16] R. Singh, M. A. Khan, S. Mukherjee, and A. Kranti, "Analytical Model for 2DEG Density in Graded MgZnO/ZnO Heterostructures With Cap Layer," *IEEE Trans. Electron Devices*, vol. 64, no. 9, pp. 3661–3667, Sep. 2017.

[17] M. A. Khan, R. Singh, S. Mukherjee, and A. Kranti, "Buffer Layer Engineering for High ($\geq 10^{13}$ cm^{-2}) 2-DEG Density in ZnO-Based Heterostructures," *IEEE Trans. Electron Devices*, vol. 64, no. 3, pp. 1015–1019, Mar. 2017.

[18] A. Ohtomo, M. Kawasaki, I. Ohkubo, H. Koinuma, T. Yasuda, and Y. Segawa, "Structure and optical properties of ZnO/Mg0.2Zn0.8O superlattices," *Appl. Phys. Lett.*, vol. 75, no. 7, pp. 980–982, Aug. 1999.

[19] H. Tampo, H. Shibata, K. Maejima, A. Yamada, K. Matsubara, P. Fons, S. Niki, T. Tainaka, Y. Chiba, and H. Kanie, "Strong excitonic transition of Zn1−xMgxO alloy," *Appl. Phys. Lett.*, vol. 91, no. 26, p. 261907, Dec. 2007.

[20] O. Ambacher, J. Smart, J. R. Shealy, N. G. Weimann, K. Chu, M. Murphy, W. J. Schaff, L. F. Eastman, R. Dimitrov, L. Wittmer, M. Stutzmann, W. Rieger, and J. Hilsenbeck, "Two-dimensional electron gases induced by spontaneous and piezoelectric polarization charges in N- and Ga-face AlGaN/GaN heterostructures," *J. Appl. Phys.*, vol. 85, no. 6, pp. 3222–3233, Mar. 1999.

[21] A. Asgari, M. Kalafi, and L. Faraone, "The effects of GaN capping

layer thickness on two-dimensional electron mobility in GaN/AlGaN/GaN heterostructures," *Phys. E Low-dimensional Syst. Nanostructures*, vol. 25, no. 4, pp. 431–437, Jan. 2005.

[22] J. Zhang, Y. Hao, J. Zhang, and J. Ni, "The mobility of two-dimensional electron gas in AlGaN/GaN heterostructures with varied Al content," *Sci. China Ser. F Inf. Sci.*, vol. 51, no. 6, pp. 780–789, Jun. 2008.

[23] J. P. Ibbetson, P. T. Fini, K. D. Ness, S. P. DenBaars, J. S. Speck, and U. K. Mishra, "Polarization effects, surface states, and the source of electrons in AlGaN/GaN heterostructure field effect transistors," *Appl. Phys. Lett.*, vol. 77, no. 2, pp. 250–252, Jul. 2000.

[24] P. A. Barnes, "Capacitance-Voltage (C-V) Characterization of Semiconductors," in *Characterization of Materials*, Hoboken, NJ, USA: John Wiley & Sons, Inc., 2012.

[25] D. J. As, A. Zado, Q. Y. Wei, T. Li, J. Y. Huang, and F. A. Ponce, "Capacitance Voltage Characteristics and Electron Holography on Cubic AlGaN/GaN Heterojunctions," *Jpn. J. Appl. Phys.*, vol. 52, no. 8S, p. 08JN04, Aug. 2013.

[26] M. Nakano, A. Tsukazaki, K. Ueno, R. Y. Gunji, A. Ohtomo, T. Fukumura, and M. Kawasaki, "Spatial distribution of two-dimensional electron gas in a ZnO/Mg0.2Zn0.8O heterostructure probed with a conducting polymer Schottky contact," *Appl. Phys. Lett.*, vol. 96, no. 5, p. 52116, Feb. 2010.

[27] K. Ding, M. B. Ullah, V. Avrutin, Ü. Özgür, and H. Morkoç, "Investigation of high density two-dimensional electron gas in Zn-polar BeMgZnO/ZnO heterostructures," *Appl. Phys. Lett.*, vol. 111, no. 18, p. 182101, Oct. 2017.

[28] K. T. Roro, G. H. Kassier, J. K. Dangbegnon, S. Sivaraya, J. E. Westraadt, J. H. Neethling, A. W. R. Leitch, and J. R. Botha,

"Temperature-dependent Hall effect studies of ZnO thin films grown by metalorganic chemical vapour deposition," *Semicond. Sci. Technol.*, vol. 23, no. 5, p. 55021, May 2008.

[29] A. Tsukazaki, A. Ohtomo, T. Kita, Y. Ohno, H. Ohno, and M. Kawasaki, "Quantum Hall Effect in Polar Oxide Heterostructures," *Science (80-.).*, vol. 315, no. 5817, pp. 1388–1391, Mar. 2007.

[30] D. C. Look, J. W. Hemsky, and J. R. Sizelove, "Residual Native Shallow Donor in ZnO," *Phys. Rev. Lett.*, vol. 82, no. 12, pp. 2552–2555, Mar. 1999.

[31] C. H. Seager and S. M. Myers, "Quantitative comparisons of dissolved hydrogen density and the electrical and optical properties of ZnO," *J. Appl. Phys.*, vol. 94, no. 5, pp. 2888–2894, Sep. 2003.

[32] R. Gottinger, A. Gold, G. Abstreiter, G. Weimann, and W. Schlapp, "Interface Roughness Scattering and Electron Mobilities in Thin GaAs Quantum Wells," *Europhys. Lett.*, vol. 6, no. 2, pp. 183–188, May 1988.

Chapter 6

Role of Surface States and Interface Charges in 2DEG in Sputtered ZnO Heterostructures

6.1 Introduction

As discussed in the previous chapters, MgZnO/ZnO based heterostructures show the formation of two-dimensional electron gas at the MgZnO/ZnO heterointerface due to spontaneous and piezoelectric polarization [1]. The two-dimensional electron gas (2DEG) density in MgZnO/ZnO heterostructure can be obtained by different growth mechanisms such as epitaxial and sputtering. However, the 2DEG density is nearly an order of magnitude different in heterostructure grown by sputtering [2]–[4] and epitaxial [1], [5], [6] techniques. Therefore, the contributing factors to the source of electrons in 2DEG in MgZnO/ZnO heterostructure in both growth techniques should be different and require insightful analysis. Ibbetson *et al.*, suggested the presence of surface donor states to be the predominant origin of electrons in 2DEG for AlGaN/GaN heterostructures [7], which might also hold for MgZnO/ZnO heterostructures grown by molecular beam epitaxy (MBE). However, an exact physical mechanism of formation of 2DEG, its understanding and contributions of different affecting parameters is still lacking in literature mainly for sputtered deposited MgZnO/ZnO heterostructure [7], [8].

The difference in the values of 2DEG by sputtering and epitaxial growth suggests that the formation of 2DEG is affected by the introduction of an additional source of electrons in case of growth by sputtering. In order to explain the source of electrons in the 2DEG in MgZnO/ZnO heterostructures grown by different techniques, the roles of surface states and interface charges in MgZnO/ZnO heterostructure are investigated using an insightful analysis based on electrostatic neutrality across barrier

and buffer layer. The proposed theory is compared with simulations to account for different contributing factors and the effect of each such factor on 2DEG density. The analysis is further verified by comparing the results with published experimental data for epitaxial [1] and sputtering [3] growth mechanisms. This work improves the understanding of roles of donor and acceptor states and provides an explanation for an order of magnitude high 2DEG density in sputtered heterostructures through the contribution of interface charges. This understanding is essential for the estimation of 2DEG under different growth mechanisms, which is crucial to the performance of HEMTs.

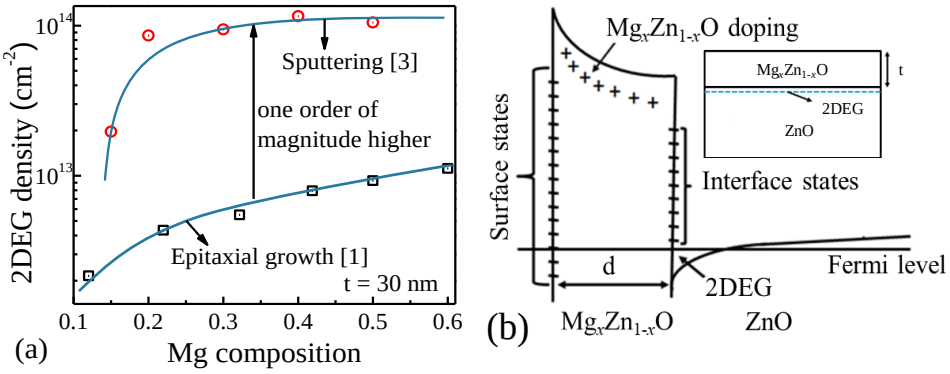

Fig. 6.1: (a) 2DEG density varying with Mg composition for sputtering [3] *and epitaxially* [1] *grown MgZnO/ZnO heterostructures. (b) Schematic conduction band diagram for MgZnO/ZnO heterostructure showing the various space charge components and inset shows the device schematic.*

6.2 Simulations

Fig. 6.1 (a) shows the experimental 2DEG density in MgZnO/ZnO heterostructure, available in literature [1], [3], grown by MBE [1] and radio frequency (RF) sputtering [3] techniques, with varying Mg composition (x) in MgZnO barrier layer at zero bias. Therefore, all the investigation done in this work are at zero bias. For a 30 nm barrier layer thickness (t), the value of 2DEG density in sputtering grown MgZnO/ZnO heterostructures

is nearly one order of magnitude higher than that grown by MBE. Ibbetson *et al.*, [7] suggested that the surface donor-like states to be the origin of 2DEG electrons, the same mechanism is not appropriate to predict an order of magnitude higher 2DEG values in RF-sputtered samples which requires careful reconsideration of the contributing factors and the distinct roles of each for high values of 2DEG density. Chin *et al.* [3] has suggested that high values of 2DEG density (~10^{14} cm^{-2}) in MgZnO/ZnO samples is due to high defect density in their samples which contribute more carriers to the interface, and thus increases 2DEG density.

As shown in the schematic conduction band diagram (Fig. 6.1 (b)) of MgZnO/ZnO heterostructure, the space charge components consists of (i) negative charge due to electrons in 2DEG at the heterointerface (qn_s, where q is the charge of electron and n_s is the 2DEG density), (ii) polarization induced sheet charges in barrier and buffer layer, (iii) integrated sheet charge ($\sigma_{integrated}$) due to ionized bulk donors in MgZnO (σ_{MgZnO}) and ZnO (σ_{ZnO}) layers, (iv) charge due to ionized surface states ($\sigma_{surface}$), including donors (N_D) and acceptors (N_A) surface states (here N_D and N_A are not doping densities but surface state densities), and (v) charges due to formation of interface states at the barrier-buffer interface ($\sigma_{interface}$). In this study $\sigma_{interface}$ is considered as fixed charge as the study done in this work is for zero bias conditions. In case of (0001) oriented MgZnO/ZnO heterostructure, the polarization difference created at the heterointerface is positive. This polarization difference at the heterointerface creates an electric field, which attracts free electrons present in the heterostructure to nullify the positive polarization charge difference at the heterointerface. If the deposition is not single crystalline i.e. defective, then there is possibility for fixed trap charges in barrier layer, which will enhance or decrease the electric field created by polarization difference depending on positive or negative nature of fixed trap charges. The electrons in 2DEG thus can be obtained as

$$qn_s = \sigma_{surface} + \sigma_{interface} + \sigma_{integrated} \qquad (6.1)$$

The device structure has been analyzed through ATLAS simulation tool [9]. In order to ensure accuracy of physics based simulations, parameters such as band gap energy, spontaneous polarization coefficients, lattice parameters, elastic stiffness constants, piezoelectric constants, and relative permittivity, as outlined in Table 3.1 were used in simulation of MgZnO/ZnO heterostructure. Bandgap narrowing model is included to account for the variation of band gap with temperature, Fermi-Dirac [10] statistics and Shockley-Read-Hall (SRH) Recombination [11], [12] model has been included in the simulations. The models of carrier transport are also taken into account [13], [14].

6.3 Results and Discussion

As per the existing theory valid for epitaxially grown heterostructures [8], electrons which compensate the positive polarization charge difference, come from integrated sheet charges from bulk donors ($\sigma_{integrated}$) and ionized surface states ($\sigma_{surface}$) for single crystalline MgZnO/ZnO system. The $\sigma_{interface}$ is neglected because its value is very small for single crystalline systems [15]. Therefore, the expression of n_s for single crystalline epitaxially grown heterostructures can be expressed as

$$qn_s = \sigma_{surface} + \sigma_{integrated} \tag{6.2}$$

Fig. 6.2 (a) shows the comparison of epitaxially grown experimental results [1] of 2DEG density with our simulation for varying barrier layer thickness at fixed Mg composition of x = 0.37. It is observed that the surface donor and acceptor densities combined can attain the experimental 2DEG density values. The ionized surface donor states density of 7×10^{12} cm^{-2} at 0.8 eV energy level below barrier layer conduction band minima along with surface acceptor states density of 10^{13} cm^{-2} at 0.2 eV above barrier layer valence band maxima, are used in the simulation. These values of surface donor and acceptor energy level as predicted in our work agrees very well with the published results of Tampo *et al.* [16] and Park *et al.* [17],

respectively. The value of N_D as predicted in our work is also in reasonable agreement with experimentally obtained value of ~8×10^{12} cm^{-2} by Tampo *et al.* [16] at $x = 0.42$. The value of surface acceptor states density of 10^{13} cm^{-2} is used to obtain a good fit in the simulations, and is also in the range of reported values for surface acceptor states density [18]. The value of σ_{MgZnO} is ~ 10^{17} cm^{-3} and σ_{ZnO} is ~ 10^{16} cm^{-3} is used throughout in the simulations unless its changed value is explicitly mentioned. Our simulated results as shown in Fig. 6.2 (a) suggests that the existing theory [7] for the source of 2DEG electrons in single crystalline AlGaN/GaN system partially holds true for single crystalline MgZnO/ZnO system. Published results have also reported the presence of both surface donor and acceptor states in ZnO surface [18], [19]. It can also be seen in Fig. 6.2 (a) that as the surface acceptor states density increases, 2DEG density value decreases because it pulls the Fermi energy level down and decreases the triangular potential well depth, which is formed at MgZnO/ZnO heterointerface. It is also to be noted that without surface acceptor states, the simulated 2DEG density values are higher than the experimental values, and vary from 8.56 $\times$ 10^{12} cm^{-2} to 8.73 $\times$ 10^{12} cm^{-2} for corresponding change in thickness of MgZnO layer from 3 nm to 20 nm, not shown in the graph.

Fig. 6.2 (b) shows the comparison of 2DEG density in experimental results of RF-sputtering [3] with our simulated 2DEG density, with and without interface charges for varying Mg composition at fixed barrier layer thickness of 30 nm. Our simulated 2DEG density is unable to attain the experimental 2DEG density for lower Mg composition of $x = 0.15$. This may be due to sudden decrease in interface charges at $x = 0.15$ onwards lower Mg composition because of decrease in lattice mismatch between barrier and buffer layer [20] which reduces the chance of formation of high interface charges. Another probable reason for this sudden transition may be that the polarization field difference for the $Mg_{0.15}Zn_{0.85}O$/ZnO interface in RF sputtered film is weaker than those with higher Mg content. The carriers induced by the polarization field in this case may not be sufficient to passivate the defects [21]. From Fig. 6.2 (b) the following are evident:

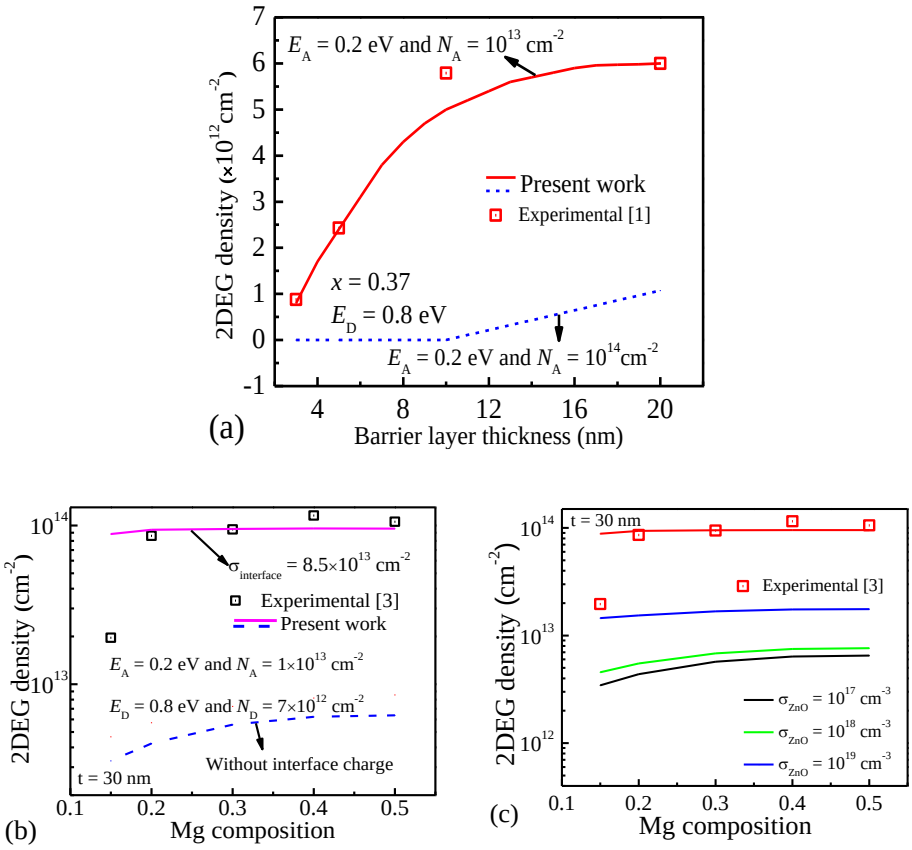

Fig. 6.2: Comparison of simulated and experimental 2DEG density grown by (a) MBE, and (b) RF-sputtering. (c) Simulated 2DEG density for different doping density in ZnO buffer layer showing that higher values of 2DEG density are least likely to be due to the doping of buffer layer.

i) The surface donor and acceptor states alone cannot attain the experimentally obtained 2DEG values in sputtered heterostructures [3]. The experimental values as shown in Fig. 6.2 (b) are one order of magnitude higher than the simulated values achieved only by surface donor and acceptor states, and undoped barrier and buffer layer. Therefore, the surface donor and acceptor states are not the sole source of 2DEG electrons in sputtered ZnO heterostructures.

ii) The other possible source of 2DEG electrons is the integrated sheet charges in barrier and buffer layer due to doping. However, these charges were not able to achieve the experimental values even when the doping density in buffer ZnO layer was increased excessively (> 10^{19} cm^{-3}), while keeping the constant doping in barrier MgZnO layer as 10^{17} cm^{-3}, as can be seen in Fig. 6.2 (c).

iii) Experimental values of 2DEG density in sputtered MgZnO/ZnO heterostructures [3] were only achieved when another source of 2DEG electrons was considered in the analysis. As the surface of ZnO is generally not very stable due to presence of oxygen vacancies [22] and hydrogen adsorption [23], it is highly likely that the interface of sputtered MgZnO/ZnO has defect states which contribute towards an enhanced 2DEG density [3]. The defect density is high in sputtered samples, which leads to high trapped charges, and therefore, higher values of effective interface charges [3].

This would imply that for sputtering grown samples the charge balance equation is same as Eq. (6.1).

While the exact mechanism for the formation of high defect density in MgZnO/ZnO samples is still under research for sputtered deposited samples, our work has shown that it has significant impact on the formation of 2DEG in sputtered MgZnO/ZnO heterostructure [17], [24]. In MBE, the deposition is nearly defect free and, therefore, there are negligible charges at MgZnO/ZnO interface [15].

Fig. 6.3 (a) shows that the conduction band for epitaxially grown heterostructures (without interface charges), that suggests an abrupt change at the interface and the triangular potential well is formed only in buffer layer side. This is because the source of 2DEG electrons, to be collected in the triangular potential well, is surface states which pin the Fermi energy level at a specific energy level below conduction band minima i.e. fixes the position of conduction band minima as well. In sputtering grown heterostructure (with interface charges, ~10^{13} cm^{-2}), we observe that the

conduction band shifts downwards, thus, more two-dimensional density of states are available for 2DEG. This is due to the defect generated charge carriers [25] that pull down the conduction band minima further below in buffer layer, until the positive polarization difference at the barrier-buffer interface is completely abolished. For further increment of positive interface charges [26], the induced free carriers accumulate at the barrier-buffer interface under additional positive columbic attraction and since, the band-offset is below the Fermi energy level, the free carriers are accumulated on the barrier side as well. This further increases the depth of potential well, and hence, 2DEG increases.

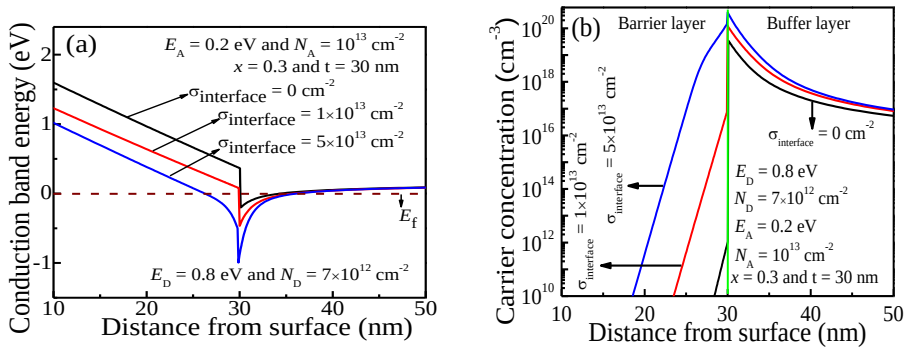

Fig. 6.3: (a) Conduction energy band diagram of MgZnO/ZnO heterostructure for without interface charges and with interface charges. (b) Charge distribution profile of 2DEG across MgZnO/ZnO heterostructure for without interface charges and with interface charges.

Fig. 6.3(b) shows the charge distribution profile of 2DEG across MgZnO/ZnO heterostructure for a 30 nm barrier layer thickness over buffer layer ZnO for without interface charges and with interface charges. The peak in electron carrier concentration at 30 nm from surface, in Fig. 6.3 (b), shows the confinement of 2-D electrons at the MgZnO/ZnO heterointerface. It can be noticed that the electron concentration in barrier layer is significantly lower than the bulk electron concentration (in buffer layer), suggesting the depletion of barrier electrons in the formation of 2DEG.

6.4 Conclusion

The epitaxially grown MgZnO/ZnO heterostructures show a non-negligible role of acceptor states towards the formation of 2DEG density. The surface donor density shows a causal-effect relationship in presence of acceptor states. In contrast, the 2DEG density in sputtered MgZnO/ZnO samples is an order high, and exceeds the barrier-buffer polarization difference limit. This is due to the interface states present at the MgZnO/ZnO interface due to sputtering growth technique and leads to formation of interface trap charges which contribute towards enhancement of 2DEG density. This work improves the understanding of underlying physical mechanisms and contributing factors in the formation of 2DEG in MgZnO/ZnO heterostructure fabricated by different growth mechanisms.

6.5 References

[1] H. Tampo, H. Shibata, K. Maejima, A. Yamada, K. Matsubara, P. Fons, S. Kashiwaya, S. Niki, Y. Chiba, T. Wakamatsu, and H. Kanie, "Polarization-induced two-dimensional electron gases in ZnMgO/ZnO heterostructures," *Appl. Phys. Lett.*, vol. 93, no. 20, p. 202104, Nov. 2008.

[2] I.-C. Cheng, B.-S. Wang, H.-H. Hou, and J.-Z. Chen, "MgZnO/ZnO Heterostructure Field-Effect Transistors Fabricated by RF-Sputtering," *ECS Trans.*, vol. 50, no. 8, pp. 83–93, Mar. 2013.

[3] H.-A. Chin, I.-C. Cheng, C.-I. Huang, Y.-R. Wu, W.-S. Lu, W.-L. Lee, J. Z. Chen, K.-C. Chiu, and T.-S. Lin, "Two dimensional electron gases in polycrystalline MgZnO/ZnO heterostructures grown by rf-sputtering process," *J. Appl. Phys.*, vol. 108, no. 5, p. 54503, Sep. 2010.

[4] H.-A. Chin, I.-C. Cheng, C.-K. Li, Y.-R. Wu, J. Z. Chen, W.-S. Lu,

and W.-L. Lee, “Electrical properties of modulation-doped rf-sputtered polycrystalline MgZnO/ZnO heterostructures,” *J. Phys. D. Appl. Phys.*, vol. 44, no. 45, p. 455101, Nov. 2011.

[5] H. Tampo, H. Shibata, K. Matsubara, A. Yamada, P. Fons, S. Niki, M. Yamagata, and H. Kanie, “Two-dimensional electron gas in Zn polar ZnMgO/ZnO heterostructures grown by radical source molecular beam epitaxy,” *Appl. Phys. Lett.*, vol. 89, no. 13, p. 132113, Sep. 2006.

[6] H. Tampo, K. Matsubara, A. Yamada, H. Shibata, P. Fons, M. Yamagata, H. Kanie, and S. Niki, “High electron mobility Zn polar ZnMgO/ZnO heterostructures grown by molecular beam epitaxy,” *J. Cryst. Growth*, vol. 301–302, no. SPEC. ISS., pp. 358–361, Apr. 2007.

[7] J. P. Ibbetson, P. T. Fini, K. D. Ness, S. P. DenBaars, J. S. Speck, and U. K. Mishra, “Polarization effects, surface states, and the source of electrons in AlGaN/GaN heterostructure field effect transistors,” *Appl. Phys. Lett.*, vol. 77, no. 2, pp. 250–252, Jul. 2000.

[8] G. Koley and M. G. Spencer, “On the origin of the two-dimensional electron gas at the AlGaN/GaN heterostructure interface,” *Appl. Phys. Lett.*, vol. 86, no. 4, p. 42107, Jan. 2005.

[9] S. Inc, “ATLAS User Manual (Santa Clara, CA: Silvaco International),” 2010.

[10] W. B. Joyce and R. W. Dixon, “Analytic approximations for the Fermi energy of an ideal Fermi gas,” *Appl. Phys. Lett.*, vol. 31, no. 5, pp. 354–356, Sep. 1977.

[11] W. Shockley and W. T. Read, “Statistics of the Recombinations of Holes and Electrons,” *Phys. Rev.*, vol. 87, no. 5, pp. 835–842, Sep. 1952.

[12] R. N. Hall, “Electron-Hole Recombination in Germanium,” *Phys.*

Rev., vol. 87, no. 2, pp. 387–387, Jul. 1952.

[13] K. Xu, "Electro-Optical Modulation Processes in Si-PMOSFET LEDs Operating in the Avalanche Light Emission Mode," *IEEE Trans. Electron Devices*, vol. 61, no. 6, pp. 2085–2092, Jun. 2014.

[14] Y. Taur and T. Ning, "Fundamentals of modern VLSI devices," in *Fundamentals of modern VLSI devices*, 2nd ed., Cambridge: Cambridge University Press, 2015, pp. 11–34.

[15] Y. Nishimoto, K. Nakahara, D. Takamizu, A. Sasaki, K. Tamura, S. Akasaka, H. Yuji, T. Fujii, T. Tanabe, H. Takasu, A. Tsukazaki, A. Ohtomo, T. Onuma, S. F. Chichibu, and M. Kawasaki, "Plasma-assisted Molecular Beam Epitaxy of High Optical Quality MgZnO Films on Zn-polar ZnO Substrates," *Appl. Phys. Express*, vol. 1, no. 9, p. 91202, Aug. 2008.

[16] H. Tampo, H. Shibata, K. Maejima, T.-W. Chiu, H. Itoh, A. Yamada, K. Matsubara, P. Fons, Y. Chiba, T. Wakamatsu, Y. Takeshita, H. Kanie, and S. Niki, "Band profiles of ZnMgO/ZnO heterostructures confirmed by Kelvin probe force microscopy," *Appl. Phys. Lett.*, vol. 94, no. 24, p. 242107, Jun. 2009.

[17] C. H. Park, S. B. Zhang, and S.-H. Wei, "Origin of p -type doping difficulty in ZnO: The impurity perspective," *Phys. Rev. B*, vol. 66, no. 7, p. 73202, Aug. 2002.

[18] D. J. Leary, "Calculation of Carrier Concentration in Polycrystalline Films as a Function of Surface Acceptor State Density: Application for ZnO Gas Sensors," *J. Electrochem. Soc.*, vol. 129, no. 6, p. 1382, 1982.

[19] H. von Wenckstern, R. Pickenhain, H. Schmidt, M. Brandt, G. Biehne, M. Lorenz, M. Grundmann, and G. Brauer, "Deep acceptor states in ZnO single crystals," *Appl. Phys. Lett.*, vol. 89, no. 9, p. 92122, Aug. 2006.

[20] S. H. Park and D. Ahn, “Spontaneous and piezoelectric polarization effects in wurtzite ZnO/MgZnO quantum well lasers,” *Appl. Phys. Lett.*, vol. 87, no. 25, p. 253509, Dec. 2005.

[21] S.-T. Lien, H.-C. Li, Y.-J. Yang, C.-C. Hsu, I.-C. Cheng, and J.-Z. Chen, “Atmospheric pressure plasma jet annealed ZnO films for MgZnO/ZnO heterojunctions,” *J. Phys. D. Appl. Phys.*, vol. 46, no. 7, p. 75202, Feb. 2013.

[22] X. Bai, L. Wang, R. Zong, Y. Lv, Y. Sun, and Y. Zhu, “Performance Enhancement of ZnO Photocatalyst via Synergic Effect of Surface Oxygen Defect and Graphene Hybridization,” *Langmuir*, vol. 29, no. 9, pp. 3097–3105, Mar. 2013.

[23] E. V Lavrov, J. Weber, F. Börrnert, C. G. Van de Walle, and R. Helbig, “Hydrogen-related defects in ZnO studied by infrared absorption spectroscopy,” *Phys. Rev. B*, vol. 66, no. 16, p. 165205, Oct. 2002.

[24] J. Fallert, R. Hauschild, F. Stelzl, A. Urban, M. Wissinger, H. Zhou, C. Klingshirn, and H. Kalt, “Surface-state related luminescence in ZnO nanocrystals,” *J. Appl. Phys.*, vol. 101, no. 7, p. 73506, Apr. 2007.

[25] A. Janotti and C. G. Van de Walle, “Fundamentals of zinc oxide as a semiconductor,” *Reports Prog. Phys.*, vol. 72, no. 12, p. 126501, Dec. 2009.

[26] D. Delagebeaudeuf and N. T. Linh, “Metal-(n) AlGaAs-GaAs two-dimensional electron gas FET,” *IEEE Trans. Electron Devices*, vol. 29, no. 6, pp. 955–960, Jun. 1982.

Chapter 7

Cleanroom Metallization for Transistor Fabrication

7.1 Introduction

As discussed in the previous chapters, the formation of the two-dimensional electron gas in MgZnO/ZnO based heterostructures is achieved, and the contributing factors to the source of 2DEG electrons are also investigated. After the successful realization of 2DEG in MgZnO/ZnO based heterostructures, the fabrication of MgZnO/ZnO heterostructures based transistor is attempted in this work. There is very scanty literature available on MgZnO/ZnO heterostructure based thin film transistors [1], [2]. In this section, results of my first attempt to fabricate a transistor based on MgZnO/ZnO heterostructures is discussed. In this work, active area formation, insulation pad creation and source, drain and gate contact formation involving four photolithography steps, has been demonstrated. To attempt the device fabrication, first of all photolithography masks are fabricated for four lithography steps and then many intermediate process steps are optimized. However, the metallization process for gate contact formation have failed in our two lift-off attempts.

7.2 Photolithography

Photolithography is the process of transferring geometric shapes from a lithography mask to the surface of a substrate. In modern semiconductor manufacturing, photolithography uses optical radiation to image the mask on a silicon wafer using photoresist (PR) layers. The steps involved in the photolithographic process are wafer cleaning; moisture baking; photoresist application; soft baking; mask alignment; exposure and development; and hard-baking.

7.2.1 Wafer Cleaning, Moisture Baking, and Photoresist Application

In the first step, the wafers are chemically cleaned to remove particulate matter on the surface as well as any traces of organic, ionic, and metallic impurities. The details of the cleaning procedure are discussed in chapter 4. After cleaning, the wafers are baked at 120 °C for 45 minutes to remove traces of water. This is called moisture baking and the mentioned temperature and time of baking is used in our case. After moisture baking, the photoresist is applied to the surface of the wafer. The high-speed centrifugal whirling of wafers is the standard method for applying photoresist coatings in an integrated circuit (IC) manufacturing. This technique, known as "Spin Coating," produces a thin uniform layer of photoresist on the wafer surface. The thickness of the PR on the wafer is mainly determined by two factors, i) viscosity of the PR and ii) spinner rotational speed. In our case, the positive photoresist of 3 µm thickness is deposited using a spin coating. The recipe of spin coating to deposit 3 µm thick positive PR is 1000 rpm for 60 seconds.

7.2.2 Positive and Negative Photoresist

There are two types of photoresist: positive and negative. For positive resists, the resist is exposed with UV light wherever the underlying material is to be removed. In these resists, exposure to the UV light changes the chemical structure of the resist so that it becomes more soluble in the developer. The exposed resist is then washed away by the developer solution, leaving windows of the bare underlying material. In other words, "whatever shows, goes." The mask, therefore, contains an exact copy of the pattern which is to remain on the wafer. Negative resists behave in just the opposite manner. Exposure to the UV light causes the negative resist to become polymerized, and more difficult to dissolve. Therefore, the negative resist remains on the surface wherever it is exposed, and the developer solution removes only the unexposed portions. Masks used for negative photoresists, therefore, contain the inverse (or photographic "negative") of the pattern to be transferred.

Negative resists were popular in the early history of integrated circuit processing, but positive resist gradually became more widely used since they offer better process controllability for small geometry features. Positive resists are now the dominant type of resist used in very large scale integration (VLSI) fabrication processes.

7.2.3 Soft Baking

Soft-baking is the step during which almost all of the solvents are removed from the photoresist coating. Soft-baking plays a very critical role in photo-imaging. The photoresist coatings become photosensitive, or imageable, only after soft baking. Over soft baking will degrade the photosensitivity of resists by either reducing the developer solubility or actually destroying a portion of the sensitizer. Under soft baking will prevent light from reaching the sensitizer. Positive resists are incompletely exposed if considerable solvent remains in the coating. This under soft baked positive resist is then readily attacked by the developer in both exposed and unexposed areas, causing less etching resistance. In our case, the optimized soft baking recipe is 120 °C for 30 minutes.

7.2.4 Light Field and Dark Field Mask

There are two types of mask light field and dark field mask. In light field mask, the UV light is passing through the entire mask except for the desired image to be replicated on the wafer. Whereas in dark field mask the UV light passes only through the desired image printed on the mask and rest of the portion is opaque. The light field mask is mainly used for the island formation, and the dark field mask is mainly used for hole formation on the wafer. In our case, the mask for active area formation is a light field mask, and remaining masks are dark field masks. The masks are designed using L-Edit software and then printed on a glass plate using cobalt chrome. Fig. 7.1 shows the L-Edit image of the masks which were designed.

Fig. 7.1: The L-Edit image of the mask in which green color mask is for active area formation, the red one is for insulator pad formation, the gray one is for source and drain contact fabrication, and blue one is for gate contact fabrication.

7.2.5 Mask Alignment; Exposure and Development

One of the most important steps in the photolithography process is mask alignment. A mask or "photomask" is a square glass plate with a patterned emulsion of the metal film on one side. The mask is aligned with the wafer so that the pattern can be transferred onto the wafer surface. Each mask after the first one must be aligned with the previous pattern. Once the mask has been accurately aligned with the pattern on the wafer's surface, the photoresist is exposed through the pattern on the mask with high-intensity ultraviolet light. In our case, the optimized recipe of exposure is UV light exposed for 30 seconds.

One of the last steps in photolithography is development in which the exposed wafers are dipped in the developer solution where the unwanted PR is washed away. The optimized recipe for the developer is 25 seconds dip and hold and then 25 seconds rinse the wafers in the developer solution followed by rinsing in de-ionized (DI) water for 1 minute.

7.2.6 Hard Baking

Hard-baking is the final step in the photolithographic process. This step is necessary in order to harden the photoresist and improve adhesion of the photoresist to the wafer surface. The optimized recipe for hard-baking in our case is 120 °C for 30 minutes.

7.3 Lift-off Process

In semiconductor wafer fabrication, the term 'lift-off' refers to the process of creating patterns on the wafer surface through an additive process, as opposed to the more familiar patterning techniques that involve subtractive processes, such as etching. Lift-off is most commonly employed in patterning metal films for interconnections.

Lift-off consists of forming an inverse image of the pattern desired on the wafer using a dark field mask, which covers certain areas on the wafer and exposes the rest. After the development, the exposed area is open (hole formed). The layer to be 'patterned' is then deposited over the wafer. In the exposed areas of the wafer, the layer material gets deposited directly on the wafer substrate, while in the covered areas, the material gets deposited on top of the PR film.

After the layer material has been deposited, the wafer is immersed in acetone to dissolve the PR layer. Once the PR is dissolved, the layer material over it gets 'lifted off' (hence the term 'lift-off'), leaving behind the layer material that was deposited over the wafer substrate itself, which forms the final pattern on the wafer.

The 'lift-off' process as a patterning technique offers the following advantages: 1) composite layers consisting of several different materials may be deposited one material at a time and then 'patterned' with a single 'lift-off'; 2) residues that are difficult to remove are prevented in the absence of etching of the patterned layer; 3) sloped side walls become possible, resulting in good step coverage. On the other hand, the main disadvantage of the lift-off process is the difficulty of creating the required PR patterns for successful lift-off. Fig. 7.2 is showing the complete process flow of the lift-off process.

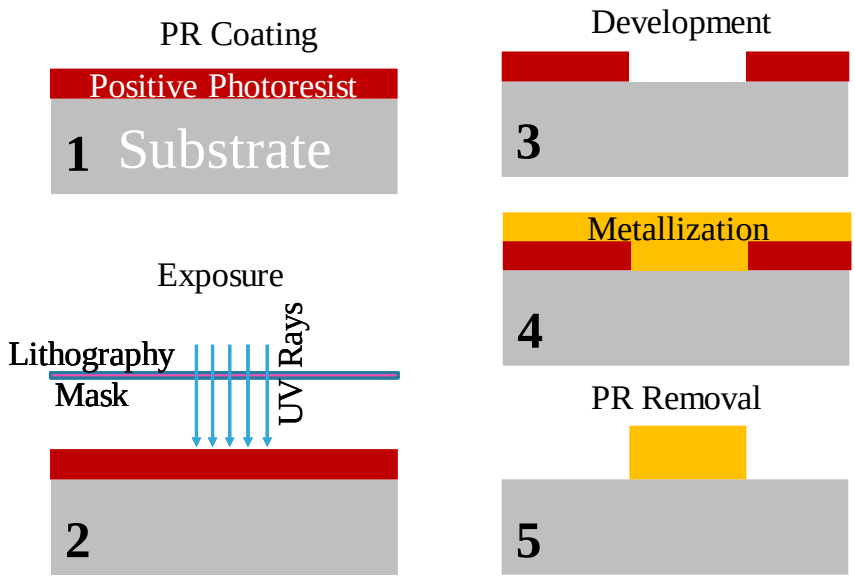

Fig. 7.2: The complete process flow of the lift-off process.

The key to successful lift-off is the ability to ensure the existence of a distinct break between the layer material deposited on top of the PR and the layer material deposited on top of the wafer substrate. Such separation allows the dissolving liquid to reach and attack the PR layer.

In our case, all the metal deposited wafers are kept in acetone for 15 hours and then agitated in ultra-sonicator for 10 min and then 2 min break. This process of agitation is repeated for 3 times.

7.4 Lithography Process for Transistor Fabrication

7.4.1 Active Area Formation

MgZnO/ZnO heterostructure grown on SiO_2 is coated with positive PR of 3 μm after wafer cleaning, moisture baking. A light field mask is used to map rectangular design of 1030 μm × 300 μm onto the heterostructure grown wafer. The wafer after UV exposure under the mask is developed in the developer and rinsed in DI water. Hereafter, the wafers are placed in an oven for hard baking of PR. The hard baked wafers are than dipped in diluted HCl for etching the unprotected heterostructure from the wafers

with an optimized time of 20 second. The etched wafers are than placed in acetone for removing the hard baked PR from the active region islands.

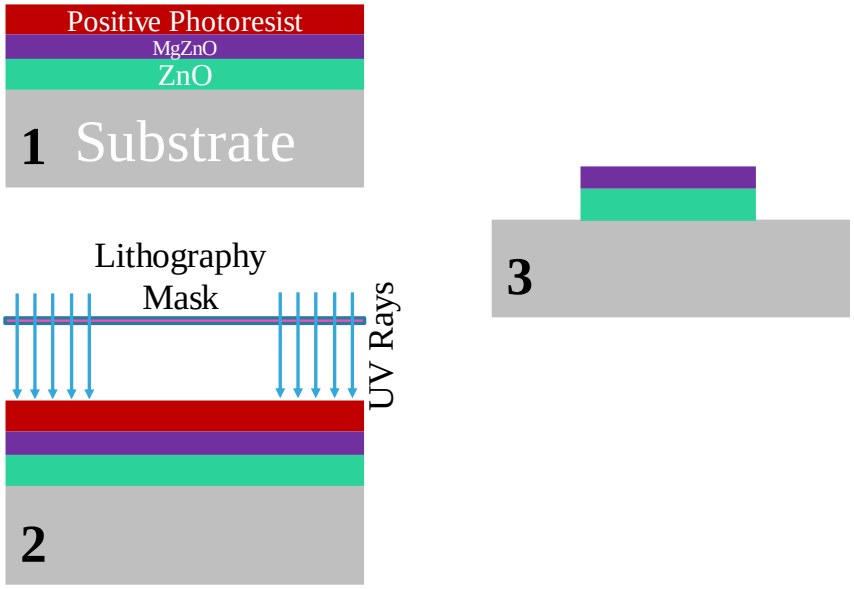

Fig. 7.3: The complete process flow of the active area formation.

7.4.2 Insulator Pad Formation

A 400 nm thick layer of SiO_2 is deposited all over the wafers with active region islands after ashing out the remnants of hard-baked PR by Asher and cleaning the wafers and moisture baking them. The SiO_2 deposited wafers are coated with 3 μm positive PR. A dark field mask is used to pattern 1020 μm × 290 μm openings in positive PR by UV exposure through the mask onto the wafers, and developing them in the developer. The developed wafers are than placed in an oven for hard baking of PR. Henceforth, the exposed SiO_2 in the hard baked wafers is etched by dry reactive ion etching (DRIE) for optimized 11 minute time, to expose the active region out of insulation pads. Hereafter, the wafers are rinsed in acetone to remove hard baked PR.

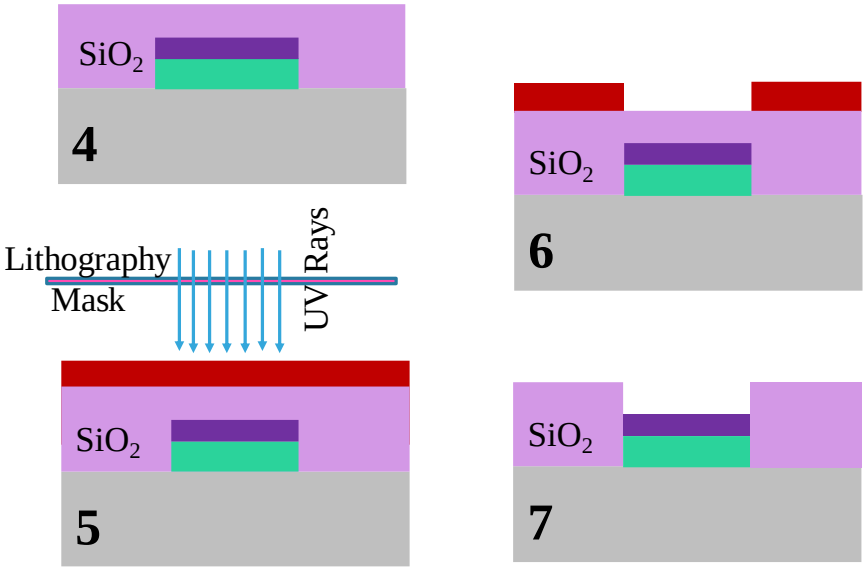

Fig. 7.4: The complete process flow of the insulation pad formation.

7.4.3 Source and Drain Formation

The wafers with the active region and insulation pad are again coated with 3 μm positive PR after cleaning and moisture baking. A dark field mask with dimension of the contact pad as 500 × 500 μm^2 and contact overlapping with active region of 500 × 200 μm^2 is used to pattern source and drain pit holes in the PR by UV exposure and development. A 10 nm Ti and 200 nm Au is deposited over the developed wafers after hard baking. These wafers are than placed in Acetone for 15 hour period before agitating them in ultra-sonicator to shed the metal deposited over PR to obtain the patterned metal shape.

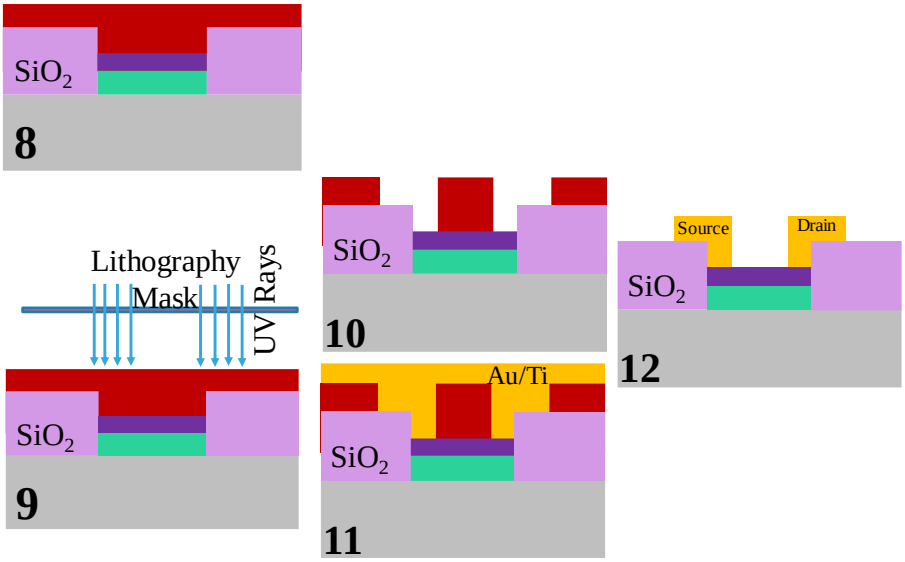

Fig. 7.5: The complete process flow of source and drain contact formation.

7.4.4 Gate Formation

The wafers with the source and drain contacts were further coated with 3 μm positive PR after cleaning and moisture baking. A dark field mask with varying dimensions of gate width ranging from 3 μm to 10 μm with 500 × 500 μm^2 contact pad is used to pattern gate region in the PR by UV exposure and development. A 10 nm Ti and 200 nm Pt is deposited over the developed wafers after hard baking. These wafers were then placed in Acetone for lift-off by agitating them in ultra-sonicator to shed the metal deposited over PR to obtain the patterned contact shape.

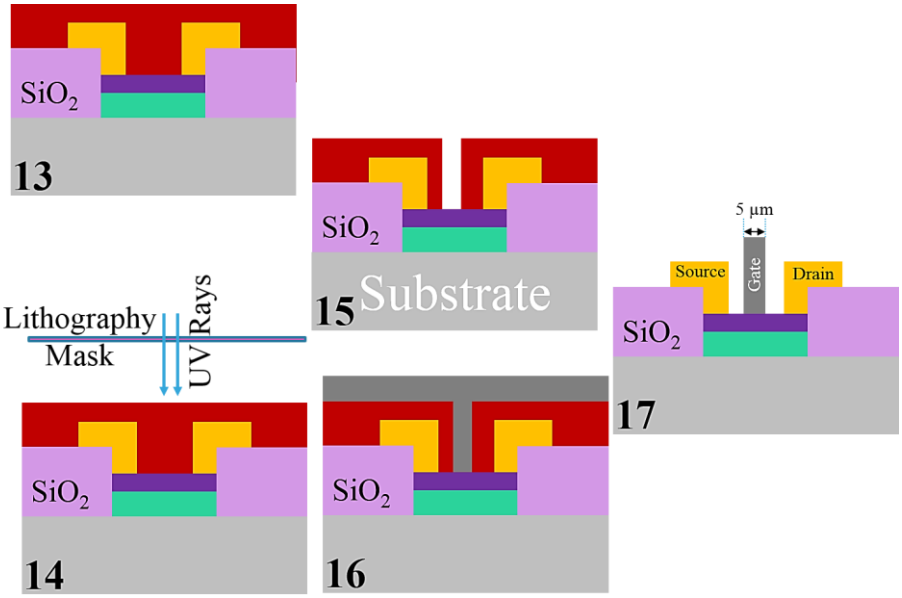

Fig. 7.6: The complete process flow of Gate contact formation.

7.4.5 Characterization of Source and Drain

The developed source-drain contacts of Au/Ti are than characterized by optical profilometer for ensuring the pattern replication from mask and continuity of the contacts. Fig. 7.6 (a) shows the zeta image of the fabricated source and drain contacts. Hereafter, electrical characterization of *I-V* is performed to ensure the ohmic nature of the contacts. The Fig. 7.6 (b) shows the linear behavior of the current with increasing voltage observed in the as-developed source-drain contacts proving them to be perfectly ohmic.

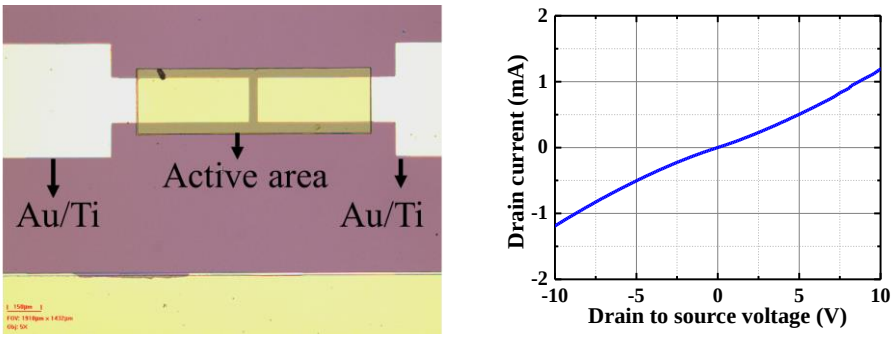

(a) **(b)**

Fig. 7.7: (a) Zeta image of the fabricated device. (b) Drain current vs. drain to source voltage curve.

7.5 Conclusion

First attempt to fabricate complete transistor on DIBS grown MgZnO/ZnO heterostructure is demonstrated. The complete cleanroom process flow for device fabrication is discussed. The source and drain contacts of Au/Ti are fabricated successfully on top of MgZnO/ZnO heterostructures. The ohmic nature of these contacts are also tested using *I-V* measurements and found almost linear. The intermediate process steps used are also optimized, and the mask for the photolithography is also fabricated. The two lift-off attempts of gate metallization failed and hence remains as future course of action to realize reliable gate.

7.6 References

[1] I.-C. Cheng, B.-S. Wang, H.-H. Hou, and J.-Z. Chen, "MgZnO/ZnO Heterostructure Field-Effect Transistors Fabricated by RF-Sputtering," *ECS Trans.*, vol. 50, no. 8, pp. 83–93, Mar. 2013.

[2] B.-S. Wang, Y.-S. Li, and I.-C. Cheng, "Mobility Enhancement in RF-Sputtered MgZnO/ZnO Heterostructure Thin-Film Transistors," *IEEE Trans. Electron Devices*, vol. 63, no. 4, pp. 1545–1549, Apr. 2016.

Chapter 8

Conclusion and Future Scope

With better electronic and elastic properties, MgZnO/ZnO material system is useful for high frequency and high power applications. Due to large spontaneous and piezoelectric polarization and high conduction band offset, a higher 2DEG density is achieved in this material system. Recent research has shown that ZnO has the capability to meet the increasing demands for higher operating frequencies and power. But due to the technological challenges faced by researchers currently, innovative solutions, both in design and material configurations are required to make it possible. It has been observed that changing the thickness of barrier layer (MgZnO), has significant impact on 2DEG density when other parameters are kept constant. In MgZnO/ZnO material system, the 2DEG is observed mainly by single crystalline deposition techniques, which are, however, not suitable for low cost and large area fabrication. Very few reports are available in literature in which 2DEG is observed by sputtering, but detailed study on sputter deposited 2DEG is still lacking in the literature. Thus, in order to improve the 2DEG density in sputter deposited MgZnO/ZnO heterostructures and improving the understanding of the effects of variation of different parameters like barrier layer thickness, cap layer thickness and Mg molar composition in barrier layer were studied here.

In this research work, the optimization of fabrication of ZnO and MgZnO thin films was performed using the state of art DIBS system. After the growth, the thin films were characterized for structural, electrical, morphological and elemental properties. The optimization of growth parameters included a variation of deposition temperature and gaseous ambient in the DIBS system. Efforts were put to establish the correlations among different properties by employing XRD, Hall, and HRTEM measurements techniques. It was observed that the thin films' properties

were highly dependent on the growth parameters and the high-quality films could be successfully obtained at even low temperature by DIBS system. Further, after investigating the material properties, the properties of MgZnO/ZnO heterostructures were analyzed with the objective to achieve large 2DEG density and the applicability of the MgZnO/ZnO heterostructure for HFETs. For the development of MgZnO/ZnO heterostructures based HFETs the source and drain contacts of Au/Ti are fabricated on top of MgZnO/ZnO using lift-off process. The gate contact of Pt/Ti is also attempted using lift-off process but the lift-off was failed two times. This is the first attempt made on DIBS grown MgZnO/ZnO heterostructures.

8.1 Conclusions

The main outcomes of this thesis are summarized as follows:

(i) The $Mg_{0.05}Zn_{0.95}O$ film (MZO) was fabricated by the DIBS system on *p*-Si (111) substrate at 80 % oxygen partial pressure and 300 °C growth temperature. On the fabricated film, for Schottky contact (SC) formation, a 100 nm thick and 12.3816 μm^2 area Au was deposited by DIBS at room temperature. The electrical, structural, and elemental properties of the films were investigated. The temperature dependent *I-V* and *C-V* measurement were done for the SC. XRD measurement demonstrated that the MZO film was polycrystalline in nature with preferred crystal orientation in (002) plane at 2θ = ~34.4°. The resistivity, carrier concentration, and mobility of the MZO film were evaluated to be 0.12 Ω-cm, 6.05×10^{17} cm^{-3}, 85.12 $cm^2V^{-1}s^{-1}$, respectively at room temperature from Hall measurement.

The temperature dependent *I-V* measurement of the SC reveal that with increasing measurement temperature, the barrier height increases and the ideality factor decreases. This

anomalous temperature dependence of the barrier height and ideality factor could be associated with the nature of inhomogeneous Schottky barrier consisting of a combination of low and high barrier patches. Temperature-dependent SBH describes a DGD with mean apparent barrier heights of 0.95 and 0.54 eV and standard deviations of 0.131 and 0.074 eV in the temperature range of 160–300 K and 80–160 K, respectively. The larger value of SBH inhomogeneity is attributed to interface states at the MS junction. The interface state density at 300 K varied from 6.46×10^{14} $eV^{-1}cm^{-2}$ at E_C-0.27 eV to 1.58×10^{14} $eV^{-1}cm^{-2}$ at E_C-0.74 eV. Thus, it is concluded that the presence of barrier inhomogeneity and interface state density are the main reason for deviation of Schottky junction characteristics from its ideal behavior.

(ii) A physics-based generic analytical model for the graded and fully strained MgZnO/ZnO heterostructure with cap layer was developed for the calculation of 2DEG density and V_{OFF}. The generic model can be easily reduced for relatively simpler structures. Calculated n_s values suggested that the use of graded MgZnO layer significantly increases (2.3 times higher) the 2DEG density in MgZnO/ZnO heterostructure but at the expense of an increased threshold voltage. A graded structure with low thickness of layers was proposed, to achieve a compromise between high 2DEG density and V_{OFF}, based on the developed model. An alternate expression for the net polarization sheet charge density difference at barrier-buffer interface to overcome the existing discrepancy with an experimental data has also been suggested. The proposed model will be a useful tool for the design and optimization of 2DEG and V_{OFF} in ZnO-based heterostructures.

(iii) ZnO-based 2DEG yielding heterostructures, with MgZnO as the barrier layer, were fabricated by DIBS system and probed for variations of n_s and mobility as a function of the Mg composition in the barrier layer, barrier layer thickness and cap

layer thickness. XRD and HRTEM results showed the high crystallinity of the buffer ZnO as well as a flat and uniform heterointerface, which are essential for the formation of 2DEG. The values of n_s were observed to increase with the corresponding rise in Mg composition for both the bilayer (MgZnO/ZnO heterostructures) and capped (ZnO/MgZnO/ZnO heterostructures) structures. At $x = 0.3$, for the bilayer structure, the values of n_s and mobility were 1.11×10^{14} cm^{-2} and 28.13 $cm^2V^{-1}s^{-1}$, respectively at RT. The observed n_s saturated at a higher barrier layer thickness for the bilayer heterostructure. The effect of variation in the cap layer thickness suggested an enhanced n_s for a thinner cap layer thickness (1.65×10^{14} cm^{-2}), which decreased and saturated at a higher cap layer thickness. The carrier profiling done by *C-V* measurement indicated a high carrier concentration (~10^{20} cm^{-3}) at 30 nm from the top surface of the bilayer heterostructure, which is the barrier/buffer interface, indicating the confinement of charge carriers. The temperature dependent Hall measurement indicated almost a constant sheet carrier concentration in temperature range of 5 K to 300 K. The observation of *C-V* measurements and the temperature dependent Hall measurement confirmed the formation of 2DEG in the heterostructures.

(iv) The source of electrons in 2DEG in MgZnO/ZnO heterostructures grown by different deposition techniques were investigated using an insightful analysis based on electrostatic neutrality across barrier and buffer layer. The proposed theory was compared with ATLAS simulations to account for different contributing factors and the effect of each such factor on 2DEG density. The analysis was further verified by comparing the results with published experimental data for epitaxial and sputtering growth mechanisms. The epitaxially grown MgZnO/ZnO heterostructures showed a non-negligible role of acceptor states towards the formation of 2DEG density. The surface donor density showed a causal-effect relationship in

presence of acceptor states. In contrast, the 2DEG density in sputtered MgZnO/ZnO samples was an order high, and exceeded the barrier-buffer polarization difference limit. This was due to the interface states present at the MgZnO/ZnO interface due to sputtering growth technique and lead to formation of interface trap charges which contribute towards enhancement of 2DEG density.

(v) The source and drain contacts of Au/Ti were fabricated on top of MgZnO/ZnO heterostructures using lift-off process for the development of HEMT using this heterostructure. The fabricated source and drain contacts were characterized using *I-V* measurement and the result of *I-V* measurement was found to be linear indicating the ohmic nature of the fabricated contacts. The fabrication of gate contact of Pt/Ti was failed two times using lift-off process. So fabrication of reliable gate contact using lift-off process is future work.

8.2 Future Scope

Although, the physics based analytical model for the estimation of 2DEG density in MgZnO/ZnO heterostructures was developed and 2DEG was realized by fabricating the MgZnO/ZnO heterostructures using DIBS. The source and drain contacts were also fabricated on top of MgZnO/ZnO heterostructures using lift-off process. The following future works can be focused

(i) Optimization of source and drain contacts in terms of contact resistance.

(ii) Formation of reliable gate contact on MgZnO/ZnO heterostructures by lift-off process and characterization of HEMT.

(iii) Optimization of gate geometry of fabricated transistor to study its effect on gain and trans-conductance.